The Dissertation Committee for Ryan Joseph Nagao Certifies that this is the approved version of the following dissertation:

CREATION OF AN OPTIMIZED ACELLULAR SCAFFOLD FOR IMPROVED VASCULAR ENGINEERING

Committee:

Laura J. Suggs, Supervisor

Christine E. Schmidt, Co-Supervisor

Roger P. Farrar

Andrew K. Dunn

Aaron B. Baker

CREATION OF AN OPTIMIZED ACELLULAR SCAFFOLD FOR IMPROVED VASCULAR ENGINEERING

by

Ryan Joseph Nagao, B.S.

Dissertation

Presented to the Faculty of the Graduate School of
The University of Texas at Austin
in Partial Fulfillment
of the Requirements
for the Degree of

Doctor of Philosophy

The University of Texas at Austin
May, 2013

Acknowledgements

I would like to thank the hard work my undergrad students Ross Malik, Yafei Ouyang, Renee Keller, and Curtis Lee and Remeditex employee Diana Gutierrez put in over the course of this project. Without their help, I undoubtedly would not have been able to successfully complete my experiments in a timely fashion, and likely have gone insane.

Thank you to the various mentors I have been lucky enough to learn from: Jon Nickels, Jae Lee, and Leo Forciniti all imparted me with guidance on how to approach science.

Thank you to the National Institute of Health, the Gillson-Longenbaugh Foundation, and the venture capital group Remeditex for believing in my research goals and competence. Special thanks to Claire Aldridge of Remeditex for prioritizing the completion of my graduate project.

CREATION OF AN OPTIMIZED ACELLULAR SCAFFOLD FOR IMPROVED VASCULAR ENGINEERING

Ryan Joseph Nagao, Ph.D.
The University of Texas at Austin, 2013

Supervisor: Laura J. Suggs, Christine E. Schmidt

Engineering a complex tissue that exceeds 100-200 μm requires a vascular connection. Methods to enhance vascularization include the delivery of angiogenic factors, and the use of scaffolds that encourage vascular ingrowth. However, these techniques rely on the host to vascularize the construct upon implantation, which is often too slow to provide nutrients to the entire construct. Hence, recent research has focused on creating *de novo* vascular networks prior to implantation. Such technologies would enable faster anastomosis with the host vascular system, as well as fully perfused constructs that can increase cell viability. Many techniques have been investigated to create *de novo* vascular networks with varying levels of success. Our approach was to utilize native vascular extracellular matrix (ECM) obtained from decellularizing highly vascularized tissue as a substrate for re-endothelialization and thus to create a three-dimensional vascular bed for ultimate use with various implant and tissue engineering applications. We have demonstrated a method of chemical decellularization that effectively removes cellular material while leaving behind an organized patent vascular network down to the capillary scale. Standard histological methods, DNA quantification, as well as vascular corrosion casting demonstrated this efficacy. Subsequent subcutaneous implantation then explantation of the scaffold at 7 and 28 days was used to assess the immunogenicity of the graft by analyzing the presence of immune cells. This scaffold was then re-endothelialized with human dermal microvascular endothelial cells (HDMECs) and conditioned with peristaltic flow for 60 hours to help improve vascular patency. Cellular distribution was determined qualitatively by first incubating the HDMECs with gold nanotracers, then imaging their presence upon implantation through ultrasound-guided photoacoustic (US/PA) imaging. Following the culture process, the scaffolds were analyzed for vascular patency through vascular corrosion casting, and cellular phenotype through histological methods—demonstrating a decrease in vascular damage. The re-endothelialized scaffolds were then assessed for functional vascular performance by perfusing whole blood through them. Results demonstrated better blood clearance in re-endothelialized scaffolds compared to scaffolds without cells. These results point to the ability of the optimized acellular (OA) scaffold to be used in future experiments focused on vascular and tissue engineering.

Table of Contents

List of Tables

List of Figures

Chapter 1: Introduction

Tissue engineering techniques are attempting to alleviate problems experienced because of the shortage of organ donors, by creating functional alternatives for those in need. To date, successful tissue engineered products have been limited in part because of poor nutrient delivery to cells within constructs that are more than several hundreds of microns thick—this is in part because they lack a vascular network. Thus, improving the capabilities to achieve vascularization of tissue constructs has become one of the paramount topics in biomedical engineering.

Current strategies to improve the vascularization of tissue constructs encompass the traditional tissue engineering focuses: scaffolds, growth factors, and cells, in innumerous combinations. Angiogenic factors have increased vascular growth into constructs—which have in turn been investigated to determine ideal properties for vascular ingrowth. Countless cell lineages have also been evaluated for their efficacy as well. As the field of vascular engineering has become more mature, research has begun to focus on ways to create working vascular networks in scaffolds *in vitro*, prior to their implantation *in vivo*. This strategy aims to create networks that only require vascular ingrowth into the extremity of the scaffold in order to anastomose into the network and subsequently provide rapid nutrient delivery.

We have created a thick tissue engineering scaffold that maintains the native architecture of a highly vascularized tissue down to the capillary scale. This construct can be perfused with cells to ensure their even distribution throughout its entirety; it can be connected to peristaltic flow to condition cells within the vascular network; it also has the potential to be anastomosed into a vascular axis in the body, enabling rapid perfusion.

Such a construct could support cellular viability throughout its entirety, and become a potential candidate for organ replacement in future studies.

This dissertation is divided into six chapters. Chapter 2 provides background information regarding past research and successes in tissue engineering scaffolds, centered on improving vascularization of scaffolds. A description of the potential benefits of tissue engineering scaffolds, scalability issues, and current solutions to scalability problems is first presented. Next, an overview of decellularization techniques, and possible advantages over synthetic scaffolds are discussed, followed by a discussion of the important components of the extracellular matrix to vascular engineering. Finally, an in depth look at cells used in vascular engineering is presented.

Chapter 3 describes the development and characterization of an optimized decellularization method compared to other decellularization methods. The experimental design and methods used throughout the creation and evaluation of the vascular optimized acellular (OA) scaffold, methods for characterizing tissue following decellularization, and implantation into animals for immunogenicity testing will be described. The OA scaffold provided better preservation of vascular patency following decellularization compared to other decell methods, while still removing cellular and immunogenic material. Differences between decell methods were not seen through normal histological methods, but were only visualized during VCC—supported through histological, vascular casting, and *in vitro* analyses.

Chapter 4 presents the work necessary to re-endothelialize the vascular OA scaffold. Different endothelial cell lineages were injected into the vascular axis of the vascular OA scaffold and assessed for initial distribution, retention following perfusion culture, and the subsequent vascular performance of the tissue—indicated with vascular corrosion casts, and propensity to hemorrhage following the injection of whole blood.

Optimizing the re-endothelialization enabled even distribution of cells as seen through US/PA imaging. Subsequent VCC analysis demonstrated a recovery of vascular patency due to re-endothelialization. The re-endothelialized OA scaffold also allowed for better clearing of whole-blood compared to barren scaffolds.

Chapter 5 entertains a discussion of the results in Chapter 4. The reasoning behind the selection of the decellularization protocol, as well as control groups is highlighted. Animal selection and source material selection was also explained, both for the organ harvest, as well as the immunogenicity study. A discussion of the components removed and preserved following the decellularization process is presented regarding their importance in vascular engineering. The interpretation of vascular casts is also discussed, highlighting the importance of testing for functionality when performing decellularization. Interpretation of US/PA imaging as a tool for tracking cellular distribution is also discussed. Finally, the function recovery regarding vascular patency following re-endothelialization, and its importance in subsequent tissue engineering ventures is discussed.

Chapter 6 is a summary of the work performed to complete this dissertation, as well as the future directions for this project—both as a substrate for tissue regeneration, as well as for use as a substrate to obtain a better understanding of biological phenomenon in a complex environment.

Chapter 2: Background Information on Tissue Engineering Thick Constructs—the Importance of a Working Vasculature

As the organ wait list continues to exceed the number of donors each year (over 100,000 in need, under 15,000 donors) [1], the need for alternative therapies to transplantation, such as tissue engineered constructs, is becoming increasingly important. Yet, the most successful tissue engineered products have been either avascular structures (cartilage) or thin membranes (skin and bladder) (**Figures 1, 2**) [2-4]. Engineering more complex tissues, such as myocardium, bone, or skeletal muscle, requires a nutrient delivery system that matches the metabolic needs of the tissue [5]. Researchers have demonstrated that a vascular connection is necessary to maintain viability in tissues beyond 100-200 μm thick [6]. One of the limiting factors in creating a complex tissue construct is the rate of vascular ingrowth upon implantation. The spontaneous vascular growth in the human body is only several tenths of microns per day [7], far too slow to traverse constructs ranging in the hundreds of microns in a biologically-relevant time scale. This limited vascular ingrowth results in poor nutrient and oxygen delivery to the cells comprising the construct. Nutrient delivery is a critical component for any type of organ transplantation [8], and the failure to address the metabolic needs of cells often leads to the formation of necrotic cores in engineered substitutes [9-13]. A hindered oxygen supply is not only responsible for cell death and the failure of most grafts [14], but can also increase vascular endothelial growth factor (VEGF) and mRNA transcription, which can have detrimental effects on tissues by producing leaky, abnormal vascular structures [15, 16]. To overcome these potential problems, researchers have attempted to create *de novo* vascular constructs prior to implantation. However, many of these techniques fail to create mature, three-dimensional networks. Another concern with current strategies has been keeping cells viable in the construct as the vascular network is

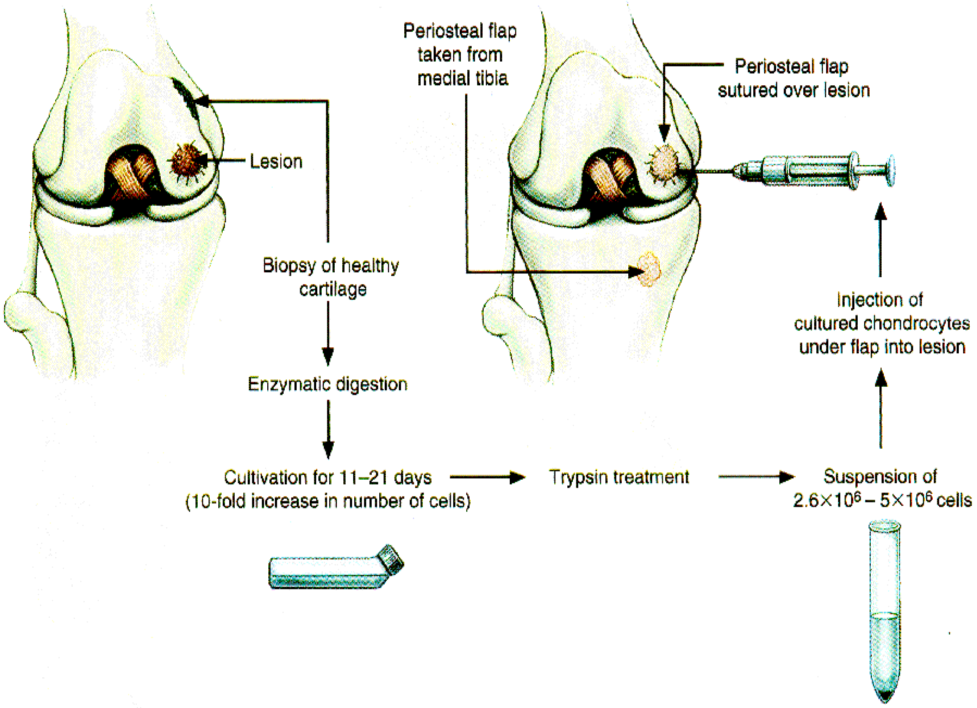

Figure 1. Diagram of chondrocyte transplantation in the right femoral condyle. (Brittberg, M., *et al.* New England Journal of Medicine, 1994).

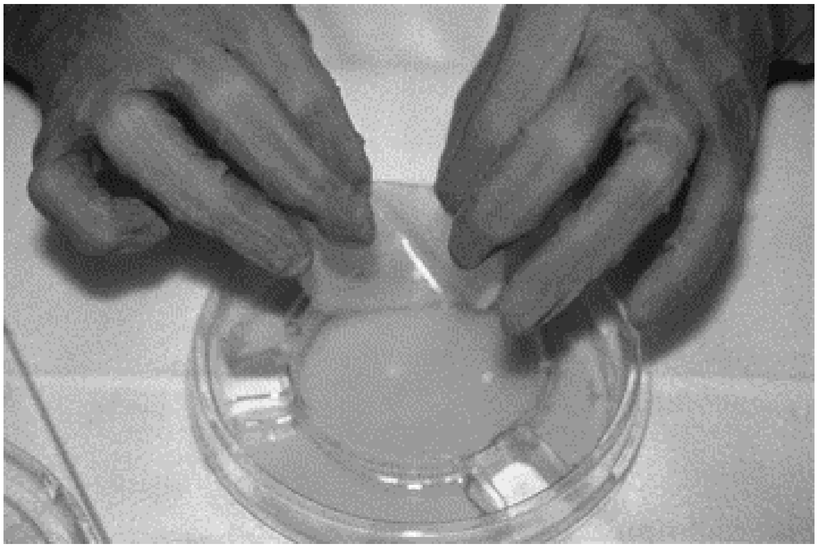

Figure 2. Apligraft prior to clinical use. Apligraft is a bilayered skin simulant constructed of type-I bovine collagen (extracted from bovine tendons and subsequently purified) and live allogeneic human fibroblasts and keratinocytes (isolated from human foreskin). Apligraft is packaged in a clear plastic carrier tray assembly consisting of four pieces—the tray, a tray insert with porous membrane, a gel tissue-support medium and the tray lid. (Kirsner, R.S., *et al.* Trends in Biotechnology, 1998).

being synthesized [17]. We aim to create a construct with a functional vascular network that can be microsurgically connected to the host vasculature, which will ensure rapid anastomosis and the likely survival of cells within the construct.

Many clinically available tissue constructs and tissue engineered products are derived from natural tissues, including the porcine small intestinal submucosal (SIS)-based acellular products from Cook Biotech, AlloDerm decellularized human dermis from LifeCell, and AxoGen's Avance decellularized human nerve graft. These are examples of intact tissues that have been decellularized and used clinically as growth-promoting scaffolds. In addition, other products are derived from natural tissue components, rather than intact tissues, including the Apligraft skin substitute from Organogenesis, Inc., which consists of natural collagen combined with neonatal human cells (**Figure 2**), and Ace Surgical Supply, Inc.'s Osteocel allograft "powdered" bone matrix, which retains native immune-privileged mesenchymal stem cells (MSCs). Despite these exciting clinical advances, less academic research is being devoted to investigate either how to modify natural materials to make them more effective, or to pursue new avenues in which these materials can be used. Instead, most academic research is focused on complex synthetic materials and nanocomposites, although the clinical viability of these approaches may be farther from realization. We use decellularized ECM as a construct upon which endothelial cell lineages will expand and form a biologically relevant vascular network. A few other researchers have investigated the ability to re-endothelialize an acellular vascular scaffold [18-20]; however, these researchers used a tissue source that was only 200 μm thick. Furthermore, the construct formed was not evaluated for immunogenicity or long-term thrombogenicity. By using a decellularized 3D native vascular scaffold as a framework for endothelial expansion, we combat the issues that have plagued the success of tissue constructs. Furthermore, using acellular scaffolds provides a potentially unlimited source of starting material from cadavers or xenogeneic sources.

In addition to natural acellular tissues, which will facilitate future translation, we also propose to use HDMECs to re-endothelialize the remaining vascular ECM network. The controlled injection into only the vascular space enabled the patency of the vascular network to improve versus scaffolds without cells. This system has the potential for use as an *ex vivo* culture system to test more clinically relevant cell models in subsequent studies.

2.1 ANGIOGENIC FACTORS AND PERMISSIVE SCAFFOLDS FOR VASCULARIZATION

The use of growth factors is one area of research that has attempted to promote vascularization. The most well-known angiogenic growth factor is vascular endothelial growth factor (VEGF). In addition to VEGF, other growth factors which promote new vessel formation include placental growth factor (PIGF), and basic fibroblast growth factor (bFGF) [21]. However, use of these growth factors creates vessels which are erratic, hemorrhagic, and leaky [16, 22]. To correct these drawbacks, researchers have investigated ways to promote vessel stability. Most attempts involve the use of growth factors that recruit pericytes or smooth muscle cells. For example, transforming growth factor beta (TGF-β) forms ECM that causes interactions with endothelial cells (ECs) and mural cells and more stable vessels [21, 23]. Platelet derived growth factor (PDGF) and angiopoietins (Ang1/2) have also been used to stabilize vessels [24-26]. In addition to growth factors that directly influence vessel stabilization, indirect therapies, such as sonic hedgehog (SHH), can lead to VEGF and Ang1/2 expression and the formation of stable vessels. Although these methods can increase vascularization and the rate of vascular ingrowth when combined with a tissue construct, they still require the host vascular system to initiate vascularization on the exterior of the tissue construct, leading to nutrient deficiency and hypoxia in the center of the construct [17].

Closely coupled to the use of angiogenic factors are scaffolds designed to permit vascular ingrowth and physical support. Tissue engineered scaffolds must be designed to provide cells with a substrate on which they can proliferate and differentiate. In addition to supporting the tissue-specific cells that the construct has been seeded with, the scaffold must allow for incorporation into the site that it is implanted. Angiogenic factors are capable of providing cues that promote increased levels of angiogenesis and are often coupled to scaffolds as a therapeutic combination [27]; however, scaffolds need to be optimized to allow for easy vascular ingrowth. Researchers have demonstrated that pores that are greater than 250 µm allow for faster ingrowth (**Figure 3**) [28]. Additionally, pore connectivity has been shown to be an important factor in facilitating vascular ingrowth [29, 30]. Although scaffolds help direct vascularization of a tissue construct, this organization is still erratic and too slow to prevent central necrosis. Bioreactors that help perfuse constructs with cells have been used to prevent necrosis in the middle of the construct [31]. However, bioreactor use still does not address concerns regarding forming a functional vasculature that can be anastomosed upon implantation [32]. As such, research has been dedicated to creating systems that give rise to a functional and well defined vascular architecture.

2.2 ENGINEERING A VASCULAR ARCHITECTURE

With the shortcomings relying on the host to vascularize a tissue engineered construct, research has focused on creating *de novo* vascular networks prior to implantation. Such technologies would enable faster anastomosis with the host vascular system, as well as fully perfused constructs that can increase cell viability. Additionally,

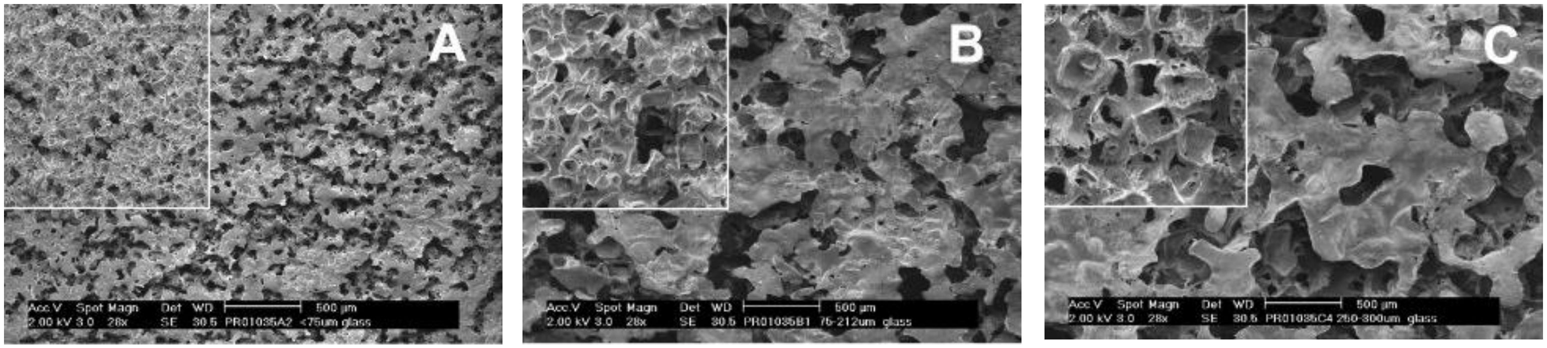

Figure 3. The structure of the porous poly(ether ester) block–copolymer scaffolds as imaged by electron microscopy. Three different types of scaffolds (A: 20–75 µm; B: 75–212 µm, C: 250–300 µm) were implanted into the chamber to measure neovascularization. (Druecke, D., *et al.* Journal of Biomedical Materials Research Part A, 2004).

tissue engineered constructs must mimic the shape of a vascularized network down to capillary meshes and support fluid flow. Ott *et al*. have demonstrated that ECs cultured in the presence of fluid shear stress have better retention in vascular constructs once implanted into patients [33]. When subjected to fluid shear stress ECs change morphology and align their actin filaments in the direction of the applied stress [34, 35]. Shear stress not only directs morphological change but also affects gene expression in ECs, upregulating prostacyclin secretion [36]. Technologies that attempt to recreate biologically relevant geometries, as well as functional vessels can be divided into microfabricated and prevascularized techniques.

2.2.1 Microfabrication

Microfabrication has been used in a number of biological applications to obtain well defined architectures that suit their function. Soft lithography can be used to create microfluidic devices that have since been applied to biological systems [37, 38]. Endothelial cells have been successfully added to the surface of microchannels in vascularization engineering applications [39, 40]. Such devices are ideal for vascular engineering as they can achieve capillary dimensions and can sustain fluid flow. However, these early attempts at a vascular tissue engineered construct suffered from problems regarding the substrate used, and the channel geometry created. Most systems relied on poly(dimethylsiloxane) PDMS substrates, a polymer that yields unpredictable interactions with biological components [41]. Since then, alternative biodegradable substrates including poly(lactic co-glycolic acid) (PLGA) [42] and poly(glycerol sebacate) (PGS) [43] have been implemented in soft lithographical systems. However, although these polymers have better known cellular interactions, their mechanical properties and degradation profiles are not well understood in microfluidic systems [44].

Another issue with early microfluidic systems was the rigid geometry of the channels produced [41]. PDMS microchannels typically have rectangular cross-sections and sharp furcations which lead to problems in cell seeding [45], and shear dynamics [46]. Recently, Borenstein et al. attempted to address these geometrical considerations by constructing a microfluidic system that has rounded cross-sections and smooth furcation transitions (**Figure 4**) [41]. Although this system has ideal geometries for vascular reconstruction, the PDMS substrate used still inhibits the practicality of this method. Another problem with the methods discussed so far is their inability to be translated into three-dimensional (3D) constructs. Most systems are simply thin films that contain microchannels. To achieve 3D constructs, researchers have resorted to stacking thin films together or rolling them into 3D tubes [40]. Other methods like 3D printing have been utilized successfully in tissue engineering to create 3D constructs [47, 48]; however, issues regarding the pore size and mechanical properties of the substrates used in this method detract from the efficacy of this technology [49].

2.2.2 Prevascularized Techniques

Alternative methods to create a fully perfused construct that can be rapidly anastomosed have involved prevascularization. Although this technique does not offer the precision of microfabricated techniques, by allowing natural vessel formation to occur prior to implantation, a functional vasculature can be created in comparatively thick constructs. In general, prevascularized techniques rely on *de novo* vascularization prior to implantation into the region of interest. The two main methods have been implemented to achieve this are divided into *in vivo* and *in vitro* techniques.

Prevascularization *in vivo* utilizes the host vascular system to perfuse constructs in an inert region prior to transplantation to the region of interest. This technique is a

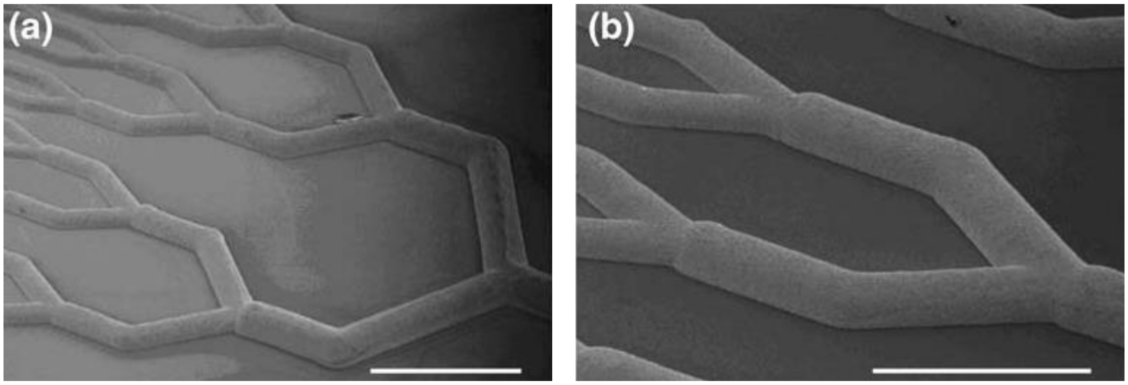

Figure 4. Microfabricated vascular structures. (a) SEM image of a Cu electroplated mold on silicon wafer showing four levels of smooth vessel bifurcations. (b) Higher magnification SEM image showing inverse half cylindrical geometry of the electroplated mold to be used to emboss half-cylindrical channels in polystyrene. Scale bars are 1 mm (a) and 500 microns (b) (Borenstein *et al.*, 2010).

modification of a surgical procedure developed in the 1960s by Buncke and McLean [14]. These researchers wrapped a vascular transplant around a tissue implant to accelerate anastomosis. Since that time, the use of an arteriovenous (AV) loop to perfuse tissue implants *in vivo* has been successfully demonstrated [50]. This technique has subsequently been implemented with a variety of constructs to promote vascularization and regeneration of various tissues [51-54] (**Figures 5, 6**) and large animal models [55]. In this method, the AV loop is either wrapped around the tissue construct, or implanted directly into the graft. This allows the host vascular system to vascularize the construct for several weeks. After this vascularization period, the construct is harvested along with the vascular axis (the major artery and vein vascularizing the tissue) and microsurgically connected to the host vascular system in the defect site. This method allows for rapid anastomosis to occur throughout the construct in a fully functional system. Despite these benefits, the necessity for multiple surgeries and the loss of a functional vascular axis are significant drawbacks. Additionally, some cell death, and unwanted tissue formation in the graft during the vascularization period *in vivo* is likely to occur.

In contrast, *in vitro* prevascularization is a co-culture method used to develop lumen in tissue constructs prior to implantation. Endothelial cells are co-cultured with mural cells and tissue-specific cell lineages to achieve an implantable construct. Once implanted, these constructs can anastomose with the host after only four days [56]. Skin [57], muscle [58], cardiac muscle [59], and bone [60] have all been therapeutically tested using this method with differing levels of success (**Figure 7**). One reason for the dissonance of results, even in the same tissue type is the variability of the culture process [17]. The nature of co-culturing cells makes optimization for each cell line used nearly impossible. Each time a new cell line is used, the process needs to be modified to ensure

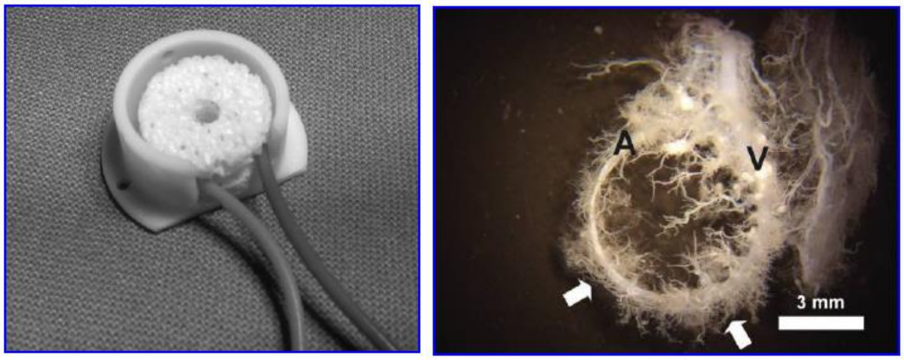

Figure 5. Photograph of a matrix encased in the isolation chamber before implantation. The arteriovenous loop is simulated using plastic tubing (Left). Vascular corrosion cast of a construct from group A (8 weeks after implantation). Blood vessels of different sizes originate from the circular arteriovenous loop. A higher vascular density is observed in the venous region of the loop than in the vein graft or the arterial region. Arrows indicate the site of the anastomosis between the vein graft and the vascular pedicle. A¼ artery, V¼vein. (Kneser, *et al.* Tissue Eng, 2006).

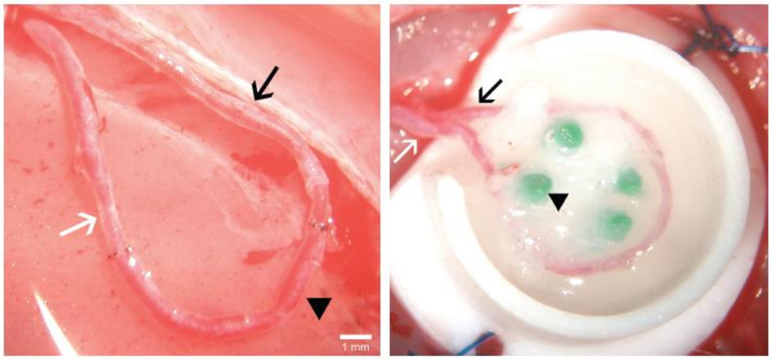

Figure 6. Microsurgically created AV loop in the groin of the rat, consisting of femoral artery (Left) (black arrow), interpositional vein graft (arrow head) and femoral vein (white arrow). (Right) Teflon chamber (inner diameter 10 mm, height 6 mm) filled with fibrin, containing the AV loop femoral artery = black arrow, interpositional vein graft = arrow head and femoral vein = white arrow) wrapped around the fixing stacks (arrow head). (Bach, *et al.* J Cell Mol Med, 2006).

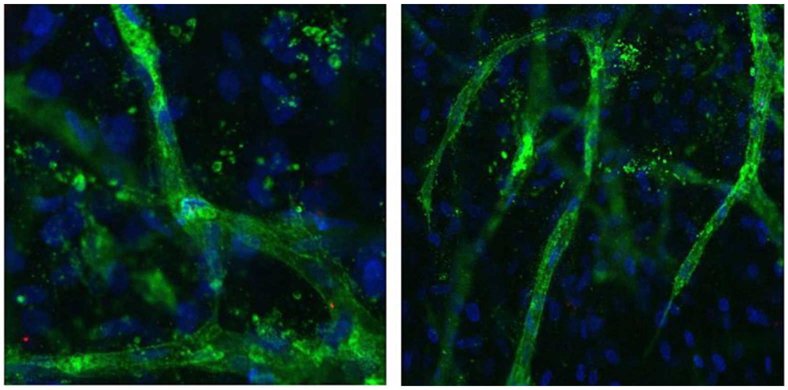

Figure 7. Prevascularization in vitro. Images of Calcein-AM-stained HDMEC under angiogenic-stimulating of HDMEC and HDMEC in coculture with primary human osteoblasts on porous hydroxyapatite (left), porous calcium phosphate (right). Confocal images of qdot-labeled HDMEC in coculture with HOS stained with endothelial cell-specific PECAM-1 (green) and nuclei stained with DAPI (blue) 42 days after addition to the respective biomaterials. (Unger, *et al.* Biomaterials, 2007).

that robust lumina are still forming. Furthermore, although these constructs are fully penetrated with *de novo* lumen structures, the lumina formed might not be patent or interconnected with each other, causing failure of the construct once implanted. An alternative prevascularization technique using decellularized omentum as a substrate for re-endothelialization has been investigated [20]. The ECM of the vascular axis was seeded with EPCs in a perfusion based culture system [19] and demonstrated vascular patency for one week following implantation [18]. However, the characterization of the vascular ECM following decellularization as well as immunogenicity of the construct need to be determined before this technology can be implemented *in vivo*.

2.3 ROLE OF ECM IN VASCULARIZATION

Endothelial ECM consists primarily of collagen type I, fibrin (or fibronectin) and a laminin rich basal membrane [61]. These proteins have distinct functions in regard to proliferation and migration, and stabilization during development and vascular healing. EC survival and proliferation are highly dependent upon adhesion to collagen I and fibrin [61]. Additionally, collagen and fibrin support chemotactic migration, and migration independent of chemokines [62]. Following injury, the basal membrane is first degraded, ECs then proliferate and migrate within tissues containing interstitial collagen (**Figure 8**) [63, 64]. Interactions with collagen cause a spindle-like morphology that will eventually reorganize into lumina over time [65, 66]. The transduction of mechanical forces through the ECM allows ECs to establish tension-based guidance pathways, leading to interconnected cords. This process can be conducted over long distances between cells, rendering cell-cell contact unnecessary [66]. Lumina then appropriate ECs from the interstitial matrix through the reestablishment of a basal lamina and form mature vascular structures [61]. Angiogenesis can be driven by chemical cues; however, ECM based

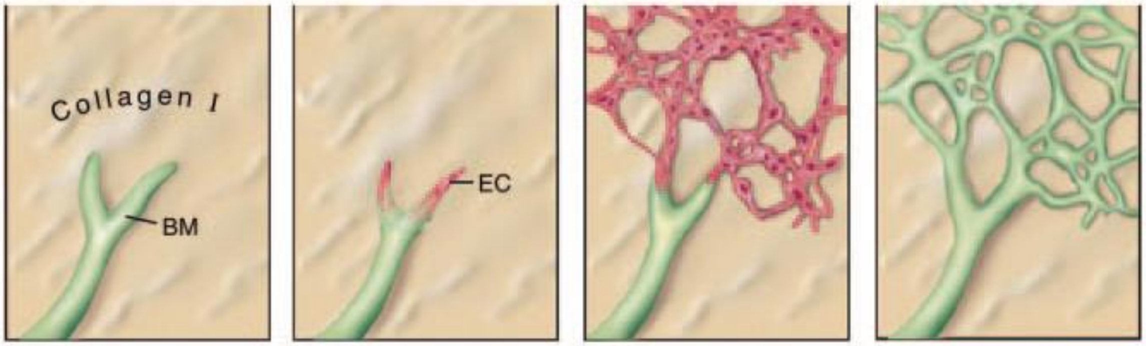

Quiescent blood vessel sequestered from collagen I by continuous basement membrane (BM)

Initiation of angiogenesis coincides with degradation of basment membrane and exposure of endothelial cells (EC) to collagen I

Collagen I drives morphogenesis of new vessel sprouts

Establishment of continuous basement membrane coincides with blood vessel maturation

Figure 8. Schematic of EC ECM involvement following injury. In this schematic diagram, collagen type I, but not laminin-1, activates Src and Rho and suppresses Rac and PKA through β1 integrins. This results in induction of actin stress fibers, disruption of VE-cadherin, and formation of precapillary cords. In contrast, laminin-1 induces Rac and PKA and suppresses Rho and, therefore, does not provoke morphogenesis (top). These marked distinctions in signaling by collagen type I ("fire") and laminin-1 ("ice") suggest a mechanism through which degradation of basement membrane and exposure of activated and proliferating ECs to collagen type I initiates morphogenesis of new capillary sprouts (bottom). (Davis and Senger, Circ. Res., 2005).

mechanochemical control can dominate these cues based on its ability to control cell fate [67]. This characteristic has been demonstrated through prevascularized methods during which ECs were able to successfully organize a vascular construct independently from angiogenic factors [57, 58]. Another important function of the ECM is to sequester cells. Research has demonstrated that the conformation and orientation of fibronectin are key components in EC cell adhesion [68]. This important finding, intimates at the importance of being biomimetic not only in biochemical composition, but also in spatial architecture. Overall, the ability of endothelial ECM to direct EC fate makes scaffold composition a significant characteristic to define in a vascular construct.

2.3.1 Decellularization Methods

One tissue engineering method that exploits the biochemical and mechanical properties, as well as architecture of native ECM is decellularization. Generally decellularization methods aim to remove the cellular components from harvested tissue, including surface markers, while leaving the ECM proteins intact. This results in a biomimetic construct composed of a variety of ECM components that synergistically provide an ideal environment for cellular homeostasis that is devoid of immunogenic markers. In addition to immunogenicity, research has demonstrated increased calcification due to cellular components in vascular constructs [69], making removal of these components paramount to long-term success. A wide number of techniques, including thermal, chemical, and enzymatic, have been used to decellularize a variety of tissues for regeneration in muscle [70, 71], vasculature [69], nerve [72-75], cardiac muscle [76], and bladder [2, 20]. Although different processes have been used to decellularize tissue, each has its own caveats which dictate their efficacy. This behavior has been demonstrated through decellularized nerve constructs for peripheral nerve injury. Thermal decellularization can effectively remove cells from tissue but fails to remove cellular debris that can still elicit an immune response and delay regeneration. Chemical decellularization on the other hand can effectively remove cellular components from the substrate, but can damage the ECM such that regeneration is hindered. To compensate for these shortcomings, research conducted previously in our lab has demonstrated that an optimized acellular (OA) protocol can be implemented to effectively remove cellular components while preserving the 10 μm diameter basal laminae (**Figure 9**) [73, 74]. Recently researchers have utilized a perfusion based method of decellularization to expedite cellular removal (**Figure 10**) [76]. Although this method was able to rapidly clear cellular components from rat heart tissue, the patency of the remaining lumen was not evaluated.

The use of decellularized constructs in vascular engineering has largely focused on the formation of large vessels as substrates for bypass grafts [69]. Researchers first decellularize vascular grafts using detergent or enzymatic processes then re-endothelialize the tunica intima [69]. Such methods have been able to create grafts that stay patent and completely re-endothelialize without calcification, thrombogenic, or immunogenic complications for up to 90 days [77, 78]. Decellularized constructs have also been used to differentiate progenitor cells into endothelial lineages. Kaushal *et al.* used EPCs to successfully re-seed porcine iliac vessels into patent grafts [79]. Lozito *et al*. have used ECM from a decellularized EC monolayer to differentiate MSCs toward EC lineages [80, 81]. Thus far, only Schultheiss *et al.* have applied the use of decellularized tissues for capillary vasculogenesis, utilizing a prevascularization model [18-20]. These researchers used bladder, then small intestine submucosa (SIS) ECM as a substrate for re-endothelialization using a pulsatile flow system. Although they demonstrate that re-

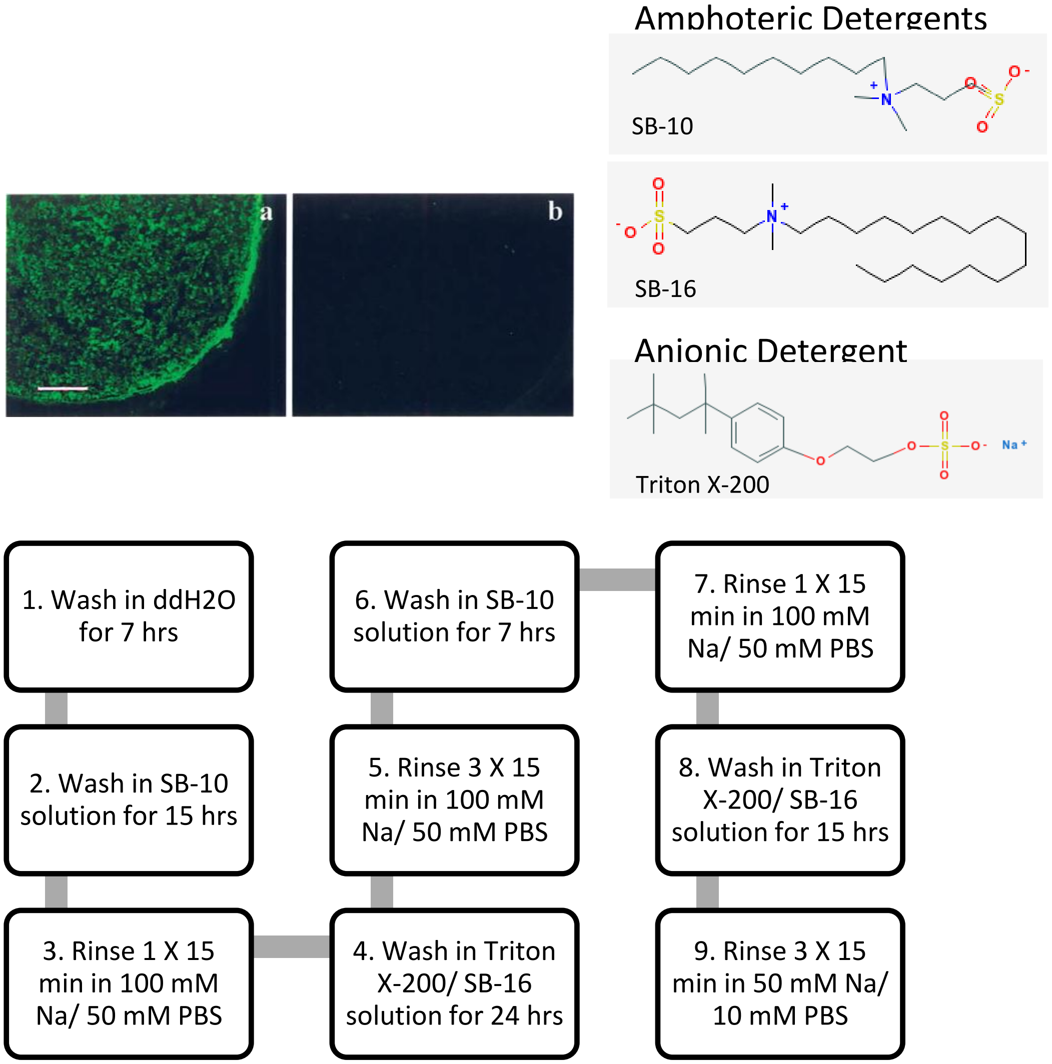

1. Wash in ddH2O for 7 hrs
2. Wash in SB-10 solution for 15 hrs
3. Rinse 1 X 15 min in 100 mM Na/ 50 mM PBS
4. Wash in Triton X-200/ SB-16 solution for 24 hrs
5. Rinse 3 X 15 min in 100 mM Na/ 50 mM PBS
6. Wash in SB-10 solution for 7 hrs
7. Rinse 1 X 15 min in 100 mM Na/ 50 mM PBS
8. Wash in Triton X-200/ SB-16 solution for 15 hrs
9. Rinse 3 X 15 min in 50 mM Na/ 10 mM PBS

Figure 9. Optimized acellular protocol. Removal of Schwann cells was evaluated by staining tissue cross-sections for S-100 protein. The fluorescence in (**a**) fresh nerve tissue was considerably more intense than in nerve treated by (**b**) the optimized protocol. (Hudson, Tissue Engineering, 2004). The optimized acellular method utilized both anionic and amphoteric detergents in diffusion-based processing cycle. (Hudson *et al.*, 2004)

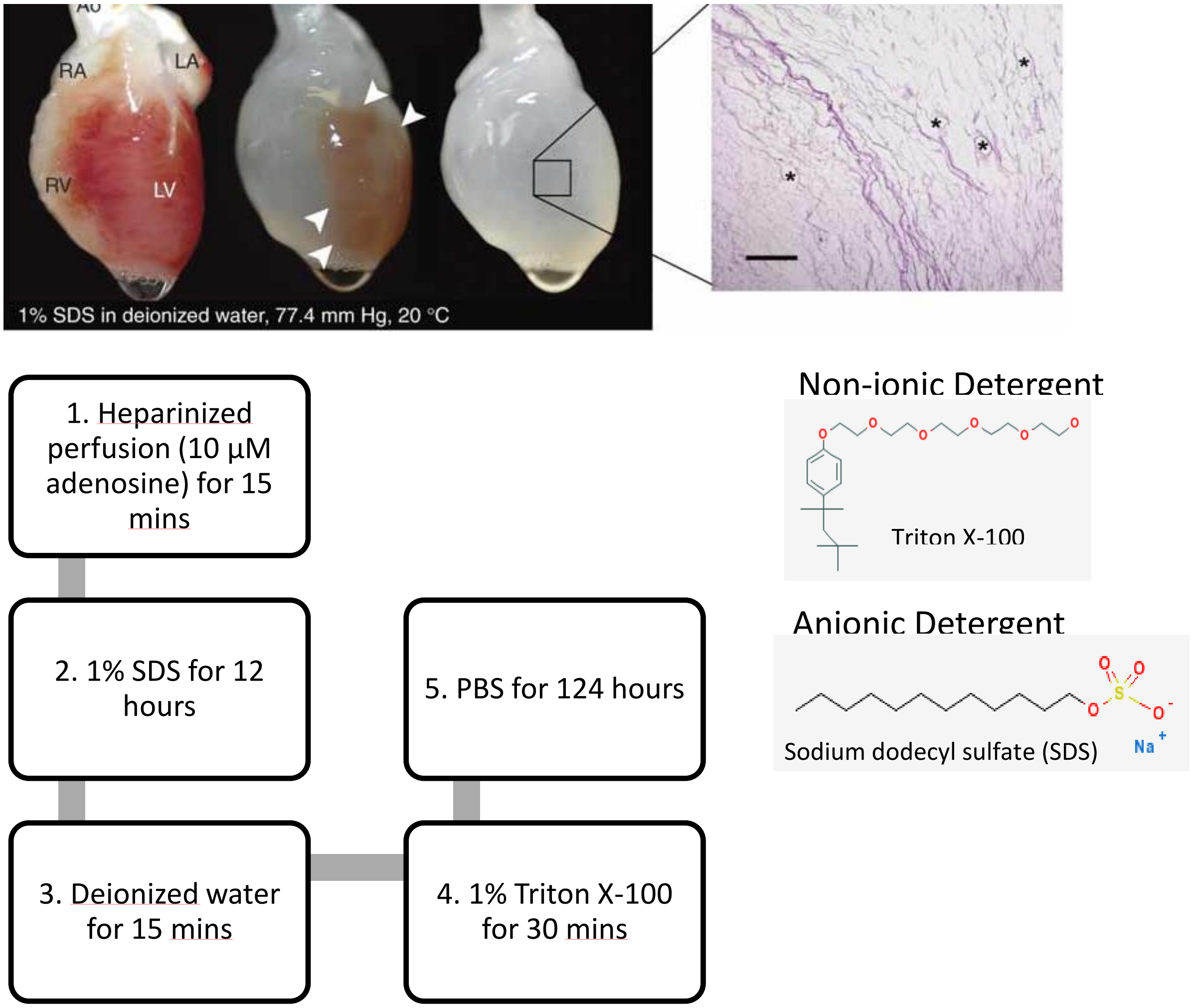

Figure 10. Perfusion SDS decellularization protocol. Photographs of cadaveric rat hearts mounted on a Langendorff apparatus. Ao, aorta; LA, left atrium; LV, left ventricle; RA, right atrium; RV, right ventricle. Retrograde perfusion of cadaveric rat heart using SDS over 12 h. The heart becomes more translucent as cellular material is washed out from the right ventricle, then the atria and finally the left ventricle. H&E staining of thin section of SDS-treated heart showing no intact cells or nuclei. Scale bar, 200 µm. SDS Protocol maintains large vasculature conduits (black asterisks). (Ott *et al.*, Nature, 2008). The SDS protocol utilizes both anionic and non-ionic detergents in a perfusion-based processing cycle.

endothelialization can be established in this method, the potential for thrombogenesis and immunogenesis have yet to be thoroughly evaluated. Thrombogenicity is a particularly poignant concern considering historical problems in microvascular patency in SIS grafts [82]. Additionally, the SIS construct is only 200 µm thick and better suited as a patch, or thin membrane replacement compared to a large tissue construct [19].

2.4 CELL LINEAGES USED IN VASCULARIZATION

Each vascular engineering method discussed thus far utilizes cells to promote vascularization and tissue regeneration. By dictating cellular behavior, researchers are able to help coordinate events that ultimately lead to enhanced tissue regeneration. However, the factors that mediate cellular behavior in a particular therapy need to be optimized for each cell line used. Systems that implement co-culture methods to help stabilize vascular systems further complicate matters, as culture conditions need to be ideal for each cell line used. Different types of endothelial lineages along with endothelial progenitor lineages and stem cell lineage have been used to promote vascularization [14, 83, 84]. Problems with isolation and cellular expansion of adult cell lines detract from the feasibility of implementing these cell lines in a clinical setting. Clinical cell lines need to be easily isolated and rapidly expanded, and then perform physiological roles in order to be of benefit to the donor. With these considerations in mind, researchers have started to evaluate the use of MSCs and EPCs in vascular therapies. However, further complications arise when using MSCs and EPCs relating to their potential capacity for unwanted differentiation. Thus, rigorous testing must be performed to ensure the benefits of these cells are realized without this potential for detrimental results. From a preliminary standpoint, using well-defined, adult endothelial cells is still advantageous, enabling the potential starting point for future use of progenitor lineages.

2.4.1 Mesenchymal Stem Cells

Stem cells present themselves as an ideal tool for tissue reconstruction based on their abilities to either self-renew or differentiate. Increased levels of telomerase in stem cells means their proliferation can be maintained at a high level, a desirable property when culturing tissues *in vitro* for future transplantation. Long scale-up times for fully differentiated cells is one of the limiting factors for clinical application of *in vitro* culture therapies. The most common therapy for articular cartilage defects in the knee is autologous chondrocyte transplantation [3]. In this procedure autologous chondrocytes are harvested from the patient in an initial surgery. These cells are then cultured in monolayers that are reconstructed and transplanted back into the patient after three weeks. Although a generally successful operation for these patients, this method of differentiated cell culture is clearly not applicable to injuries that are more temporally constrained. This method is also not ideal for injuries to tissues that will be significantly impaired by the initial cell harvest.

Embryonic stem cells (ESCs) are pluripotent cells capable of differentiating into all three germ layers in the body [85]. However, despite the potential benefits of using ESCs, their use is extremely controversial, rendering them dormant in the clinical setting. Conversely, MSCs represent an autologous cell line that can differentiate into a number of lineages [86]. Without ethical constraints, and relative ease of extraction, MSCs represent a clinically feasible therapy. MSCs have been successfully differentiated into endothelial cell lines using growth factors [87] or in a controlled media using ECM cues [80, 81]. They can also differentiate further to smooth muscle cells, which could be of benefit to stabilizing ECs into lumen [80]. These cells have also been shown to help in vascularization pathways following injury. MSCs are recruited to the circulatory system following trauma and ischemia, and then participate in healing and angiogenesis [88-92]. Collateral perfusion can occur due to the paracrine effects of MSCs which also enhance EC recruitment [88, 90, 91, 93]. Furthermore, MSCs are an attractive cell line to employ following ischemia based on an heightened ability to engraft *in vivo* following exposure to a hypoxic environment [94].

2.4.2 Endothelial Progenitor Cells

EPCs have been used extensively in cardiovascular therapies. These cells are able to home to sites of ischemia and participate in neoangiogenesis (**Figure 11**) [83, 84]. Asahara *et al.* first isolated these cells from human peripheral blood after which these cells differentiated into adult ECs [95]. One benefit of using EPCs is their inability to differentiate into non-hematopoietic cell lines. This is in stark contrast to MSCs, which have the propensity to differentiate into a multitude of lineages, a behavior which could lead to unwanted differentiation. In addition to being able to differentiate into endothelial cells, EPCs also promote re-endothelialization through paracrine factors [96]. EPCs are also able to cover acellular vessels in *in vitro* then form neovessels upon implantation [79]. Additional benefits of using EPCs over mature ECs are favorable survival and responsiveness to growth factors [63]. Although the mechanisms by which EPCs home, migrate, differentiate and ultimately establish an environment conducive towards endothelialization are nebulous, their use in biology, particularly re-endothelialization, is appealing.

2.5 FLUID SHEAR STRESS ON CELLS

A well-known factor that contributes to EC cell fate is shear force. Ott *et al.* have demonstrated that ECs cultured in the presence of fluid shear stresses of 1-2 dynes/cm^{2}for

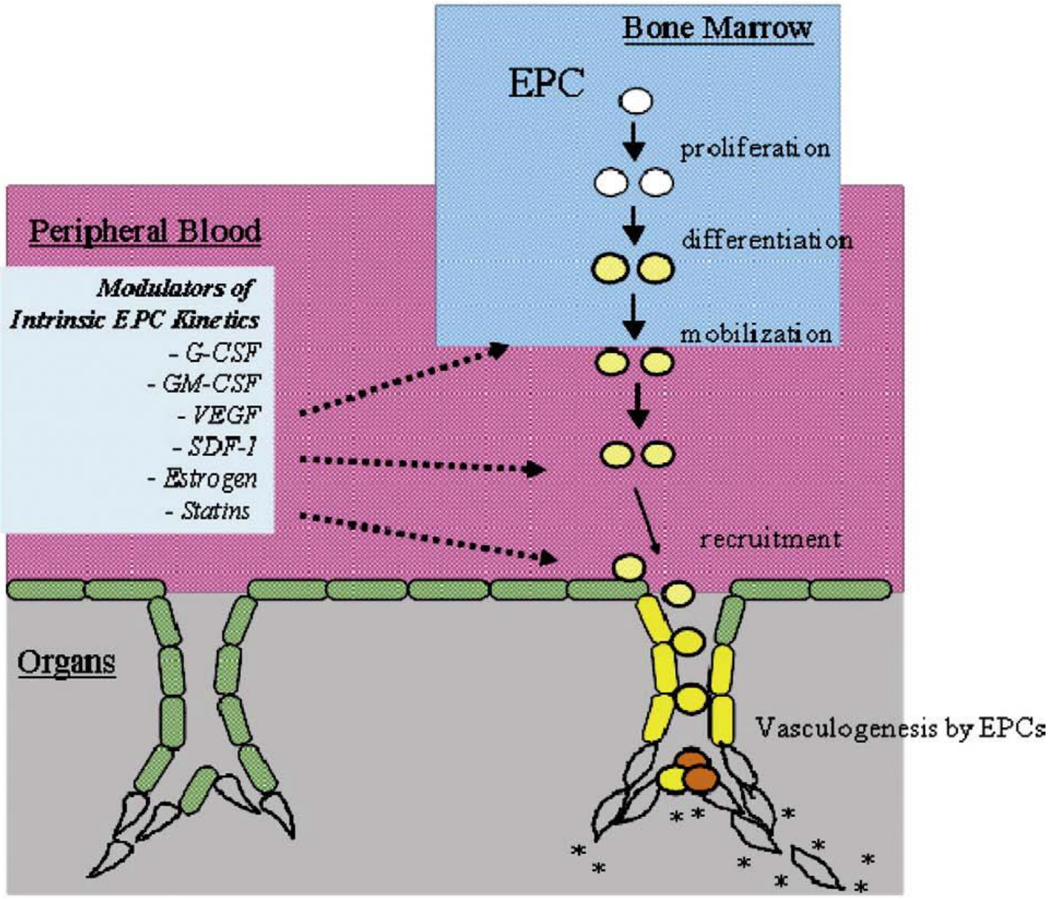

Figure 11. Mechanism of EPC-mediated postnatal neovascularization. Circulating EPCs mobilized from bone marrow are recruited into the foci of neovascularization and contribute to new blood vessel formation. The intrinsic EPC activity can be augmented by certain cytokines, growth factors, and pharmaceutical agents. EPC indicates endothelial progenitor cell; G-CSF, granulocyte colony-stimulating factor; GM-CSF, granulocyte macrophage colony-stimulating factor; VEGF, vascular endothelial growth factor; SDF-1, stromal cell-derived factor 1. (Kawamoto and Losordo, 2008).

24 hours, followed by 25 dynes/cm^2 for three days have better retention in vascular constructs once implanted into patients [33]. One suspected reason for this behavior is that when subjected to fluid shear stress ECs change morphology and align their actin filaments in the direction of the applied stress (**Figure 12**) [34, 35]. Shear stress not only directs morphological change but also affects gene expression in ECs, upregulating prostacyclin secretion [36], a marker for healthy endothelial activity.

In addition to dictating cellular fate in ECs, shear flow also influences stem cell differentiation. Much work has been accomplished demonstrating the ability to direct stem cell differentiation using applied forces [97]. Forces applied to cells through substrate interactions [98], micropipetting [99], and shear stress [100] have all been found to differentiate stem cells down particular lineages. Appropriately, shear stress has been found to differentiate both embryonic stem cells (1.5-10 dyn/cm^2) [101] and MSCs (15 dyn/cm^2) [100] towards EC lineages. Clearly, when aiming to connect a vascular construct to the host vascular system, preconditioning with shear stress has important advantages.

2.6 ANALYSIS OF VASCULAR NETWORKS

2.6.1 Vascular Casts Used to Elucidate Vascular Structure

Vacular Casts (VC) have been used to image and explore the morphology of vascular networks and structures since the 1980’s [102, 103]. These permanent representations of the vascular luminal space are obtained after the process of perfusing the vascular system to remove blood, injecting the vasculature with resin, allowing the resin to polymerize, and finally removing the surrounding tissue (Vascular Corrosion Casts or VCC), or optically clearing the surrounding tissue.

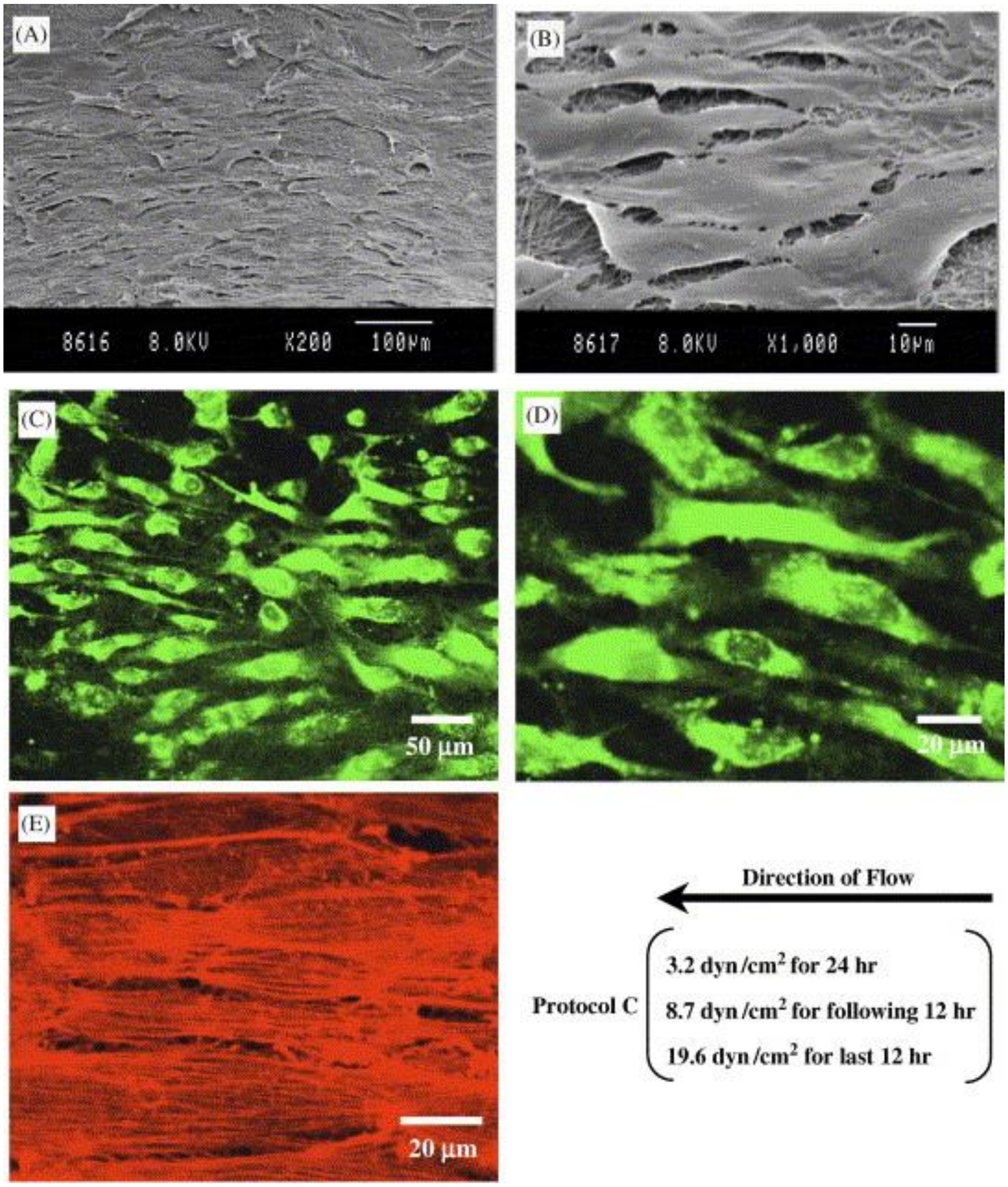

Figure 12. Gradual shear stress affects HUVEC morphology. Tissue morphology of luminal surface of HUVEC-seeded graft subjected to 12 h shear stress of 19.7 dyn/cm^{2}after 12 h stress loading of 8.7 dyn/cm^2 **(***Protocol C***)**. SEM images; A and B. CLSM images; DiO-labeled cells, C and D; actin fibers, E. (Inoguchi *et al.*, 2007).

Fully perfusing the vascular network with the casting solution is of vital importance and determines the accuracy and usefulness of the cast as a model. To ensure full perfusion and filling of the lumen, different types of resin and different viscosities of resin have been investigated [104-108]. Often the tissue will also be heparanized to prevent blood clotting [107], occlusion of microcirulatory beds [109], and minimize formation of microthrombi [109]. In addition, the tissue is sometimes perfused with a fixative to help retain vascular structure [104, 105]. Given the lengthy process of making a cast (around a week depending on corrosion or clearing methods) [104, 105, 107, 109, 110], ensuring a complete cast is vital.

These polymer casts can then be used to accurately visualize vascular structures down to the capillary scale (**Figure 13**). Scanning Electron Microscopy (SEM) and Confocal Microscopy techniques are the most commonly used to investigate the vascular structure preserved by the cast due to the high resolution images they are able to produce [109, 110]. Using stereo imaging in SEM [110, 111] and optical section stacking in confocal [112], three dimensional representations of the vascular network can be made. From these representations vascular properties including vessel dimensions, vessel densities, and branching patterns can be obtained and analyzed [110]. Additionally, VCs have been used to elucidate differences in damaged tissues, by evaluating vessel defects, truncations, and extravasation patterns [113]. These techniques provide a means to gain insight into the continuity, and thus functionality of the vascular network that remains following the decellularization of various tissues.

2.7 RESEARCH GOALS

The focus of this work has been to create a decellularized vascular scaffold that removes immunogenic components of the harvested tissue while maintaining the

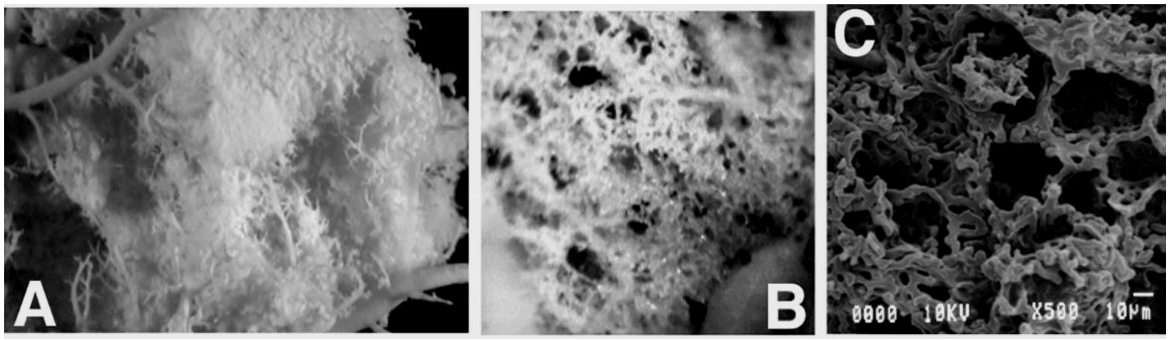

Figure 13. Images of acrylic corrosion casts of normal lamb pulmonary vasculature. Panels A –C depict lungs in which casts are made of all vessels including capillaries. Stereo microscopic images of normal corrosion casts (A and B) demonstrate the complexity of pulmonary vasculature, which is further revealed at the scanning EM level (C). (McMullan *et al.*, 2004).

biochemical availability and structural architecture necessary to support mature endothelial growth and vascular patency. This scaffold was subsequently used to investigate the ability for vascular patency to be rescued following re-endothelialization, and could potentially serve as a future tissue engineering product, as well as a system to investigate vascular engineering phenomena.

Chapter 3: Development and Characterization of a Decellularized Vascular Scaffold

3.1 INTRODUCTION

To create an optimized acellular vascular tissue construct, we needed to first determine for which tissue source a decellularization protocol would be developed. The decellularization protocol needed to effectively remove the cellular and immunogenic components of the harvested tissue, while leaving behind a working vascular network, comprised of ECM proteins—upon which optimal vascular engineering methods could be performed. Highly vascular lung tissue was selected for subsequent experimentation. Subsequently, the OA chemical decellularization protocol that was previously developed by Dr. Schmidt's lab was evaluated for its ability to decellularize lung segments of differing thicknesses. A protocol was then developed and analyzed for cellularity using qualitative histological methods, as well as quantitative DNA concentration, and then its ability to preserve the ECM matrix, both in biochemical composition—determined through immunohistochemistry, as well as patency—determined through VCC. The OA protocol was simultaneously compared to two alternative decellularization methods, chosen for their ability to decellularize tissue that contains a working vascular axis. Having outperformed the alternative decellularization methods tested, the OA method was chosen for subsequent experiments involving immunogenicity—evaluated by using an allogeneic implantation model.

3.2 RESEARCH DESIGN AND METHODS

3.2.1 Selecting the Optimal Tissue Source

To create a construct that had an intrinsically organized vascular structure, we first evaluated potential tissue sources. We selected liver and lung tissue based on their high levels of vascularization, large vascular axes, and thickness over 200 microns. As discussed earlier, tissue constructs that have a thickness of less than 200 microns may be vascularized by the host before significant necrosis can occur; hence, choosing a tissue construct that exceeds this critical size will demonstrate the effectiveness of our technology.

All animal experiments were performed in compliance with the "Guide for the Care and Use of Laboratory Animals," [114] and IACUC standards (according to protocol AUP-2010-00103). Female Fischer rats (175-200g) (Harlan, Indianapolis, IN) were given intraperitoneal injections of 1000U per kg of heparin sodium injection (TW Medical, Austin, TX) 15 minutes prior to 100/10 mg per kg of ketamine/xylazine cocktail (Bioniche Teoranta Inverin, Co., Galway, Ireland/Akorn Inc., Decatur, IL). The animals were perfused with phosphate buffer solution until liver and lungs were blanched. Whole lung and liver were excised from the animals and placed in 4^{o}C buffer. Next, the singular left lung lobe was isolated including its vascular axis using a stereoscope (Leica Zoom 2000) to allow for subsequent perfusions on a single lung lobe (**Figure 14**). Liver tissue was significantly more complex when attempting to harvest a single lobe, so each lobe’s vascular axis was not well intact. These tissues were then sectioned into smaller segments with varying thicknesses (1 mm, 2 mm, and 5 mm) to impart information regarding the efficacy of our technique, and then subjected to decellularization processing using the optimized acellular method and histological comparisons (H&E, laminin, DAPI) with fresh tissue counterparts. Results of this primary selection excluded liver from subsequent analyses.

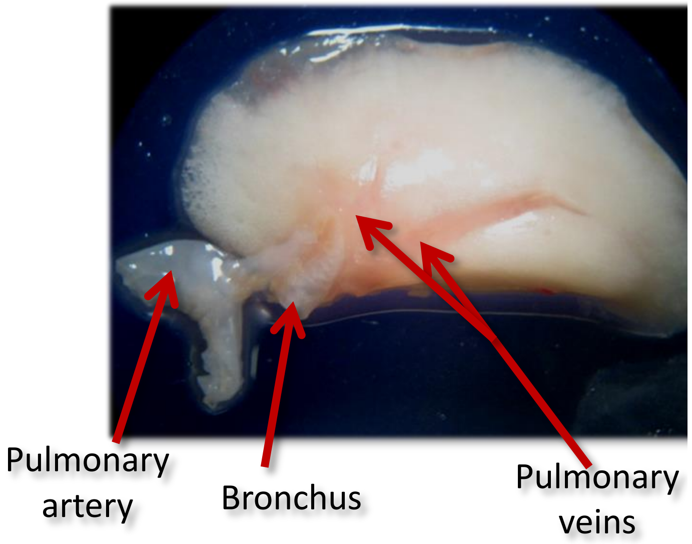

Figure 14. Isolated left lung lobe following heparinization, blanching, harvest, and isolation. An intact vascular axis, as well as bronchus can be visualized under a stereoscope.

3.2.2 Decellularization Selection

Three chemical decellularization methods were selected for comparison. The first method, optimized acellular (OA), was based off of a decellularization protocol developed previously in our lab for peripheral nerve decellularization [73]. This method was the only method optimized by changing the detergent incubation durations. The optimized protocol used in subsequent studies is outlined. Briefly, lung tissue was incubated in 125 mM sulfobetaine-10 (amphoteric) detergent for 24 hours followed by one rinse of 100/10 sodium/phosphate buffer for 15 minutes. Next tissue was incubated in a combination 0.14% Triton X-200 (anionic) and 0.6 mM sulfobetaine-16 (amphoteric) detergents for 48 hours followed by three rinses of 100/10 sodium/phosphate buffer for 15 minutes each. Tissue was then incubated in SB-10 solution for 15 hours followed by one rinse of 100/10 sodium/phosphate buffer for 15 minutes. Tissue was then incubated in Triton X-200/SB-16 solution for 24 hours followed by three rinses of 50/10 sodium phosphate buffer. All incubation and rinse steps were performed on a vertical rotator. The next method, hereby referred to as the PSDS method, was a taken from a protocol developed by Ott *et al*., effective in decellularizing heart tissue (**Figure 15**) [76]. Lung tissue was first cannulated prior to perfusion of detergents. Next, 1% SDS (anionic) in deionized water was perfused through the tissue for 12 hours, followed by 15 min perfusion of deionized water, then 30 min of 1% Triton X-100 (nonionic) in deionized water. Finally, PBS was perfused through the tissue for 124 hours to ensure the removal of residual detergent. The final method (POA) combined the detergents and timings of the original OA method, but delivered the detergents utilizing perfusion.

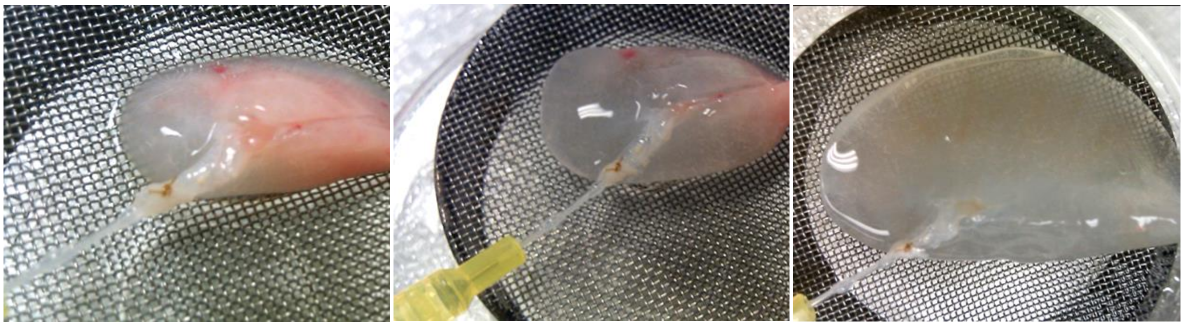

Figure 15. Perfusion-based decellularization using the PSDS protocol on isolated rat lung. A rapid clearing of the tissue was observed over one hour following the perfusion of 1% SDS solution in water. Note that swelling occurred over time as a result of the use of water as the solvent for the detergents.

3.2.3 Histological Characterization of Decellularized Lung Tissue

Histology was the first analytical strategy to assess the composition of lung tissue following decellularization. For all histological studies three unprocessed and processed tissues from each method were fixed in 4% paraformaldehyde for 4 hours, and then cut transversely into 20 µm thick sections using a cryostat (Microm HM 550). Hematoxylin and eosin (H&E) staining was subsequently performed on these samples and fresh lung as control. Representative images of each tissue were then selected for evaluation of general morphology.

Staining for the ECM proteins laminin and fibronectin was performed using standard immunofluorescence imaging procedures with antibodies against fibronectin (Sigma, F0916, 1:100) and laminin (Sigma, L9393, 1:400) on 20 µm thick sections of processed and unprocessed tissues. Immunofluorescence imaging against the endothelial glycoprotein, CD-31 (Pharmingen, 550300, 1:50), α-smooth muscle actin (Abcam, ab7817) with DAPI staining for nuclei was performed on decellularized and unprocessed tissue sections. Secondary antibodies attaching to either rabbit or mouse IgG and bound to the fluorophores, Alexa-Fluor 488, and Alexa-Fluor 568 were subsequently bound (at 1:400). In each study a negative control consisting of only the secondary antibodies used was used to prevent false-positive signal interpretation. Representative images of each tissue were then visualized on an Olympus IX70 (Olympus America, Melville, NY) inverted microscope, and captured with an Optronics (Goleta, CA) MagnaFire digital color camera. For each stain, a fixed exposure time was used.

3.2.4 DNA Quantification

To quantitatively compare the efficacy of the different decellularization methods used to remove cellular material, we isolated the DNA remaining from our scaffolds compared to fresh lung tissue. Processed and unprocessed lung tissue (three lungs per technique) was rapidly frozen with liquid nitrogen and crushed using a mortar and pestle. Three 50 mg samples per lung were then incubated in 40 mM NaOH solution for 5 hours at 90^{o}C, and then neutralized with Tris-HCl to a pH of 7.8. These samples were then centrifuged at 500g for 15 min. The supernatant was then drawn and run with a NanoDrop machine to read the optical density at 260 nm and calculate the corresponding ds-DNA concentration.

3.2.5 Vascular Casting

General Vascular Corrosion Casting

Mercox II CL-2R resin with catalyst (40% benzoyl peroxide) was injected via syringe pump (KD Scientific, Model 200) (0.2 g catalyst/ 10 ml resin) at 2 ml/min into the vascular axis of six processed and two unprocessed tissues at 2 ml/min (**Figure 16**). The resin was allowed to polymerize in water baths at 65^{o}C overnight, after which the organic components were removed by chemical washes (25% potassium hydroxide 48 hours), and warm water washes to remove remaining tissue. Photographs were taken using a standard digital camera through a stereoscope (Leica Zoom 2000).

Quantitative VCC

The presence of capillaries in the remaining plastic structure was visualized using scanning electron microscopy (SEM). The plastic molds were air dried for 24 hours in the hood, then coated with 20 nm platinum palladium for observation with SEM (Zeiss Supra 40 VP) with an acceleration voltage of 5 kV. A total of 32 images were taken for each decellularization method, and then normalized to account for the same total surface area for the particular decellularization method. Four researchers independently analyzed the

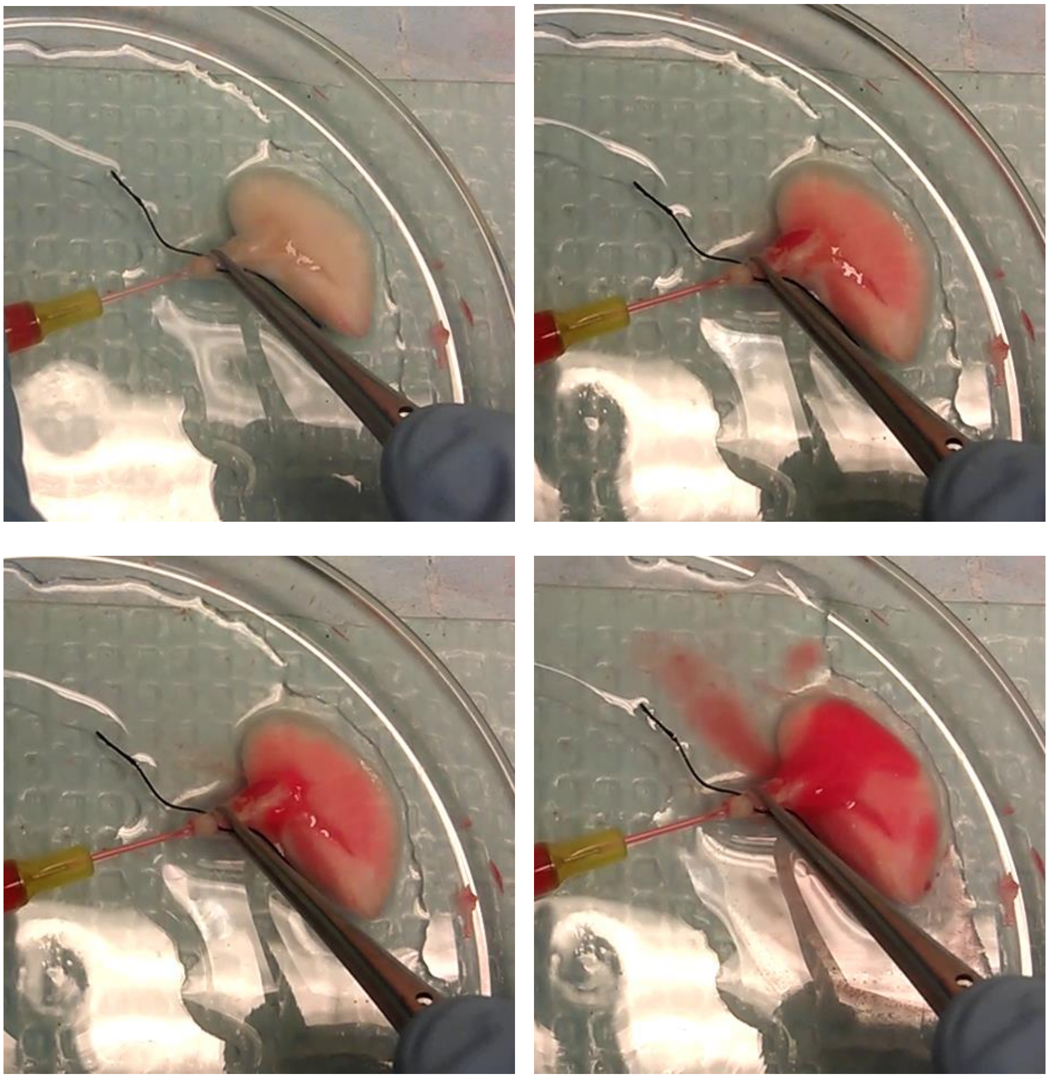

Figure 16. Mercox injection in the pulmonary artery of decellularized lung tissue. Perfusion demonstrates uniform filling, and exiting through the pulmonary vein.

images for extravasations of the resin from the luminal space. Extravasations were counted and sorted by diameter in four categories: <10 µm, 10-20 µm, 20-30 µm, and > 30 µm. These counts were normalized with respect to the area of the image, and then averaged for each decellularization group. Each decellularization group was then averaged among the four researchers. Total extravasational volume was determined by estimating the average diameter of extravasations found in each category as 5µm, 15 µm, 25 µm, and 30 µm. A paired t-test was used to determine if statistical significance existed between the researcher's counting for each decellularization group. An F-test was used to determine variance significance followed by a Student's t-test to determine statistical significance between each decellularization group.

3.2.6 Testing Immunogenicity of an Optimized Acellular Vascular Scaffold

Following the extensive testing on the efficacy of our decellularization protocol, we were able to confirm that our OA vascular scaffold was superior in maintaining vascular patency while removing the potentially immunogenic cellular material. Subsequent testing was performed using this superior decellularization protocol.

To gain a practical understanding of the potential immunogenicity of our scaffold following the OA process, we developed an *in vivo* allogeneic implantation model. 24 lungs from 175-200g female Fischer rats (Harlan, Indianapolis, IN) were isolated and decellularized using the OA process, as mentioned previously. 12 lungs were implanted subcutaneously into 175-200g Lewis rats (Harlan, Indianapolis, IN); whereas 12 were implanted subcutaneously into Fischer rats of the same size as an isogenic control. Rats were anesthetized with isofluorane vapor at 4% induction and 2.5% during surgery. A skin incision was made on the right flank of 2-5 month old Lewis rats where either decellularized or unmodified lung tissue was anchored to the thigh via 5-0 sutures

(Ethicon). Following surgery, animals received injections of buprenorphine, or saline when necessary. An equal number of animals were maintained for one and four weeks, after which they were euthanized and the implants were excised for histological analysis as described for tissue harvest. No complications arose. Basic H&E staining was used to assess general signs of immunological rejection. Additionally, thin tissue sections were obtained and used to determine the number of monocytes and macrophages (mouse anti-macrophage, Millipore, MAB1435, 1:50) within the grafts, using standard immunohistochemistry protocols [74]. Fifteen images from six sections of three tissues of both allograft and isograft were compared to each other for immune positive cell counts. These counts were then compared to the total number of cells in the field of view. Total cell counts were determined by running the DAPI image through a convolution filter in ImageJ (Bethesda, MD), then inverting and thresholding the image before applying a watershed process, then finally using the analyze particles application.

3.3 RESULTS

The optimization of our decellularization protocol—to create a scaffold devoid of cellular markers while still maintaining a vascular architecture down to the capillary scale—began by testing the efficacy of an already optimized acellular protocol for nerve tissue. Although optimized from nerve and tested on lung and liver—which are vastly different in terms of thickness, and area—the optimized acellular protocol provided excellent clearing of cellular components while maintaining structural integrity of the ECM of lung tissue of different thicknesses and arrived at our OA protocol. We then extended the detergent incubation times to account for the thicker tissue source. The extent to which the cellular material was removed, and the architecture was preserved in lung tissue was analyzed in greater detail using both qualitative histological means, as well as quantitative methods. H&E staining and immunohistochemistry revealed a comparable architecture to unprocessed tissue, and the ability for antibodies targeting specific domains on the ECM to bind and signify bioactivity, while demonstrating the removal of nuclei. As a comparison, alternative decellularization methods were also analyzed and revealed the superiority of the OA process. Quantification of the removal of nucleic material, the protein remaining, and the damage to the vascular network following the OA process were then analyzed using DNA isolation, and qVCC techniques—again demonstrating the superiority of the OA method compared to alternative methods. Following characterization, the OA vascular scaffolds demonstrated a lack of immunogenicity using an *in vivo* allogeneic model, with isogenic comparison.

3.3.1 Optimized Acellular Decellularization

Segments of lung and liver (1, 2, and 5 mm thicknesses) were decellularized using the optimized acellular protocol developed in our lab previously. Initial analysis using H&E, and immunostaining against laminin with DAPI counterstain revealed the ability for the optimized acellular method to effectively remove cellular components of each thickness of lung (**Figures 17, 18**). Liver segments failed to decellularize in more than a few hundred microns of the tissue, even in thinner segments (**Figure 18**). Following decellularization of segments, the singular left lung lobe was harvested and decellularized in its entirety. Although largely effective at removing cellular material, there were still residual components found in the tissue. To combat this problem, and spurred by the preservation of ECM even in thin lung segments, the detergent incubation times were doubled. The doubled detergent incubation time removed cellular material without the loss of ECM composition, as seen following histology and the attenuated signal of

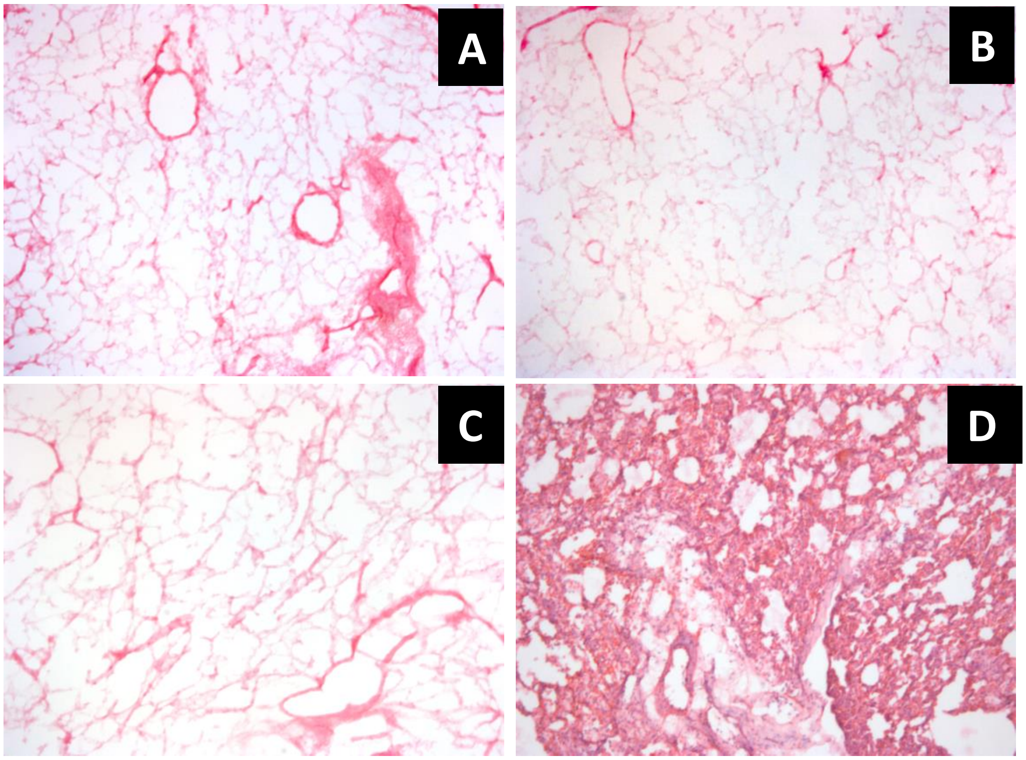

Figure 17. H&E staining for optimized acellular decellularized lung segments of different widths. H&E staining reveals an organized structure remains across all thicknesses of lung 1mm (A), 2mm (B), and 5mm (C) versus fresh lung (D), whereas nuclei are removed.

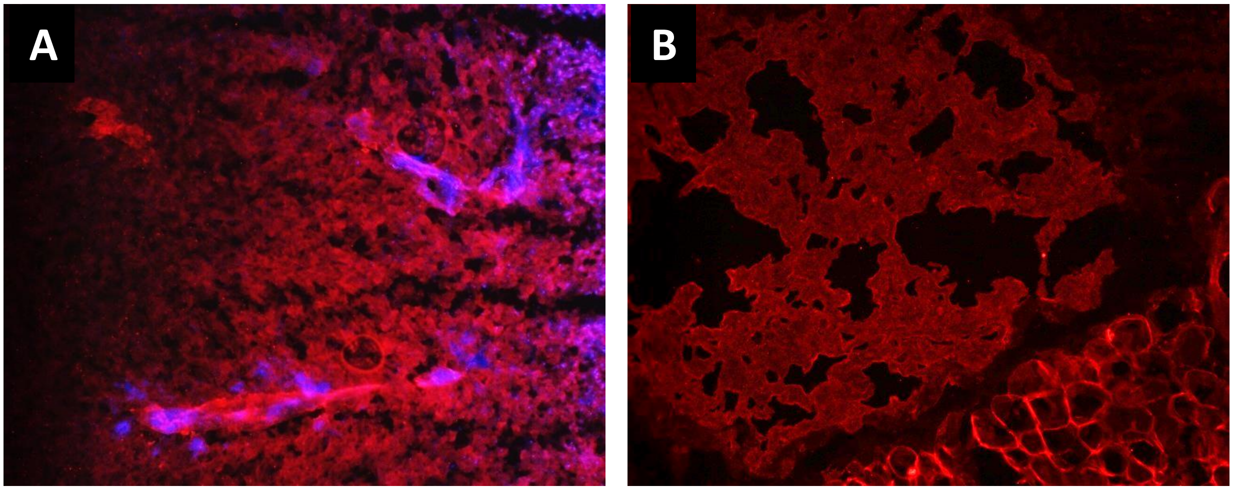

Figure 18. Initial decellularization of liver and lung tissue. Overlay of DAPI (blue) and laminin (red) staining for liver (A) and lung (B) following the OA protocol. The liver displays a gradient of decellularization from the exterior (left) to the interior (right) whereas the lung is completely decellularized (10x).

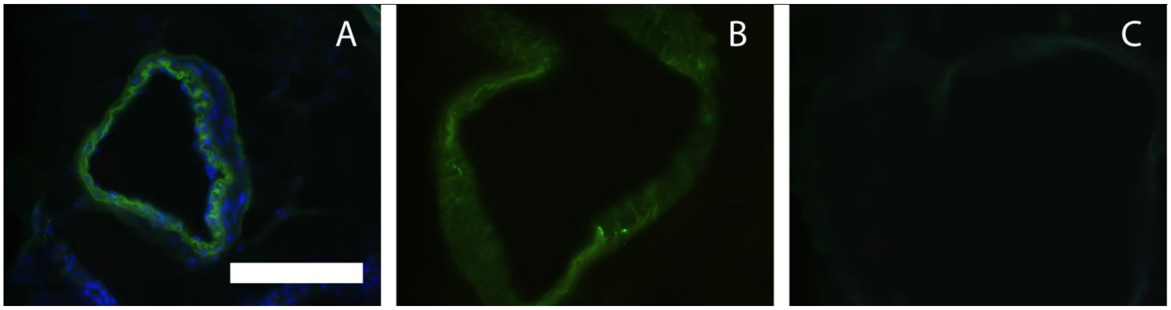

Figure 19. Increasing OA detergent incubation time improves decellularization. Staining against CD-31 (green) with DAPI (blue) of fresh (A) and decellularized (B, C) lung following OA processing at standard timing (B) and lengthened timing (C). Standard timing OA decellularization removes the presence of nuclei, but fails to remove the transmembrane glycoprotein CD-31, whereas long-time OA decellularization effectively removes all cellular components. Scale bar = 100 µm

cellular markers using immunohistochemistry (**Figure 19**). Further characterization of the tissue was then compared to other decellularization protocols.

3.3.2 Optimized Acellular Process Effective at Removing Cellular Material while Preserving ECM Content

Hematoxylin and Eosin Staining for General Ideas on Tissue Composition

Several qualitative histological methods were implemented to assess the composition of lung tissue following different decellularization protocols. The first most general method used was H&E staining—to examine the broad architecture of the lung in comparison to fresh lung samples (**Figure 20**). H&E demonstrated that nucleic material was removed and ECM persisted in each of the decellularized lungs. An organized structure similar to native tissue was visualized following tissue processing using all the decell methods.

General continuity of basal ECM was found following each decellularization method. Some erratic hematoxylin staining was seen in following the PSDS method and to a lesser extent, the POA method; this however, was likely due to anionic SDS detergent binding to the basal proteins, as opposed to genetic material—which will be thoroughly discussed in the following section.

Immunohistochemistry Demonstrates ECM Activity and Cellular Removal

Immunohistochemistry techniques also provided a qualitative representation of cellular material left over. As mentioned in the previous section, the first procedure based on the optimized acellular protocol for nerve was ineffective in removing residual fragments of cellular material; although effective in removing nuclei. Immunofluorescence evaluation reveals the removal of nucleic material. Some positive DAPI staining was seen in perfusion decell groups (**Figures 23, 24**); however, this was likely a result of residual anionic detergents remaining in the tissue, similar to the H&E

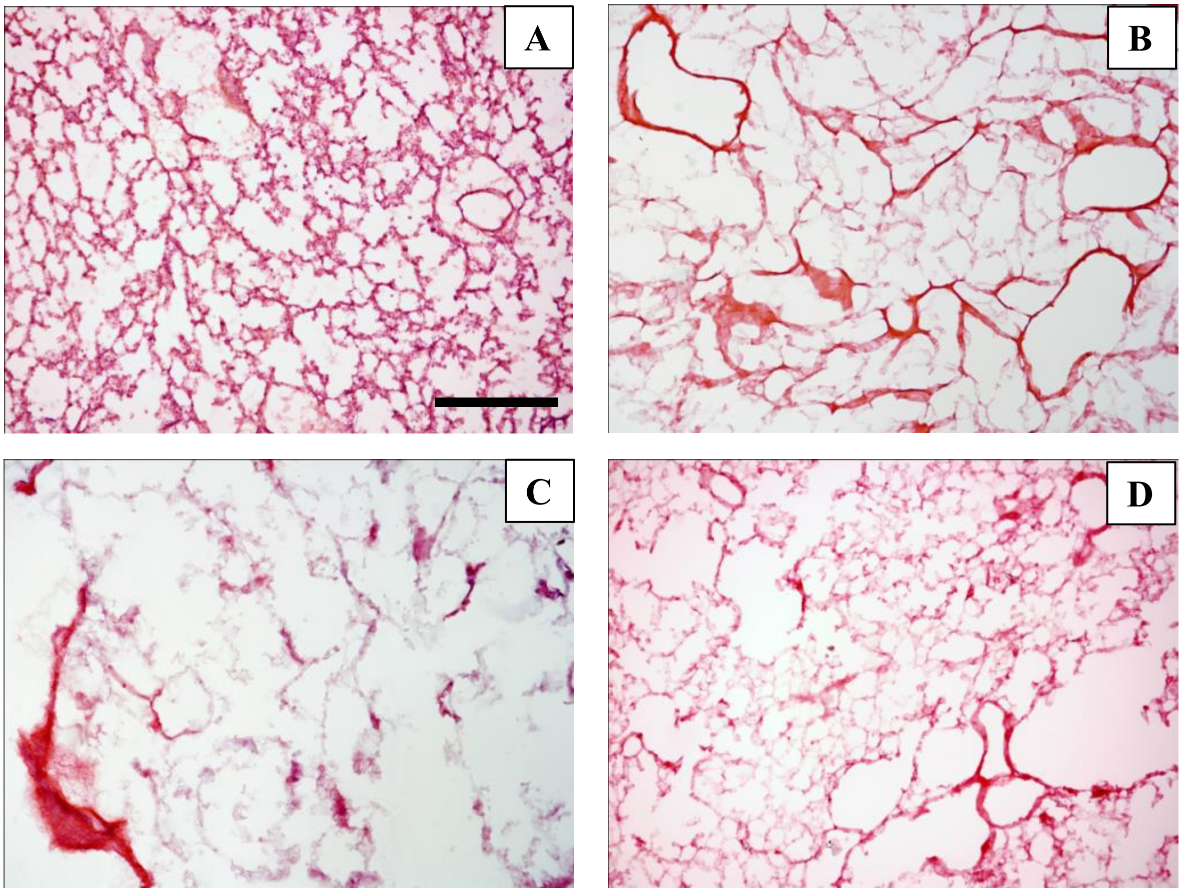

Figure 20. Hematoxylin and eosin (H&E) staining following different decellularization methods on lung tissue. Fresh (A), diffusion OA (B), PSDS (C), POA (D) lung were examined. No presence of intact nuclei remained, however, in PSDS processing, basophilic staining from hematoxylin was observed. ECM preservation was most continuous in the OA groups (B, D) compared to the Taylor method (C). Scale bar = 500 µm

staining. Immunofluorescence signal using antibodies targeting the endothelial marker CD-31 and α-SMA was greatly diminished following decellularization, although some signal was seen in the POA group (**Figures 21, 22**). In contrast, positive signal for antibodies for laminin and fibronectin, demonstrated a bioactivity of these domains in each decellularization method used comparable to fresh lung tissue (**Figures 21, 23**).

3.3.3 DNA Quantification Confirms Removal of Nucleic Material Following Decellularization

Fresh lung DNA isolation was compared to DNA isolated from segments of lung following decellularization (**Figure 25**). Spectral analysis and quantification confirmed the removal of DNA observed in qualitative histological methods. DNA concentration from each decell group was significantly lower than fresh tissue. OA, PSDS, and POA lungs resulted in 85%, 91%, and 87% less ds-DNA than fresh tissue respectively. Each decellularized DNA concentration was significant to fresh tissue ($p<0.0000001$), and significance was observed between the OA and PSDS group ($p<0.0001$). Importantly, the 260/280 nm wavelength ratios of OA, PSDS, and POA lungs were 1.75 ± 0.06, 2.07 ± 0.15, and 1.87 ± 0.09 respectively, compared to 1.74 ± 0.04 for fresh tissue and close to 1.8, signifying a pure sample of DNA without protein interference.

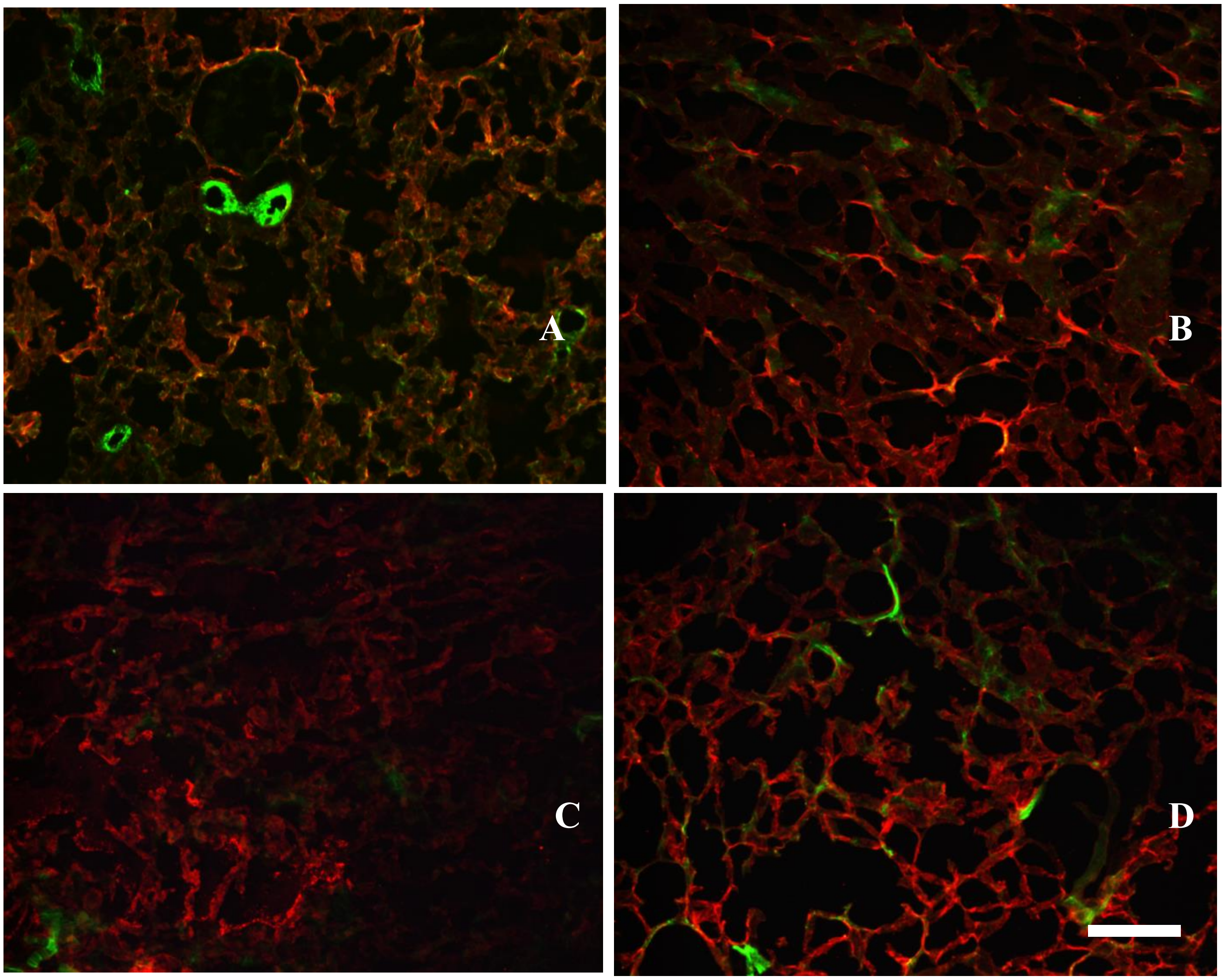

Figure 21. CD-31 and laminin immunostaining following different decellularization methods on lung. Immunostaining against laminin (red), and the endothelial marker CD-31 (green) demonstrates basal lamina remains whereas cellular signal is diminished following decellularization of lung tissue using different methods (A, fresh lung; B, OA method; C, PSDS method; D, POA method) Scale bar = 200 µm

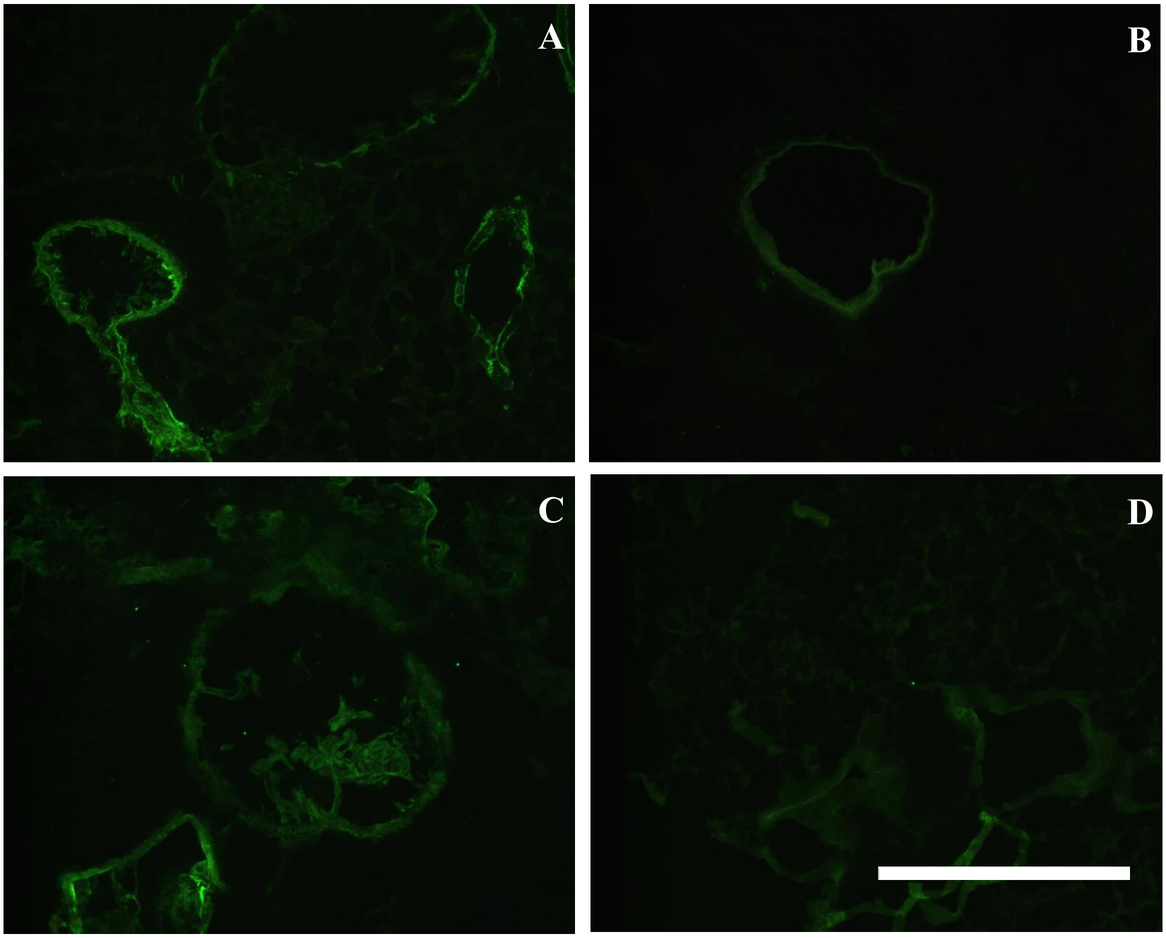

Figure 22. α-smooth muscle actin immunostaining following different decellularization methods on lung tissue. Staining against α-smooth muscle actin demonstrates attenuation of the cellular component following decellularization methods (A, fresh lung; B, OA method; C, PSDS method; D, POA method) when compared to fresh tissue (A). Scale bar = 500 µm.

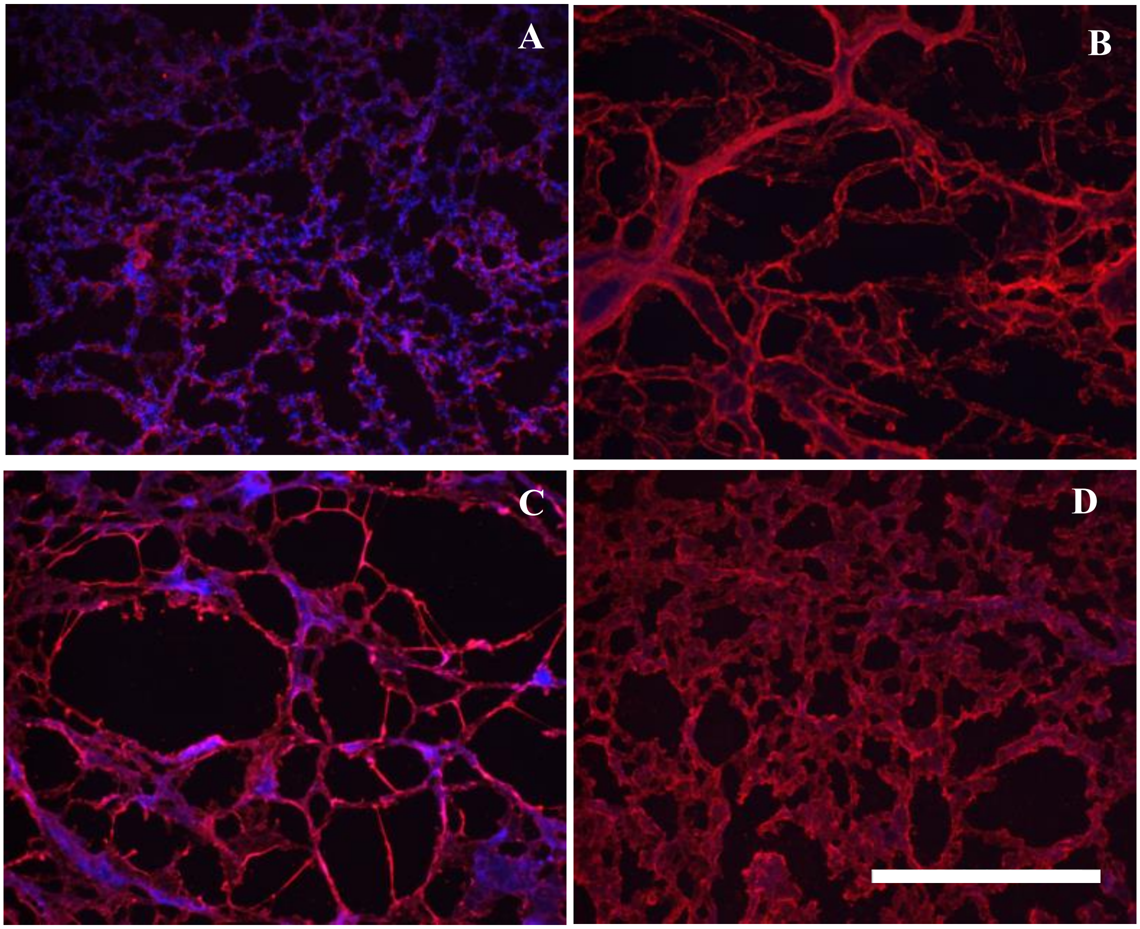

Figure 23. Fibronectin and DAPI immunostaining following different decellularization methods on lung tissue. Staining against fibronectin (red) demonstrates preservation of ECM biochemistry and organization when compared to fresh tissue (A). Higher organization was found in the groups using OA detergents; diffusion (B) and perfusion (D), compared to the PSDS method (C). Removal of nuclei through DAPI counterstain (blue) was seen following decellularization; however residual cationic staining is evident in perusion decellularization methods (C, D). Scale bar = 500

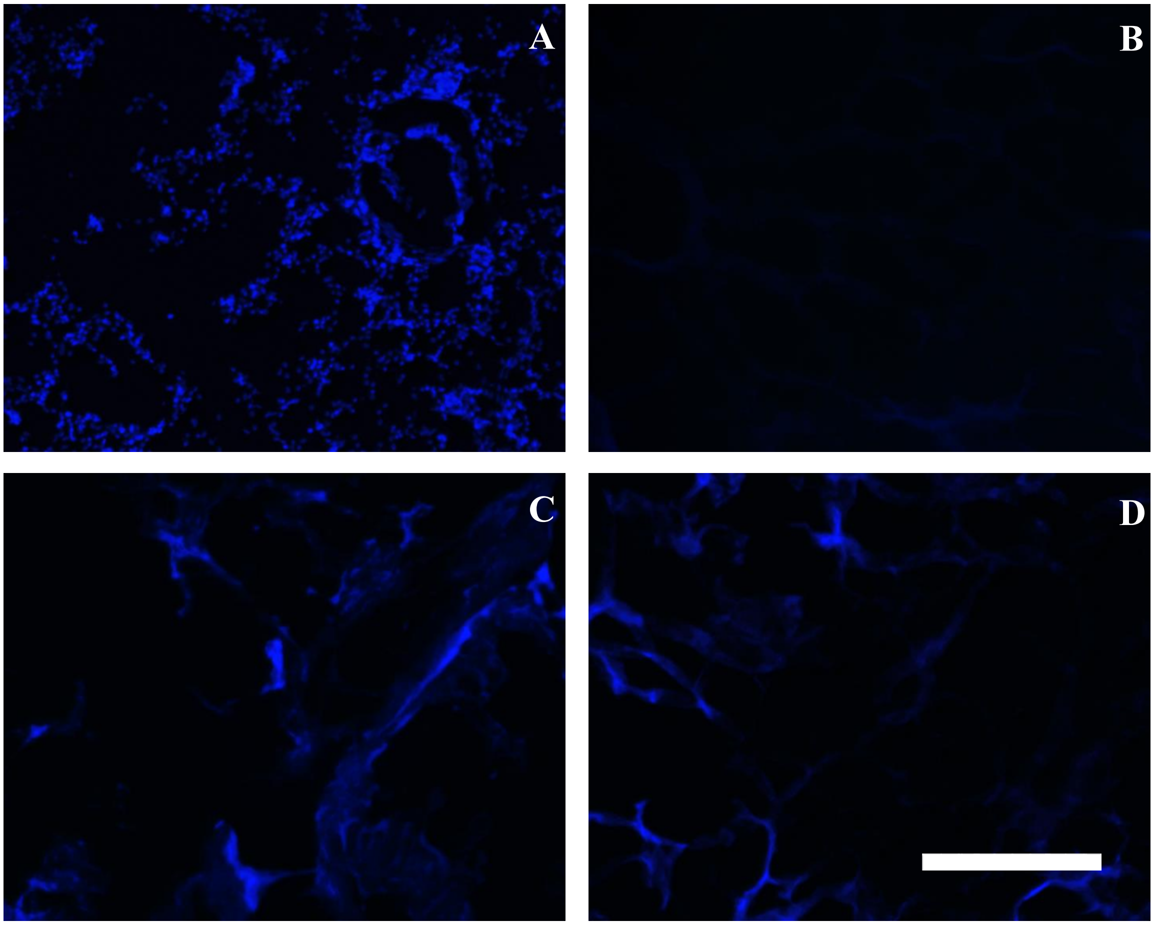

Figure 24. Staining for DAPI reveals removal of nuclei following decellularization of lung tissue using different methods (A, fresh lung; B, OA method; C, PSDS method; D, POA method). Residual anionic detergents from the perfusion based methods (C, D) stained positive in erratic fashion. Scale bar = 200 µm.

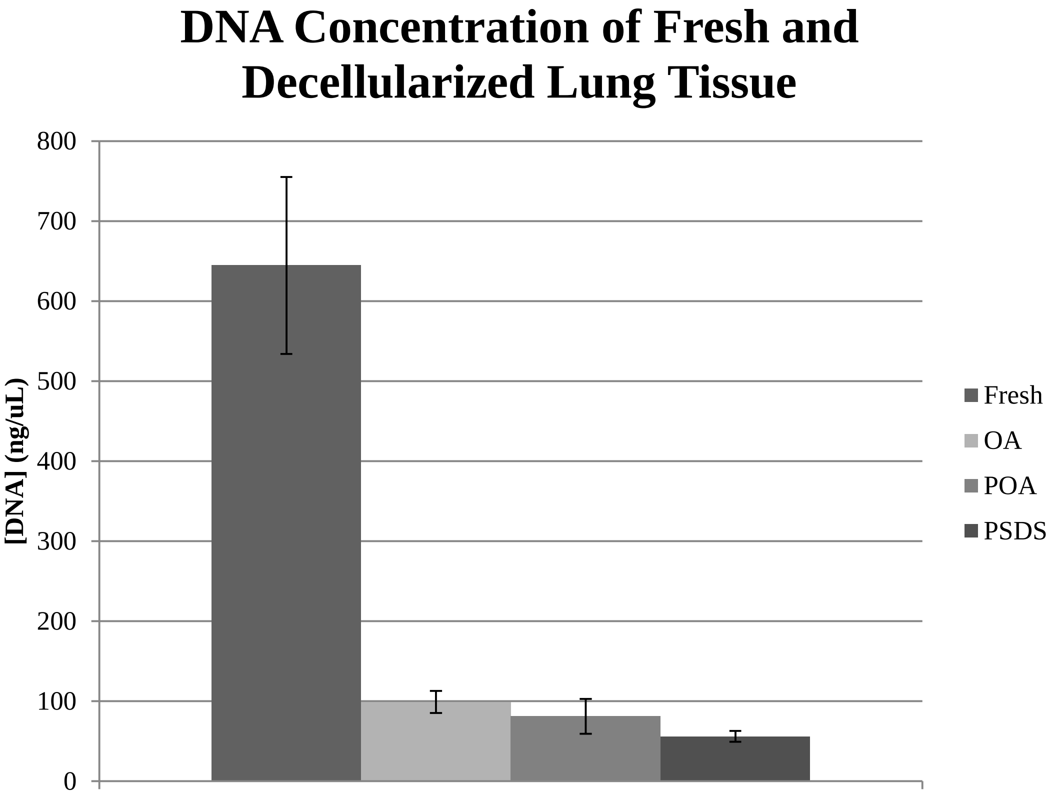

Figure 25. DNA concentration was determined using a NanoDrop spectrophotometer. Lung tissue decellularized using OA, POA, and PSDS methods demonstrated a significant decrease in concentration when compared to fresh tissue. The 91% decrease in DNA concentration following the PSDS method was also significant against 85% decrease from the OA method.

3.3.4 Vascular Corrosion Casting

Qualitative Evaluation of Casts

During VCC perfusion of each decellularization method, all of the Mercox resin was seen go into the pulmonary artery and exit through the pulmonary vein. The resulting casts all retained the shape and configuration of the lung, with a visible vascular axis intact. Macroscopically, the color of the casts appeared different. The fresh lung control was the most white in color, whereas perfusion decell methods had more color to them (**Figure 26**). Electron micrographs enabled capillary formations to be seen. The perfusion-decell groups failed to maintain vascular integrity at the capillary scale; whereas the OA decell group preserved capillary-like networks (**Figure 27**).

Quantitative VCC Analysis

Whereas differences were difficult to elucidate between the decell methods from histology, analysis of extravasations gave rise to distinct trends depending on tissue processing (**Table 1**). The fresh control had very few extravasations across all sizes. The OA method had a large number of extravasations less than 10 µm in diameter, but less extravasations of 10-20 µm, and significantly less 20-30 µm and over 30 µm extravasations when compared to the other decell methods. In addition, the total volume of resin that escaped OA tissue was substantially less than the perfusion decell methods (**Figure 28**). These results suggest that greater damage was done to the lumina of tissue processed through perfusion-based decellularization methods, than the OA method.

3.3.5 Subcutaneous Implantation of OA Scaffolds in vivo Present Normal Immunogenic Response

Following explantation, grafts from the allogeneic model, as well as the isogenic model shared typical inflammatory responses. After one week, the scaffolds were

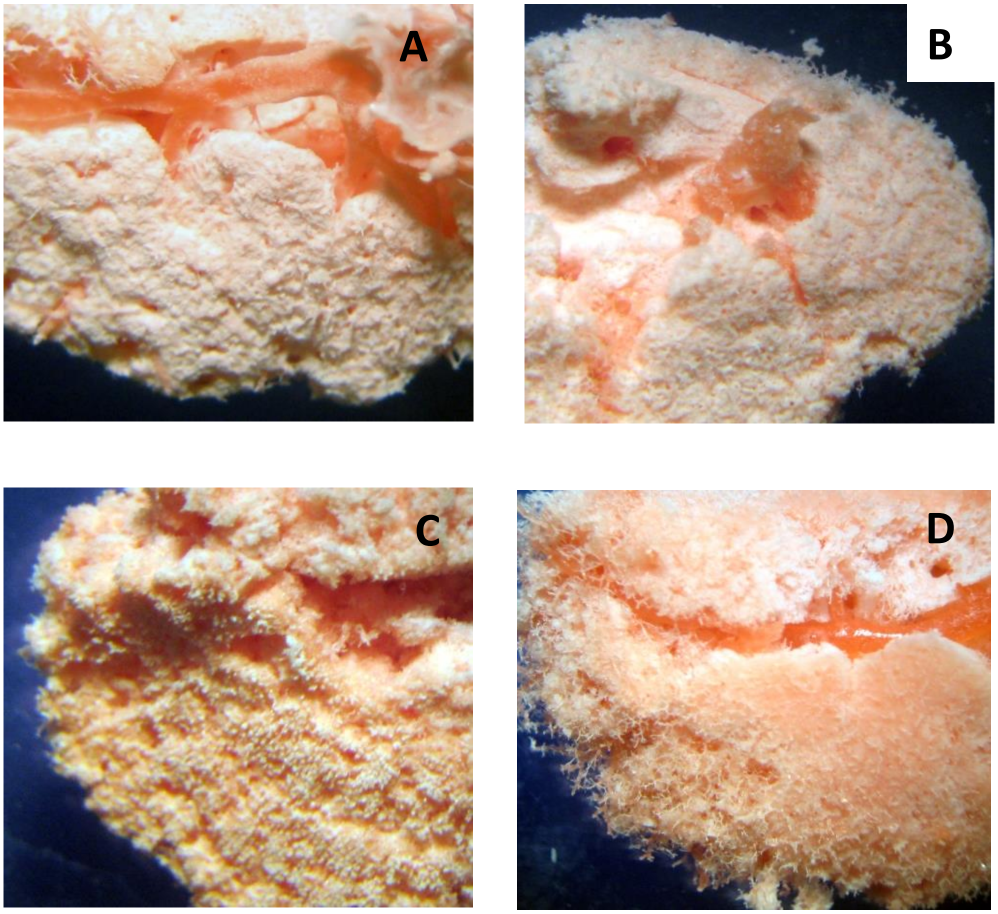

Figure 26. VCC of lungs following decellularization using different methods (A, fresh lung; B, OA method; C, PSDS method; D, POA method) reveals a defined geometry of mimicking the original tissue structure. The color of the casts appears to range from white to pink in order from A-D.

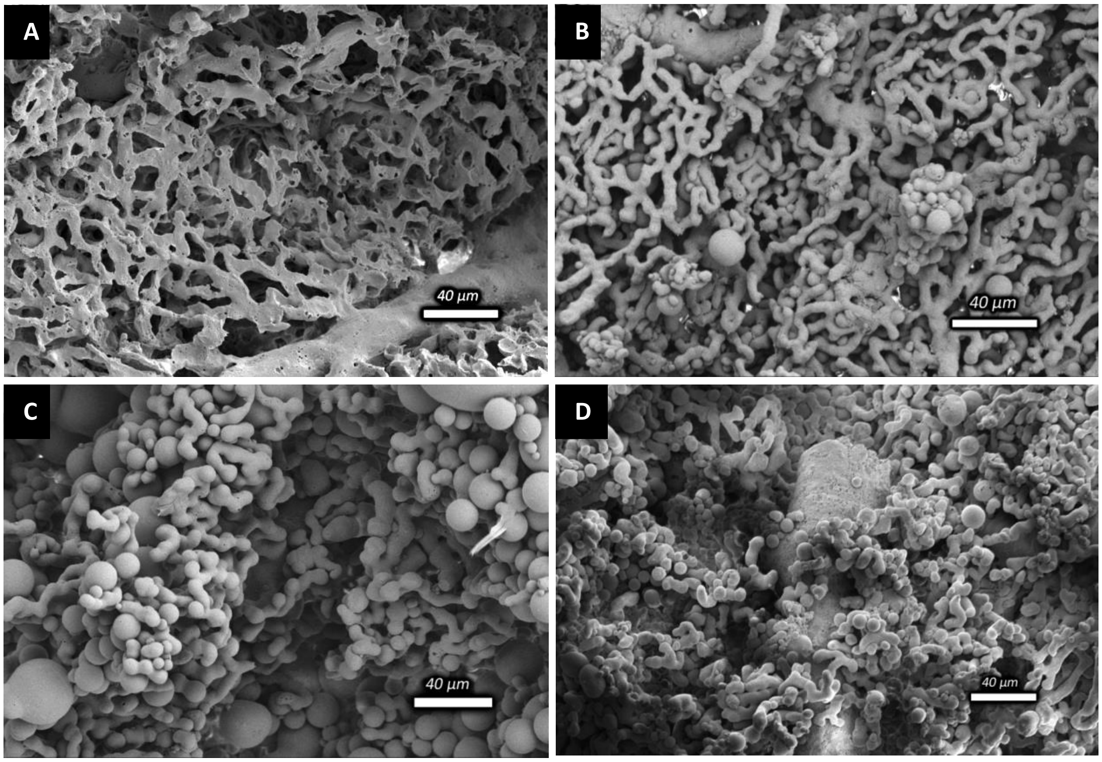

Figure 27. SEM images of VCC of lungs following decellularization using different methods (A, fresh lung; B, OA method; C, PSDS method; D, POA method). Fresh tissue displays a highly organized structure with intact vessels branching to capillary networks. OA method has some disorganized features to its capillary structure. The perfusion methods (PSDS and POA) are highly disorganized. Extravasations (asterisks) are most prevalent in the perfusion methods. The PSDS method appears to have the largest extravasations. Scale bars = 40µm.

Table 1. Extravasation Counts per mm^2 for Different Decellularization Methods

	Decellularization Method			
Extravasation Diameter	Fresh	OA	PSDS	POA
Less than 10	95.26 ± 113.8	4125.19 ± 4978.53*	418.76 ± 541.80†	4494.30 ± 2691.37*‡
10 to 20	24.01 ± 40.96	119.44 ± 11.70*	374.99 ± 474.49*	464.08 ± 425.11*†
20 to 30	3.37 ± 9.80	9.80 ± 19.5	71.78 ± 87.78*†	55.55 ± 65.25*†
Greater than 30	3.80 ± 5.88	2.56 ± 10.2	246.28 ± 148.39*†	18.15 ± 23.84*†‡

Asterisk, dagger, and double dagger denote significance ($p<0.05$) versus fresh, OA, and PSDS groups respectively

Table 1. Extravasation counts following vascular corrosion casting of fresh and decellularized lung tissue plus or minus one standard deviation. A greater number of extravasations less than 10 microns in diameter was seen in OA decellularized lung casts compared to fresh and PSDS casts; however, larger extravasation counts for OA casts were not significantly different from fresh tissue, whereas PSDS and POA casts displayed significance versus fresh tissue.

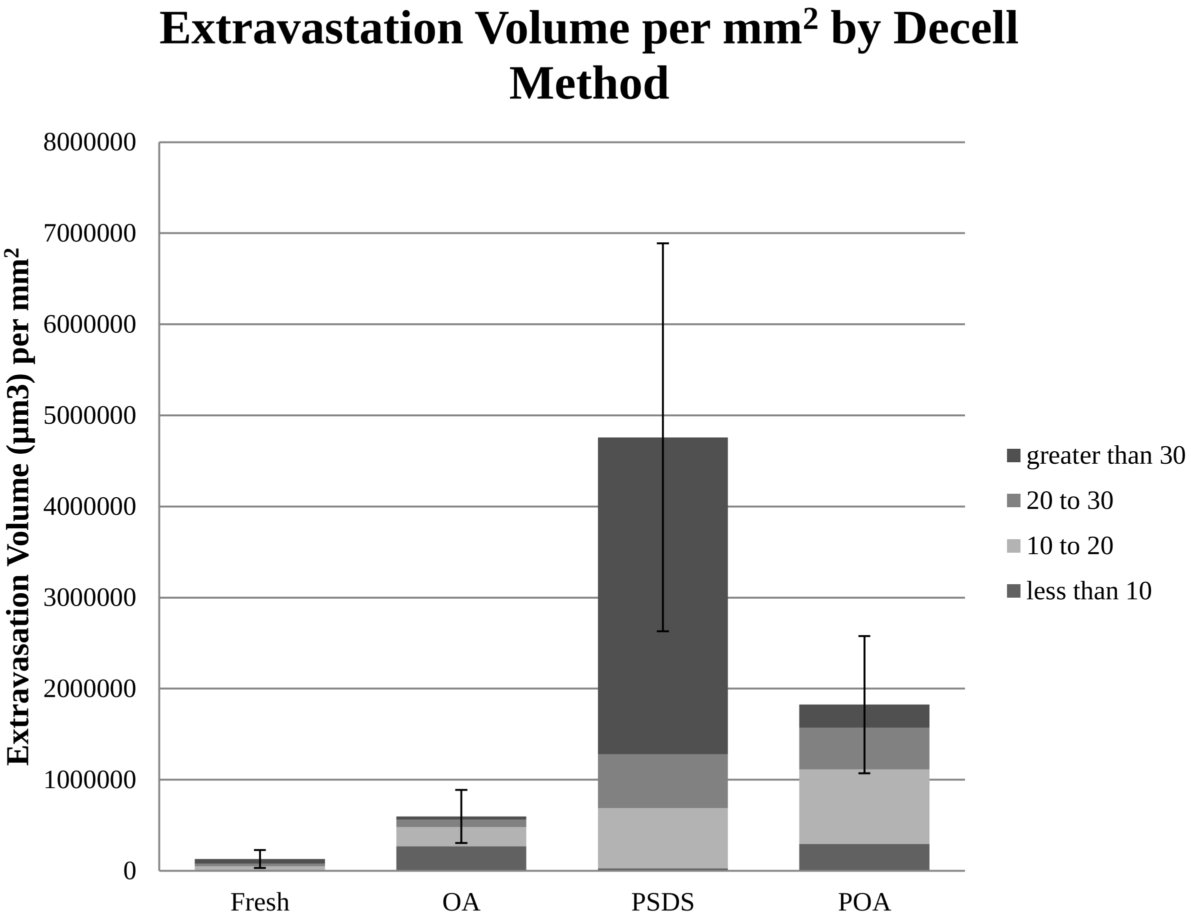

Figure 28. Total extravasation volume was calculated per mm^2 by cubic micron for each decellularization method investigated. The amount of vascular damage correlated with larger extravasations was apparent when assessing the volume of resin that escaped the vascular space of the tissue. Although damage was found following each decellularization method, the diffusion based OA method was by far the most effective at preventing the escape of resin from the remaining vascular network of ECM. Error bars represent 2SEM.

already encapsulated in fibrous tissue. At four weeks in all animals, the capsule surrounding the scaffold was thicker, and the scaffold was fully cellularized, remodeled to a flat circular morphology, and substantially smaller in size (**Figure 29**).

General histological analysis through H&E revealed similar fibrous encapsulation between isograft and allograft tissues at one and four week implantation duration. Immunohistochemistry targeting macrophages revealed additional similarities amongst groups in each implantation duration (**Figures 30, 31**). Specifically, in one-week implantation groups, macrophage counts per total cell count were 0.059 and 0.068 for isografts and allografts respectively and not statistically significant ($p>0.35$) (**Figure 32**). Total cell counts within the isograft scaffolds were more than double the allograft scaffold (23,503 and 11,125). Following one week, macrophages were most commonly found surrounding the tissue, whereas few macrophages were present within the scaffolds. Although some cellular penetration was seen following one week, most cells were found within a few hundred microns from the exterior of the scaffold; however, mass cellular infiltration was observed surrounding the bronchus of the scaffold—with few macrophage cells present (**Figure 30**).

Following implantation for four weeks, scaffolds revealed full cellular infiltration. Isografts and allografts maintained fewer immunogenic cells per nuclei compared to one-week explants (0.021 and 0.009 respectively, and were statistically significant $p<0.00001$ against one-week explants) (**Figure 32**). The total number of cells counted in each group was nearly equivalent as well at 74,279 for allografts and 74,456 for isografts—a significant increase over the one-week explants.

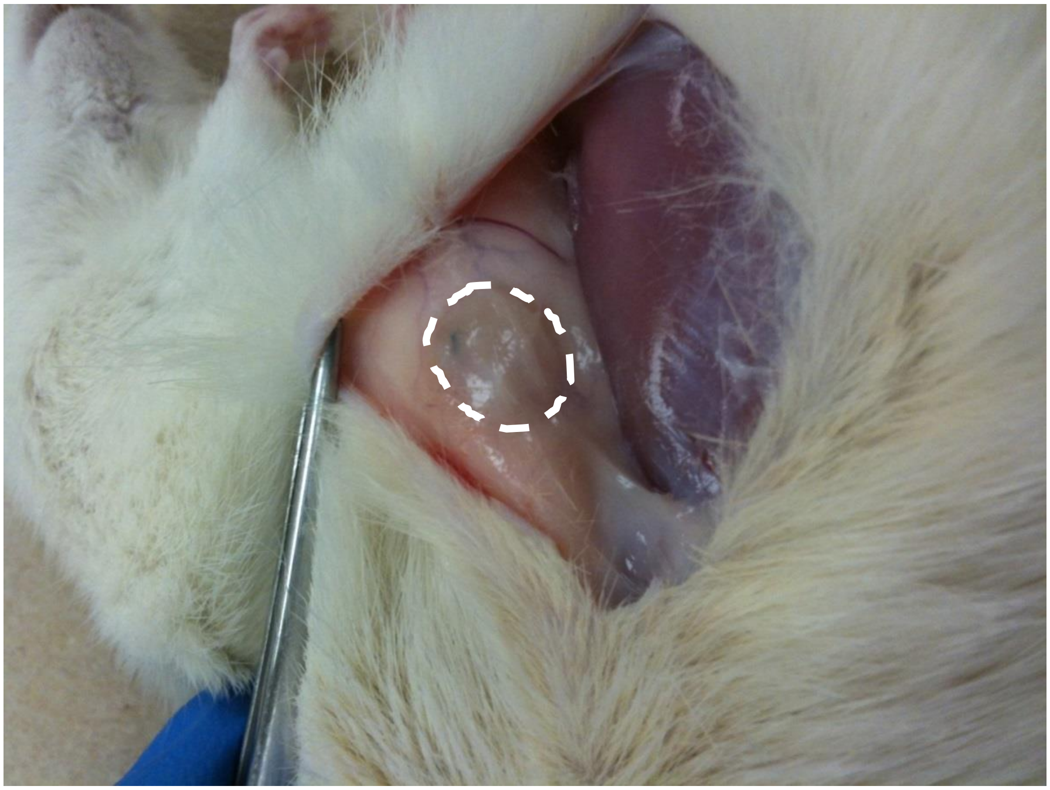

Figure 29. Right flank of a rat opened following four weeks *in vivo* to reveal the subcutaneous OA implant. Extensive remodeling of the tissue was visualized. The formerly white decellularized scaffold is now tan, demonstrating cellular infiltration. Fibrous encapsulation was seen in all implants, both allogeneic and isogenic.

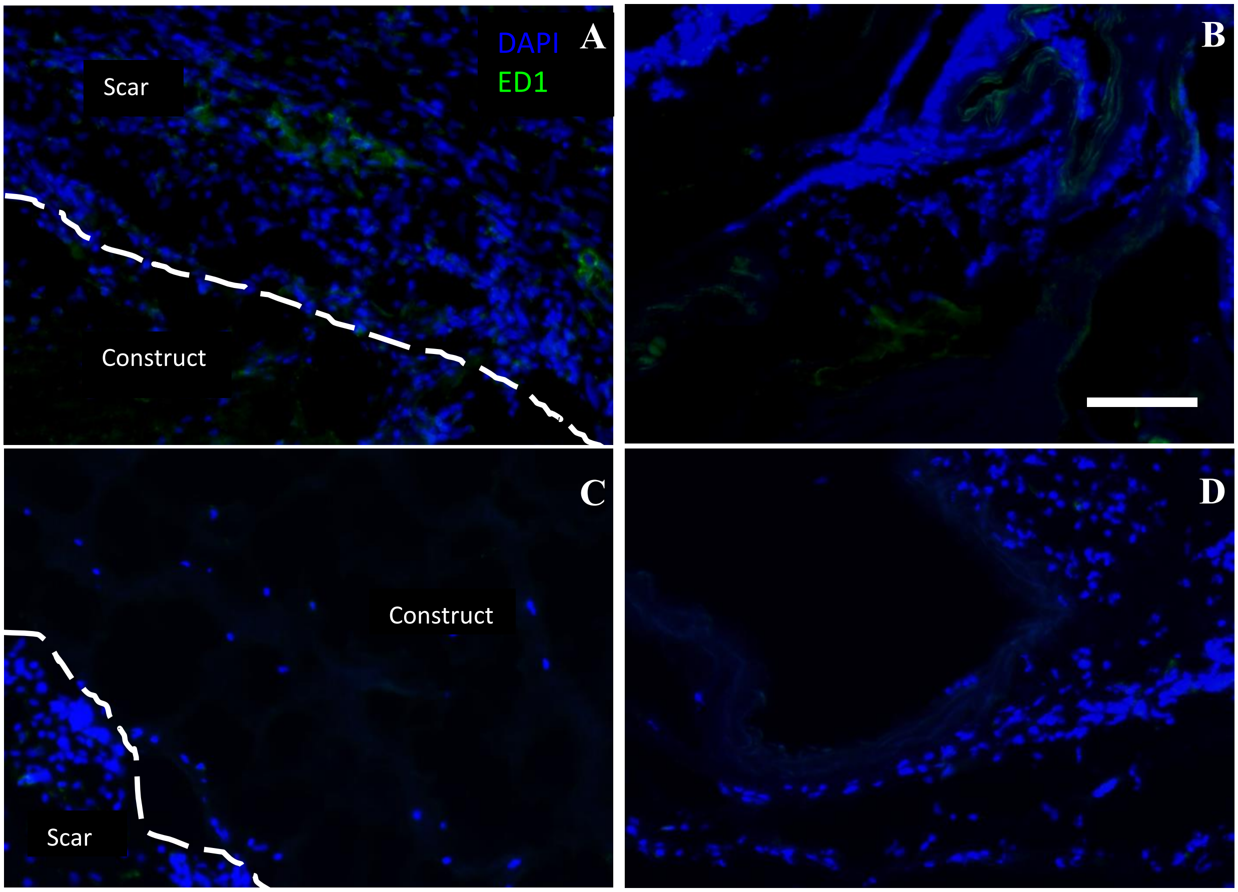

Figure 30. Isogenic (A,B) and allogeneic (C,D) OA explants harvested one week following subcutaneous implantation demonstrated similarities in cellular infiltration. Staining for the macrophage marker ED1 depicted increased macrophage counts in the fibrous scar surrounding the OA scaffold when compared to inside the scaffold in isografts (A) and allografts (C). Increased cellular infiltration into the OA scaffolds was seen near the bronchus in both isograft (B) and allograft (D). This cellular infiltration failed to stain positively for ED1. Scale bar = 100µm.

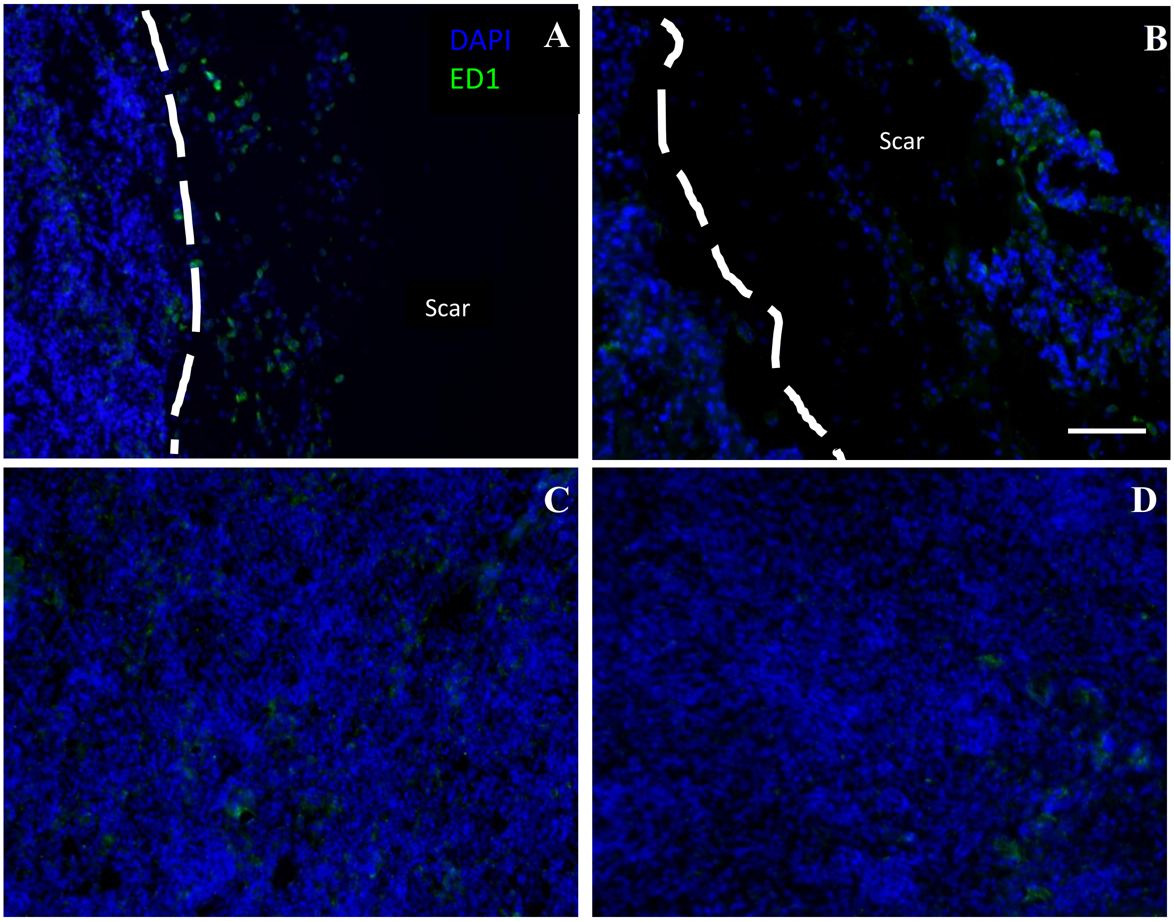

Figure 31. Isogeneic (A, C) and allogeneic (B, D) OA explants harvested one week following subcutaneous implantation demonstrated similarities in cellular infiltration. Staining for the macrophage marker ED1 depicted increased macrophage counts per total cell count in the fibrous scar surrounding the OA scaffold (A,B) when compared to inside the scaffold (C,D). Cells were able to completely recellularize the center of the scaffolds (C, D), compared to explants harvested after one week following implantation, where cells were primarily found near the exterior of the scaffold. Scale bar = 100µm.

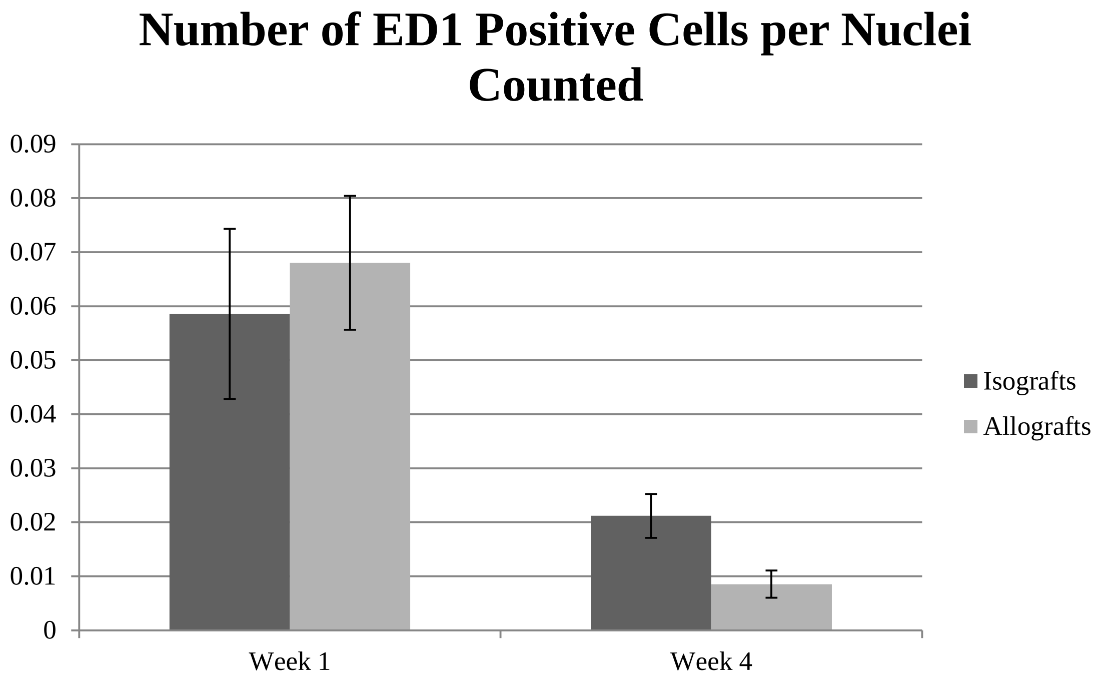

Figure 32. The number of ED1 positive cells was counted following immunohistochemistry and image processing of isograft and allograft OA scaffolds subcutaneously implanted for one and four weeks. This number was then divided by the total number of cells counted then averaged. Significance occurred between the one and four week groups as well as between isografts and allografts following four weeks implantation. Error bars represent 2SEM.

3.4 CONCLUSIONS

The OA process was successfully adapted to decellularize lung tissue leaving behind capillary-like structures while effectively eliminating cellular material. This was demonstrated through general histology, immunohistochemistry, HPLC analysis, DNA quantification, and VCC methods. Immunogenicity of this scaffold was then tested revealing the inert nature of the decellularized tissue following subcutaneous implantation for one and four weeks.

Chapter 4: Re-endothelialization of a Decellularized Vascular Scaffold

4.1 INTRODUCTION

The previous chapter described the development and characterization of a process to effectively decellularize lung tissue. The advantages of the OA process were verified through comparisons with alternative decellularization methods, and enabled further investigations to be performed using this substrate. This chapter delves into the capacity for the OA scaffold to support re-endothelialization, as well as the implications re-endothelialization have on the performance of the OA scaffold as a vascular engineering tool. Subsequent experiments involving re-endothelialization were evaluated using US/PA imaging and histology, and the effects that re-endothelialization have on recovering vascular patency were evaluated by using VCCs and comparing clotting proclivity following the perfusion of whole-blood into OA scaffolds with and without cells.

4.2 RESEARCH DESIGN AND METHODS

4.2.1 Culture and Incubation of Endothelial Cells with Gold Nanotracers

HDMECs were obtained from Promega (Heidlberg, Germany); HUVECs were obtained from Lonza (Basel, Switzerland). These cells were plated with an initial seeding density of 10,000 cells/cm^2 for HDMECs and 5,000 cells/cm^2 for HUVECs, then expanded and used from passage three to seven in all studies. Gold nanotracers were added to the cells for observance with photoacoustic absorbance as described previously [115, 116]. Briefly, 10^{12} nanoparticles/ml of media were used to incubate cells, with 200 μl/cm^2 of nanoparticle medium added to the cell culture for 24 hours.

These nanotracer loaded cells were then expanded to confluency (typically 5 days following an initial seeding density of 10,000 cells/cm^2 for HDMECs and 5,000 cells/cm^{2}for HUVECs) and imaged using phase contrast, darkfield, and brightfield imaging to observe the uptake of nanoparticles, as well as general morphological behavior.

Cytotoxicity was analyzed using a standard MTS assay (CellTiter 96® Aqueous One Solution CellProliferation Assay, Promega, Madison, WI). HDMECs and HUVECs were seeded in gold nanotracers for 24 hours as described previously in a standard 24-well plate at 10,000 and 5,000 cells/cm^2 respectively. Each cell type was allowed to grow for 24 and 72 hours following the addition of nanotracers before subsequent analysis. The MTS dye was then added to the cells at 20% the normal media volume for four hours at 37^{o}C. Next, 240 µl MTS solution was taken in triplicate from each well and read in a 96-well plate at 490 nm wavelength. For each cell type a standard curve for cells was created to ensure assay accuracy.

4.2.2 Ultrasound-Guided Photoacoustic Imaging of Re-endothelialized Scaffolds

Scaffolds re-endothelialized with cells containing gold nanotracers were imaged using ultrasound-guided photoacoustic imaging. Following re-endothelialization, scaffolds were incubated in 4% paraformaldehyde for four hours then imaged. Ultrasound and photoacoustic signals were captured using a 20 MHz array transducer with Vevo 2100 ultrasound micro imaging system (VisualSonics, Inc.). A tunable OPO laser beam (Premiscan, GWU, Inc.) pumped by a pulsed Nd:YAG laser (Quanta-Ray, Spectra Physics, Inc.) was delivered through an optical fiber bundle (Ceramoptec, Inc.). The fiber bundle was combined with the ultrasound transducer and aligned such that the transmitted light would focus at the focal point of the transducer using a positional stage (Zaber, Inc.). The trigger signal from the laser system was synchronized with the computer or the Vevo 2100 imaging system to capture the photoacoustic signal when the pulsed laser irradiated. Once the photoacoustic transient and ultrasound pulse-echo signal was captured, the off-line image processing was performed with the acquired imaging data. The magnitudes of the ultrasound and photoacoustic signals were calculated by taking the absolute values of analytic signals obtained using the Hilbert transform. The photoacoustic signal magnitude was then compensated for wavelength dependent laser fluence. The compensated ultrasound and photoacoustic signals were interpolated to 2D images. The combined ultrasound and photoacoustic images were created by overlaying photoacoustic intensities higher than a user-defined threshold on the grayscale ultrasound images. The scaffolds were imaged at 700 nm wavelength with a fluence around 10-13 mJ/cm^2. As a control, scaffolds devoid of cells were imaged for PA signal as well. As a further confirmation of cellularity following US/PA imaging, scaffolds were sectioned with a cryostat to observe the phenotype of the cells present in the scaffolds using immunohistochemistry.

4.2.3 Re-endothelialization Optimization in Optimized Acellular Scaffolds

To evaluate whether aggregation would occur in capillaries, gold nanoparticles ($3x10^{12}$ nanoparticles in 3 ml of media) were injected into the vascular axis of the OA scaffold, and then imaged with US/PA imaging to visualize distribution.

Next, endothelial cells incubated with gold nanotracers were perfused into the vascular axis of the OA vascular scaffolds using perfusion methods described previously for VCC. Concentration and number of perfusions were altered to ensure cells were present throughout the entirety of the scaffolds (concentrations ranged from 10^6 cells/ml to $2x10^7$ cells/ml, and either delivered in a single bolus injection, or divided into three injections of three ml over two hours. Cells with nanotracers were injected into the vascular axis at two ml/min using a syringe pump (KD Scientific 200). Each Using

US/PA imaging to observe cellular distribution, it was determined that three injections of 3 ml over a 3 hour time span with a concentration of 10^6 cells per ml provided optimal cell distribution in the scaffold. Cells were then allowed to adhere to the substrate overnight before the addition of pulsatile flow.

4.2.4 Pulsatile Cell Culture

Unless otherwise stated, all components of the system were autoclaved to maintain sterility, and all setup was performed in a vertical or horizontal flow hood. To connect the tissue to the pump we used the same modified 24-gauge cannula that was used in VCC that was e-beam sterilized prior to use. The cannula was connected to prefilled #16 tubing platinum cured silicone tubing (Masterflex, Germany) with a male fitting. This tubing was fed through an autoclavable 100x15 mm petri dish (Thermo Scientific, Waltham, MA) through a hole drilled smaller than the outer diameter of the tubing. This tubing was then run through a rubber plug that allowed for eventual access to the interior of the cell incubator while keeping the pump head free of humidity. The other end of the tubing was fed through another hole in the petri dish that allowed for circulation of media.

To sterilize the lung prior to loading cells, the isolated left lung was exposed to 17 kGy of radiation using an electron beam (Nutek Corp., Hayward, CA). Cells were subjected to pulsatile flow using a peristaltic pump (iPumps, Type A) while following a gradual shear flow culturing protocol [35]. Briefly, pulsatile shear stress of 3.2 dyn/cm^2 for 24 hours, followed by 8.7 dyn/cm^2 for 12 hours, and finally 19.6 dyn/cm^2 for 24 hours was delivered to cells. The flow rates necessary to deliver these shear stresses were calculated using the Hagen-Poiseuille equation (**eq. 1**), assuming a tube diameter at the macrovascular range equating to 0.5 mm.

$$\tau = \frac{4\eta f}{\pi R^3} \quad \textbf{(eq. 1)}$$

After the 60 hour shear conditioning was concluded, scaffolds were cleared of media by perfusing PBS through the system in a series of washes. To aid in the transfer of solutions by completely clearing the tubing while preventing air bubbles from entering the tissue, the cannula was detached from the system with sterile forceps, then reattached. The lung was then directly fixed with 4^{o}C 4% paraformaldehyde for 5 minutes, then post-fixed for four hours. The cannula and suture was then removed in samples for US/PA imaging and histology, or left in for samples that would be immediately cast with resin.

Histology was performed to assess the scaffold following re-endothelialization. Immunostaining against VE-cadherin (Abcam, 33168), CD-31, and DAPI following standard immunohistochemical protocols was performed. The secondary antibodies were goat anti-rabbit AlexaFluor 488, and goat anti-mouse AlexaFluor 568 (1:400).

4.2.5 Vascular Casting of Re-endothelialized Scaffolds

Following re-endothelialization, scaffolds were perfused with Mercox II CL-2R for VCC inspection using methods described previously. These VCC were used to obtain both a general sense of the preservation of vascular networks, and also images for qVCC as described previously with acellular scaffolds alone. VCC results from re-endothelialized scaffolds would be compared to the data obtained from acellular scaffolds alone to elucidate what extent re-endothelialization had on recovering the vascular patency within the acellular scaffold.

4.2.6 Whole-Blood Perfusion Assay

To understand how vascular patency might pertain to real-life applications, a whole-blood perfusion and clearing procedure was developed. 50 ml of PBS was perfused into re-endothelialized, OA vascular scaffolds alone, and fresh lung prior to blood perfusion. Whole-blood from humans (Sanguine Biosciences, Valencia, CA) was strained through a 70 micron nylon-mesh sterile cell strainer (Fisher Scientific) before being perfused into the various scaffolds. The PBS and blood were perfused into our scaffolds via a peristaltic pump at 5.8 ml/min. Following blood perfusion, the scaffolds were perfused with 100 ml PBS. Photographs were taken before and after perfusion with blood and PBS. Next, the scaffolds were fixed with 4% paraformaldehyde for four hours and sectioned for histology and immunohistochemistry targeting platelet formations, using CD-31 and DAPI.

4.3 RESULTS

Testing the ability of the OA scaffold to support re-endothelialization began by selecting two endothelial lineages, a system to support perfusion-culture, and a technique to monitor the cellular distribution. Both cell lineages were able to be successfully injected into scaffolds and subsequently subjected to perfusion-culture using a peristaltic pump and a chamber to house the scaffold. Using ultrasound-guided photoacoustic (US/PA) imaging allowed us to visualize cellular distribution throughout the entirety of the scaffold. To use US/PA imaging, cells need to be incubated with gold nanotracers. We first had to ensure that the cells tolerated incubation, verified through an MTS assay. The functionality of the vascular network of the OA scaffold with and without cells was compared using vascular corrosion casting (VCC), and revealed an improved structure both qualitatively and quantitatively. The improved vascular structure in re-endothelialized scaffolds also resulted in improved vascular clearing following perfusion with whole-blood.

4.3.1 Endothelial Cells Cultured with Gold Nanotracers Exhibit Normal Morphology and no Cytotoxicity

HDMECs and HUVECs first incubated with gold nanotracers, then cultured to confluency demonstrated normal morphology (**Figures 33, 34**). HDMECs and HUVECs demonstrated a cobblestone-like morphology indicative of healthy endothelial cells when confluent. Also, cytotoxicity results indicated through the use of an MTS assay reveal that the incubation of nanoparticles failed to decrease cellular viability (**Figures 35, 36**). Although there was a significant difference between HUVECs monitored 24 hours following the addition of nanoparticles ($p<0.01$), the difference in observed MTS fluorescence intensity at 490 nm for cells cultured with nanoparticles was only 15% less than intensity observed in cells cultured without nanoparticles. Furthermore, although statistically insignificant ($p>0.35$) at 72 hours following the addition of nanoparticles, the fluorescence intensity for cells cultured with nanoparticles was 9% greater than cells cultured without nanoparticles.

Each standard for the MTS assay demonstrated a linear relationship between cells and fluorescence intensity.

4.3.2 Optimized Injection Parameters Enable Uniform Cellular Distribution

The blank OA decellularized scaffold was a devoid of PA signal when applying US/PA imaging (**Figure 37**). The initial bolus injection of nanoparticles into the vascular axis of the OA scaffold revealed PA detection only present near the pulmonary artery of the tissue (**Figure 38**). Although, media was able to perfuse fully through the vein of the tissue, nanotracers were aggregating resulting in plasmonic resonance and PA detection.

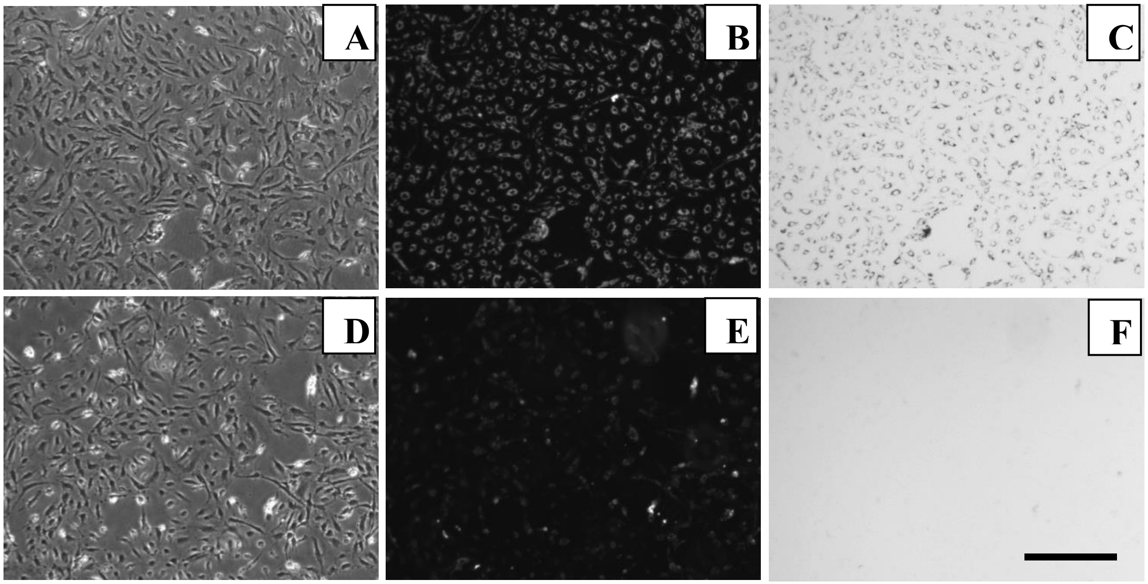

Figure 33. Effects of nanoparticle incubation on HDMEC morphology. HDMECs incubated with gold nanoparticles overnight, then allowed proliferate near confluency (A-C) displayed similar morphology as HDMECs plated without nanoparticles (D-F). Phase-contrast imaging reveals cobblestone morphology in nanoparticle and control groups (A, D) and a departure from spindle-like morphology. Dark-field and bright-field imaging demonstrate the presence of nanoparticles (B, C) compared to control (E, F). Scale bar = 50µm.

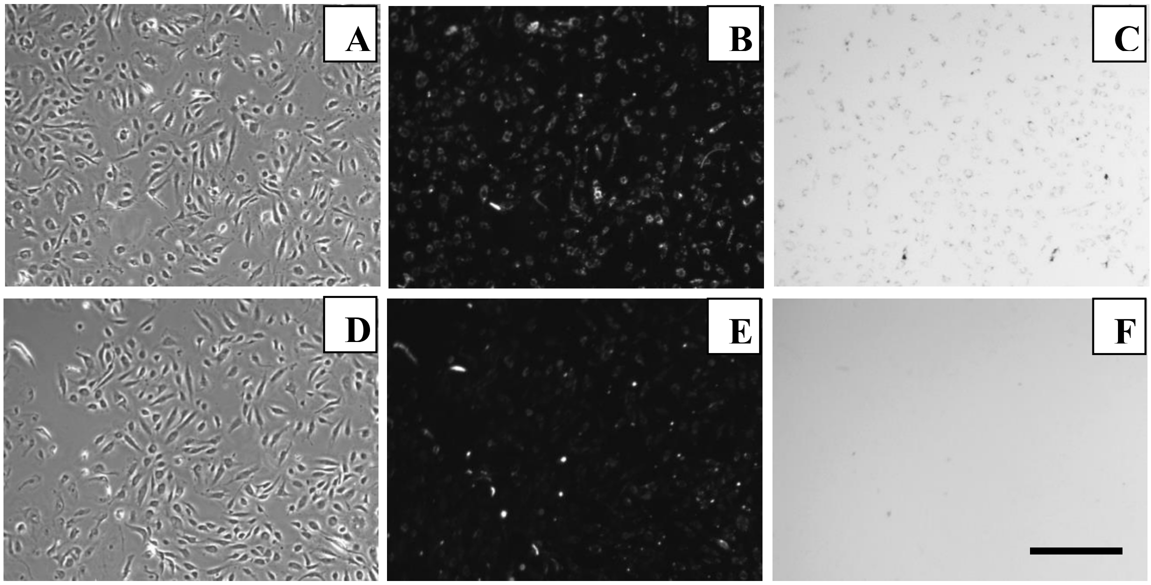

Figure 34. Effects of nanoparticle incubation on HUVEC morphology .HUVECs incubated with gold nanoparticles overnight, then allowed proliferate near confluency (A-C) displayed similar morphology as HUVECs plated without nanoparticles (D-F). Phase-contrast imaging reveals cobblestone morphology in nanoparticle and control groups (A, D) and a departure from spindle-like morphology. Dark-field and bright-field imaging demonstrate the presence of nanoparticles (B, C) compared to control (E, F). Scale bar = 50 µm.

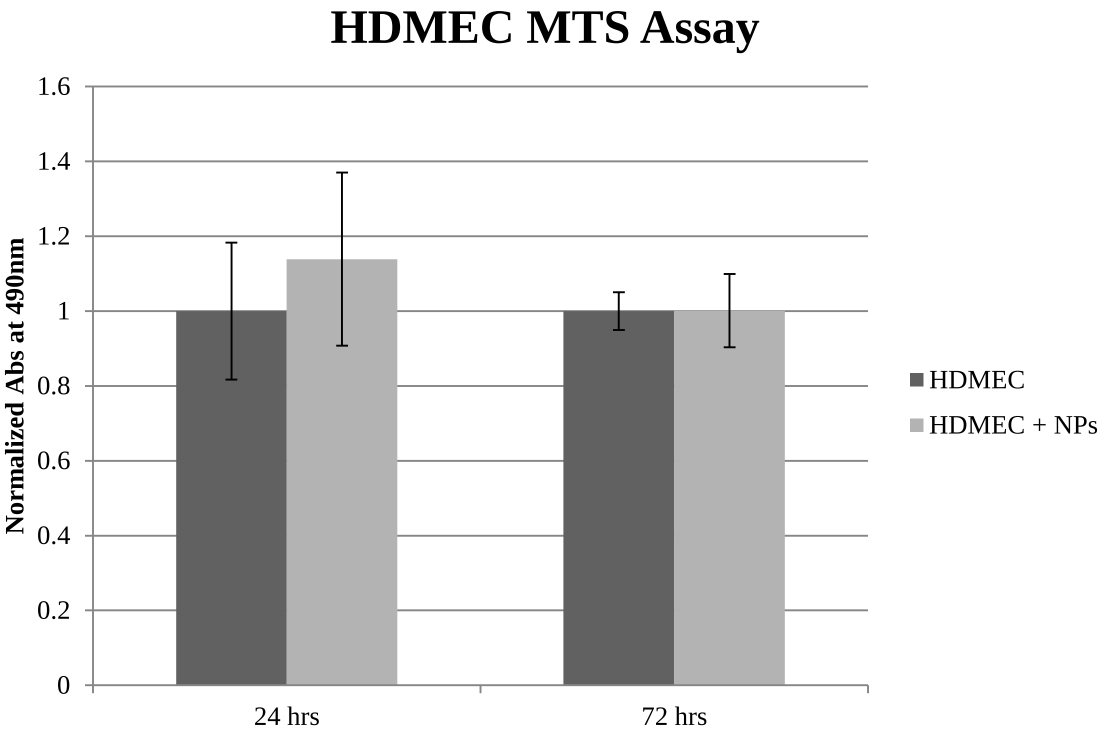

Figure 35. Following incubation with gold nanotracers for 24 hours, HDMECs were maintained for 24 and 72 hours then incubated with MTS for four hours. The culture media and MTS dye were then imaged on a 96-well plate in triplicate at 490 nm. HDMECs incubated with did not exhibit abnormal metabolic activity when compared to HDMECs without nanotracers.

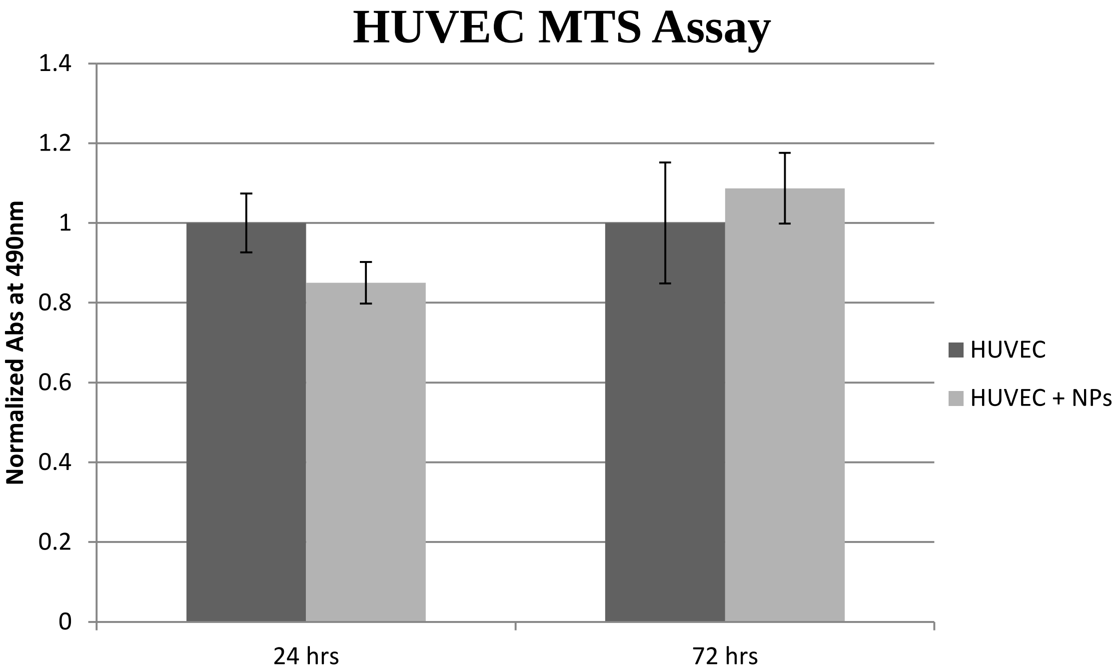

Figure 36. Following incubation with gold nanotracers for 24 hours, HUVECs were maintained for 24 and 72 hours then incubated with MTS for four hours. The culture media and MTS dye were then imaged on a 96-well plate in triplicate at 490 nm. Although the metabolic activity of HUVECs cultured with nanotracers was significantly less than HUVECs cultured without nanotracers at 24 hours, this difference was not present in cells maintained for 72 hours after the addition of nanotracers.

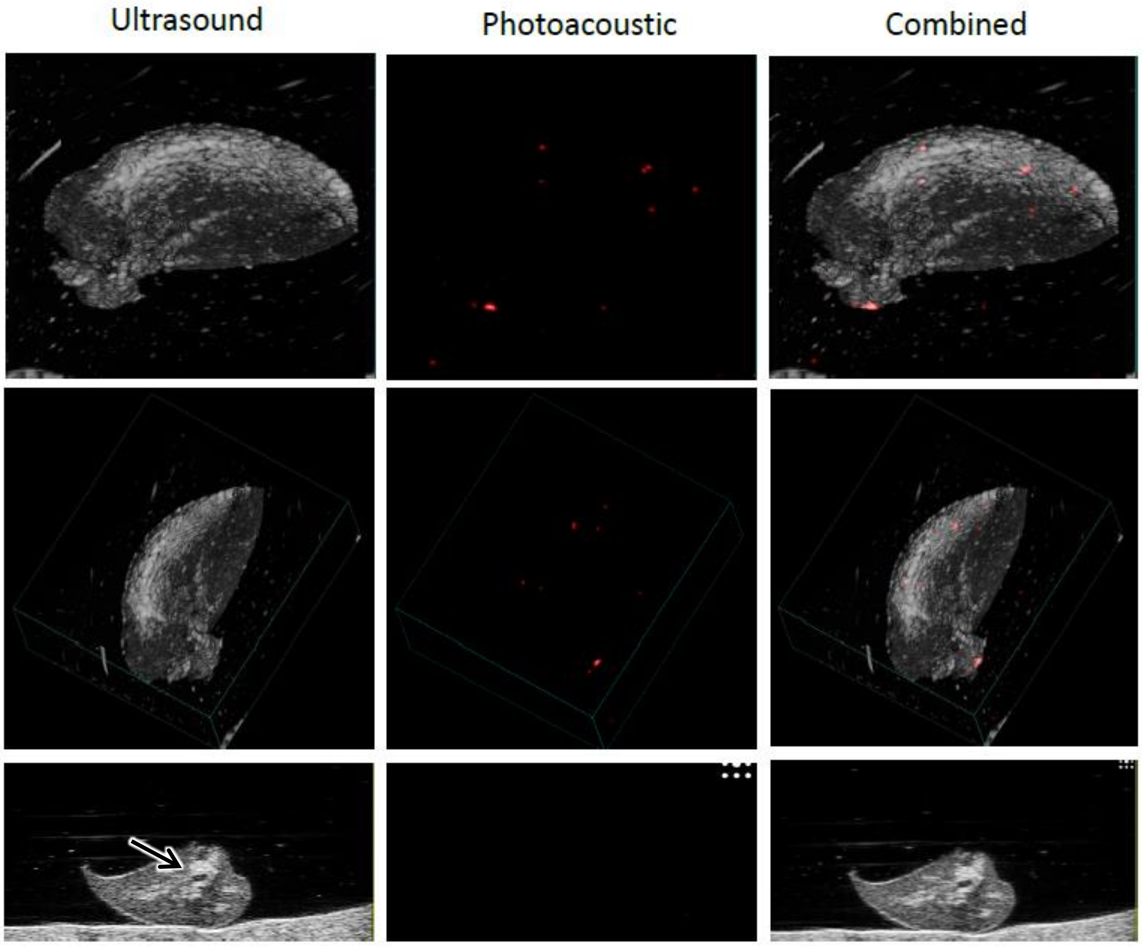

Figure 37. Ultrasound-guided photoacoustic imaging of an optimized acellular scaffold. Imaging reveals absence of photoacoustic signal at 750nm. A void in the scaffold representing the bronchus can be seen in cross-sections of the ultrasound images (arrow).

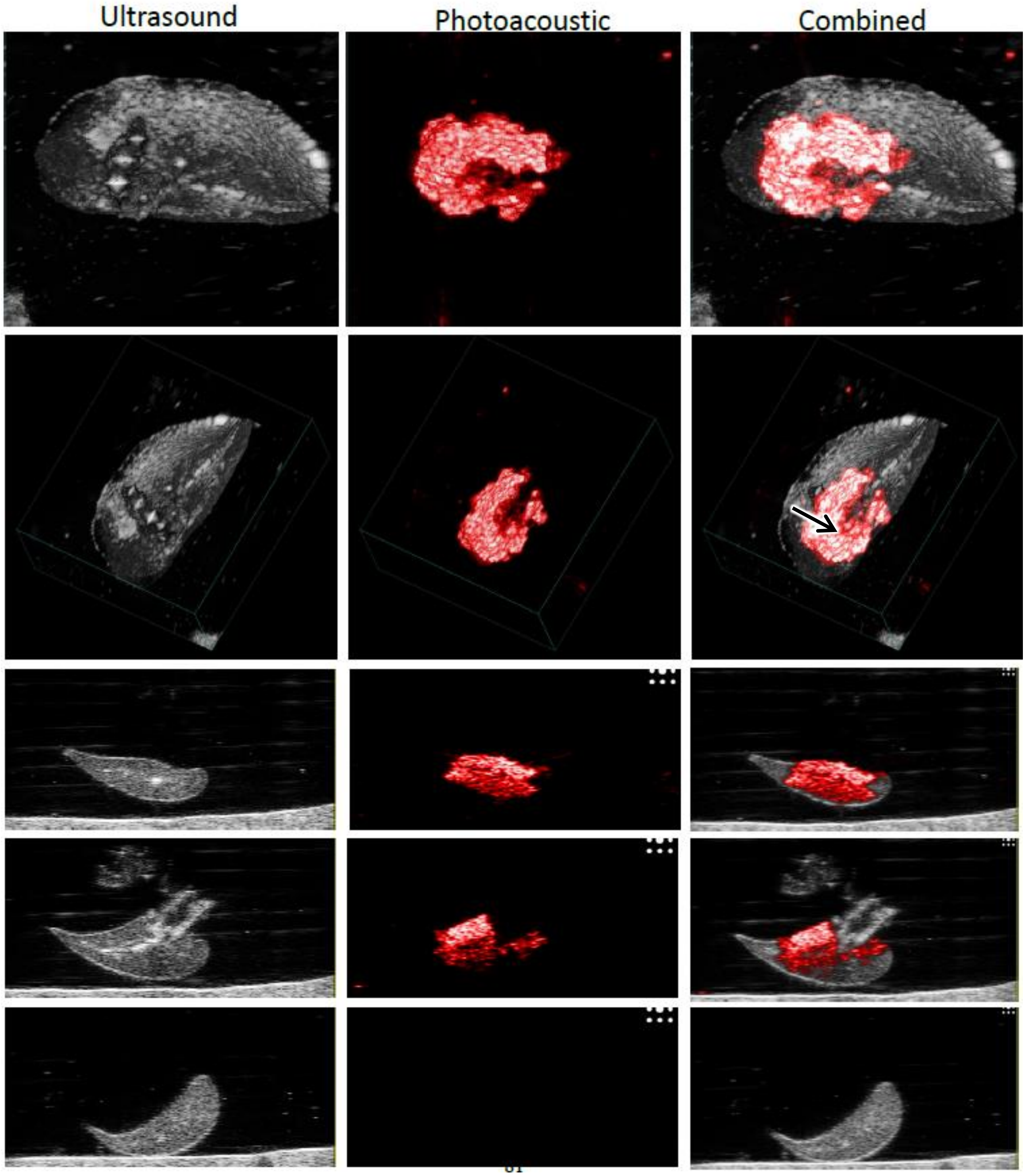

Figure 38. Nanoparticle injection into an OA scaffold. A single bolus injection of nanoparticles into the pulmonary artery of an OA scaffold demonstrates localization towards the entry point (arrow). Nanoparticles likely clogged the smaller vessels, allowing for plasmonic coupling, red-shifting, and resulting photoacoustic signal detection at 750nm to occur. Media was rinsed out then tissue was fixed prior to US/PA imaging.

The results of various injection parameters demonstrated the importance that concentration would have on aggregation and thus establishing a uniform cellular distribution. Using a single bolus injection of $3\text{x}10^6$cells in 9 ml media resulted in aggregation and clustered distribution of cells (**Figure 39**). When the injections were spread out to a series of three injections of 10^6 cells/ one ml media, the distribution was improved for HUVECs and HDMECs (**Figures 40, 41)**. This optimized re-endothelialization plan was then adopted for subsequent studies.

Following re-endothelialization and staining for VE-cadherin, CD-31 and DAPI several observations were made (**Figure 42**). Although uniform distribution could be visualized through US/PA imaging, and cells were found throughout the scaffold sections, at the cellular level the entirety of the scaffold was not cellularized. Brightfield imaging revealed the presence of cells in the locations of nuclei visualized fluorescently (**Figure 42**); however, although a minority, there were also nanoparticles present which were not associated with nuclei, but were positive for CD-31 and VE-cadherin markers. The majority of the media that exited the pulmonary vein of the scaffold after perfusion contained intact cells, not damaged cells. Positive CD-31 imaging was observed and generally associated with positive staining for VE-cadherin. These results point at the need to refine the cell concentration for re-endothelialization.

4.3.3 Re-endothelialization of OA Scaffolds with HDMECs Improves Vascular Patency down to the Capillary Scale

Following re-endothelialization and perfusion culture using both HUVECs and HDMECs, photoacoustic signal revealed that cells were well-distributed in the scaffolds (**Figures 43-45)**. Creating VCCs of these re-endothelialized scaffolds enabled differences in patency to be observed down to the capillary scale (**Figure 46**). Cellular

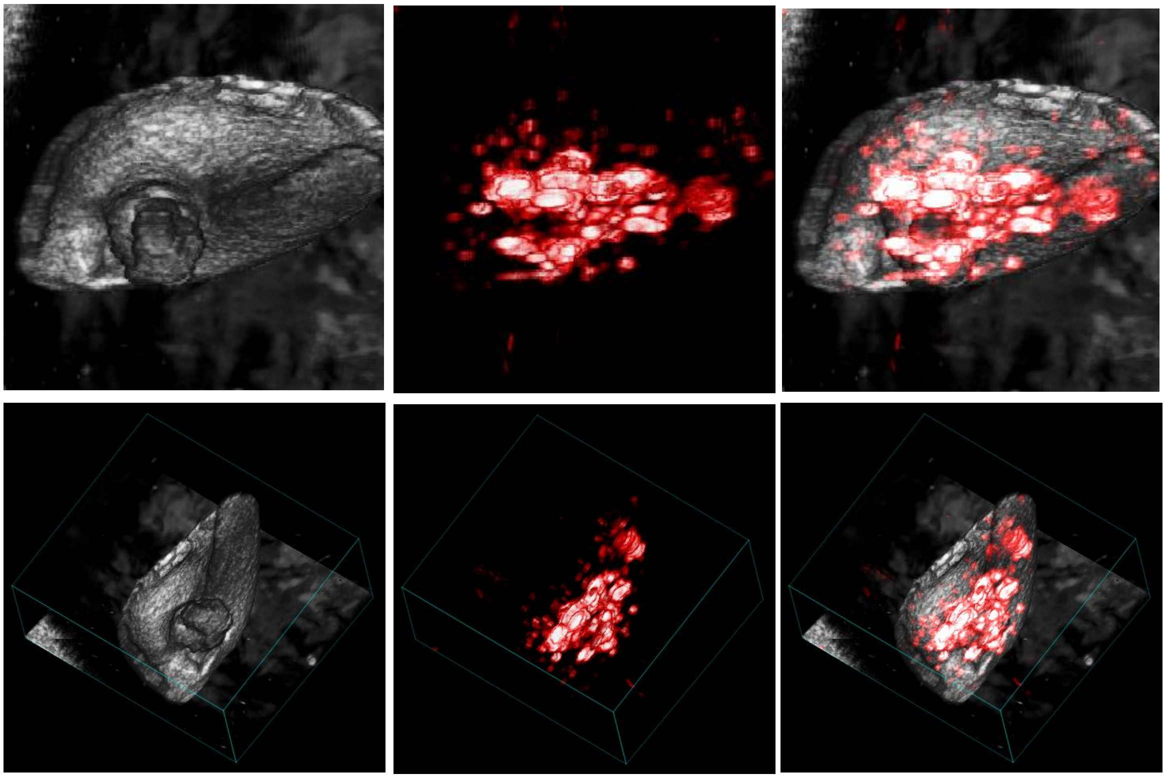

Figure 39. Single bolus injection of HUVECs into an OA scaffold. A single bolus injection of 2.5×10^5 HUVECs with gold nanoparticles in 4.5ml media results in poor distribution of cells in an OA scaffold. Media was rinsed out then tissue was fixed prior to US/PA imaging at 750nm.

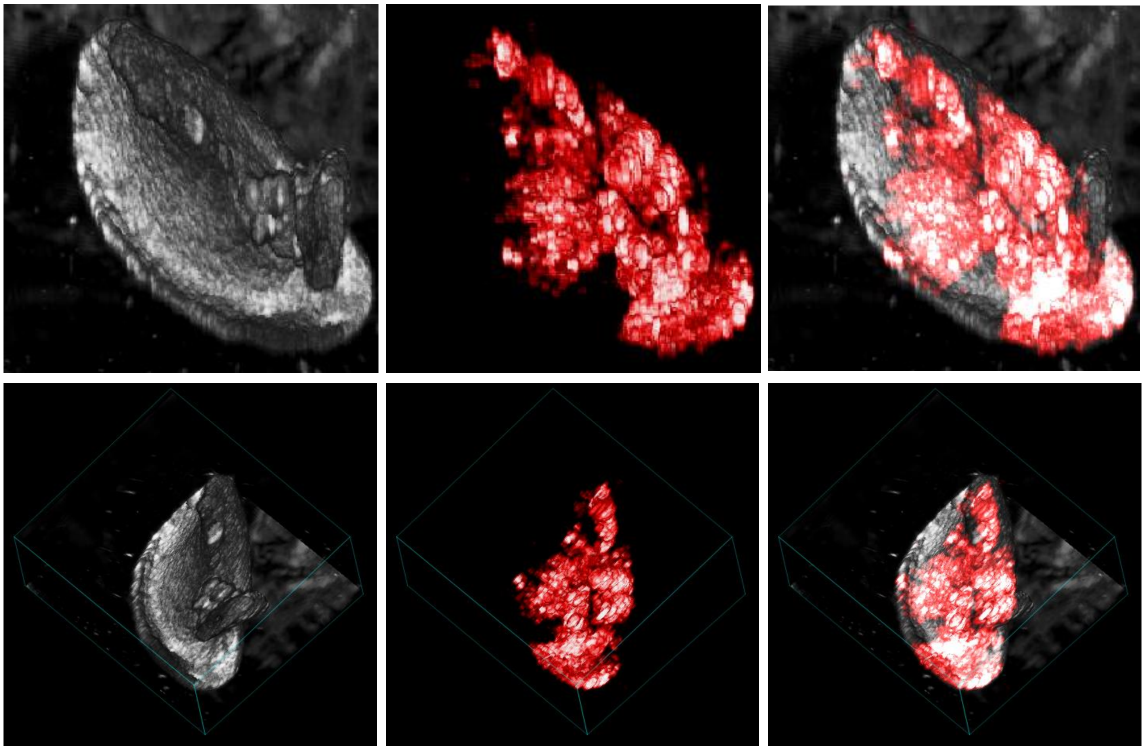

Figure 40. Multiple injections of HUVECs into an OA scaffold. Three injections of 8.3×10^4 HUVECs with gold nanoparticles in 1.5ml media over two hours results in better distribution of cells within an OA scaffold. Media was rinsed out then tissue was fixed prior to US/PA imaging at 750nm.

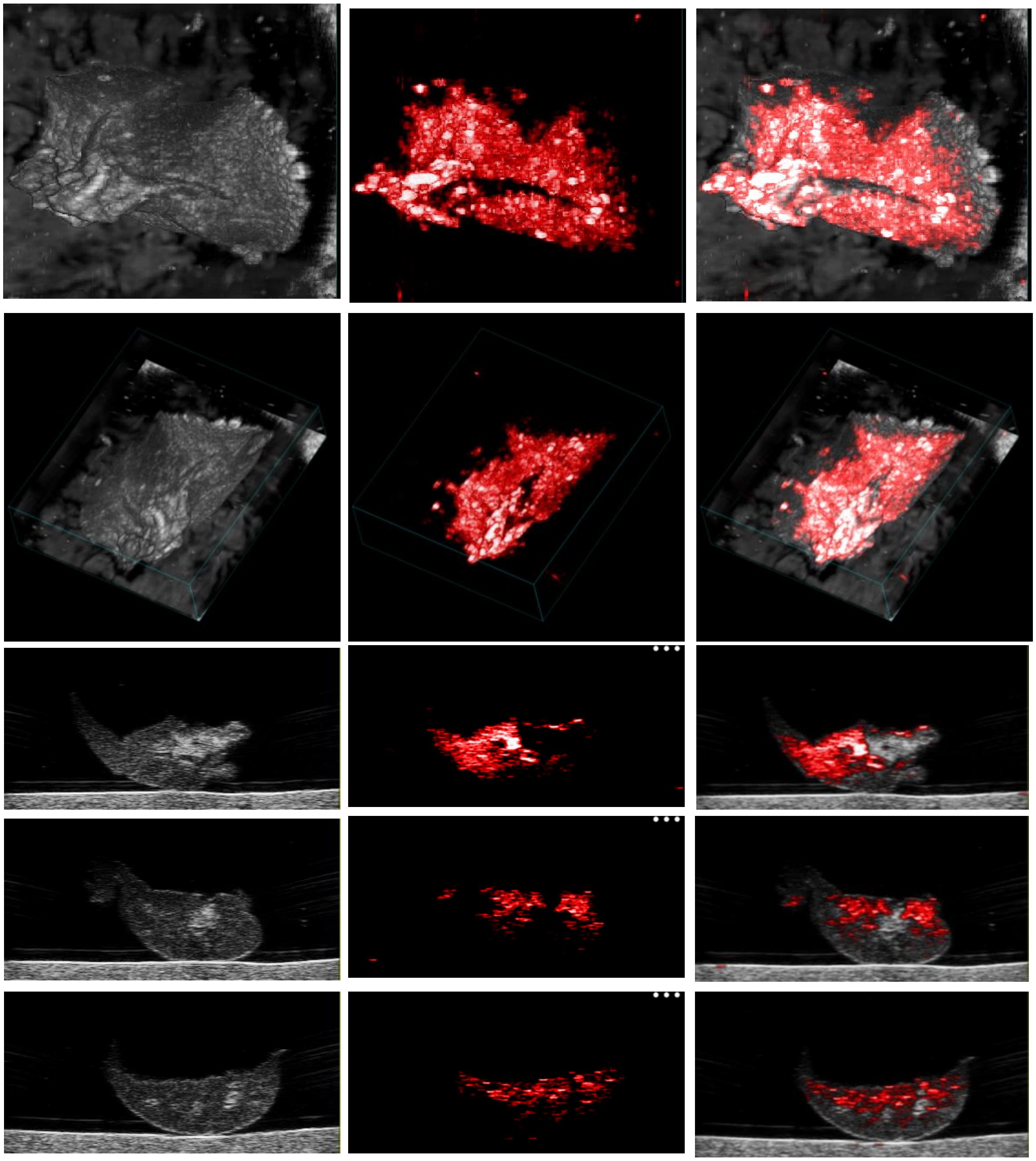

Figure 41. Multiple injections of HDMECs into an OA scaffold. Three injections of $1.6x10^5$ HDMECs with gold nanoparticles in 3.3ml media over two hours results in distribution of cells within the entirety of an OA scaffold. Media was rinsed out then tissue was fixed prior to US/PA imaging at 750nm.

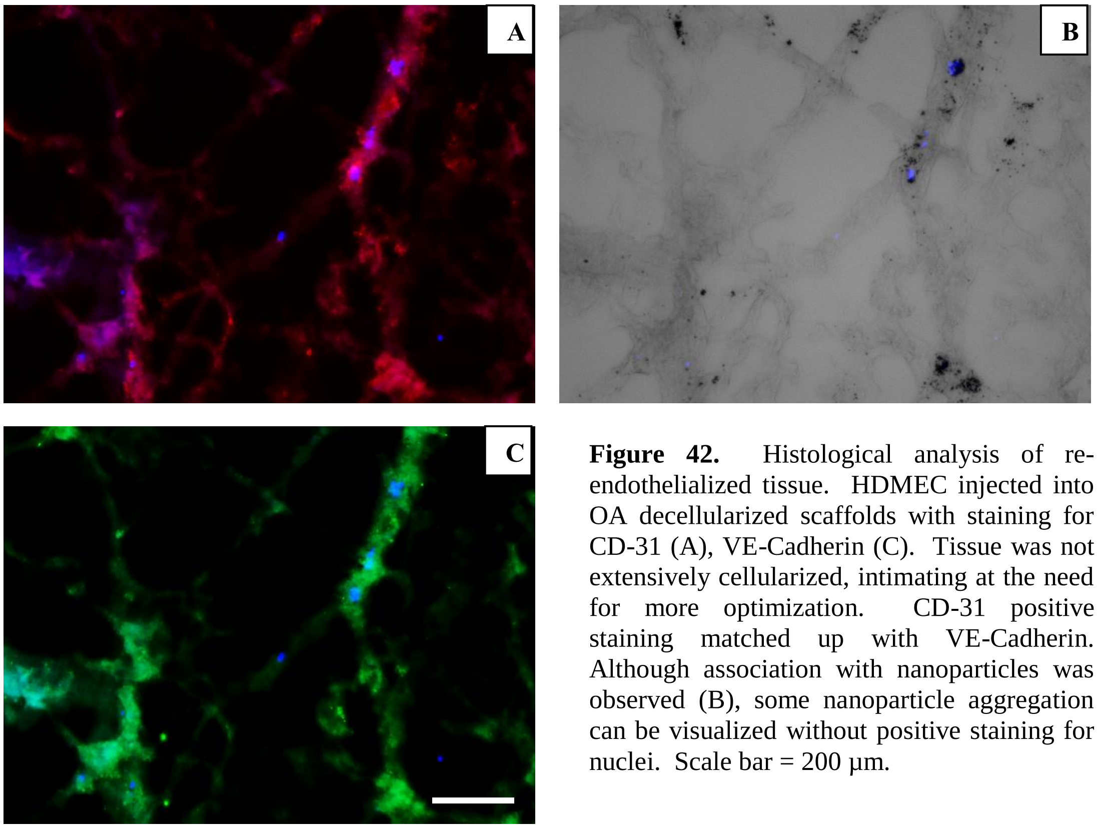

Figure 42. Histological analysis of re-endothelialized tissue. HDMEC injected into OA decellularized scaffolds with staining for CD-31 (A), VE-Cadherin (C). Tissue was not extensively cellularized, intimating at the need for more optimization. CD-31 positive staining matched up with VE-Cadherin. Although association with nanoparticles was observed (B), some nanoparticle aggregation can be visualized without positive staining for nuclei. Scale bar = 200 µm.

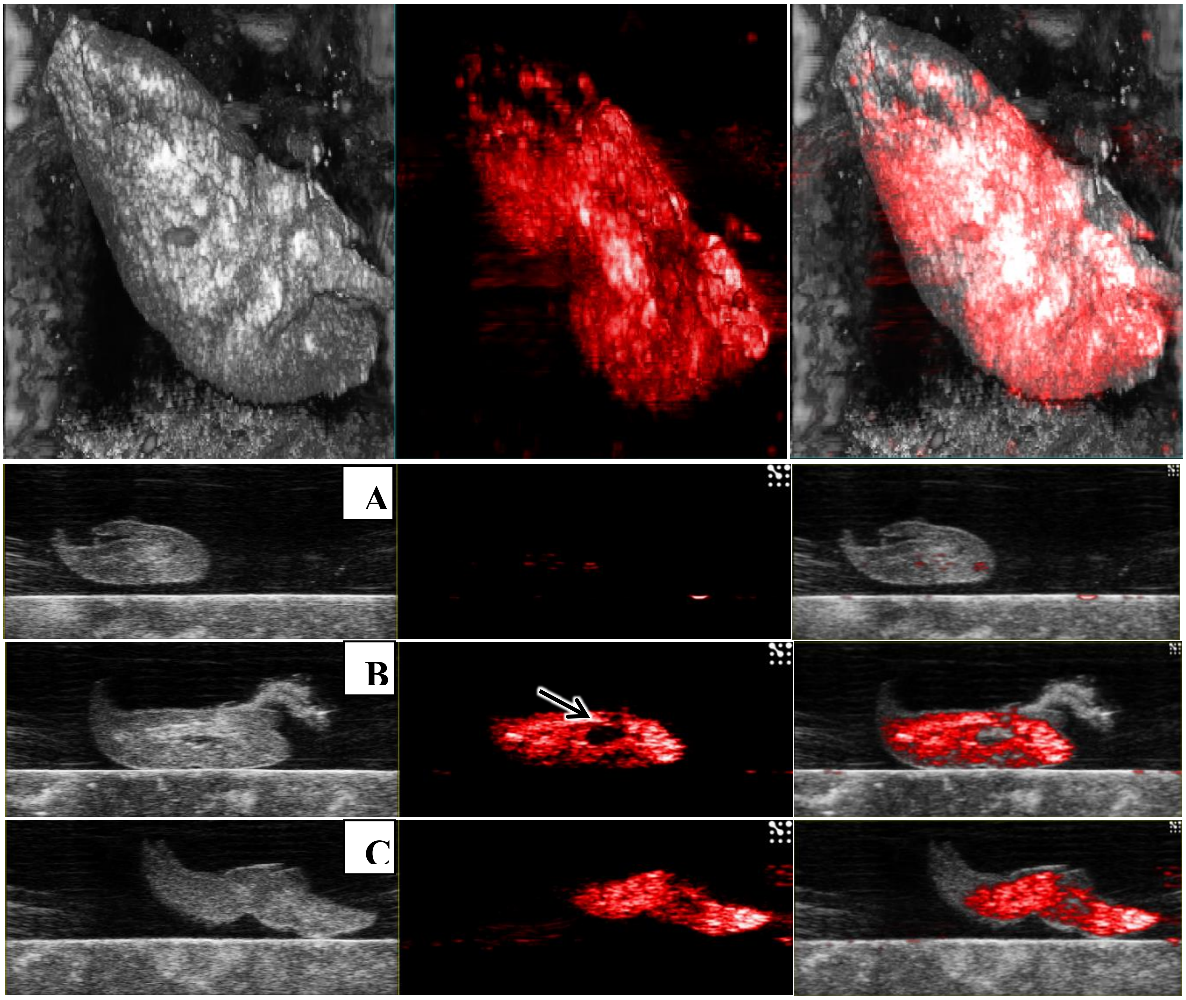

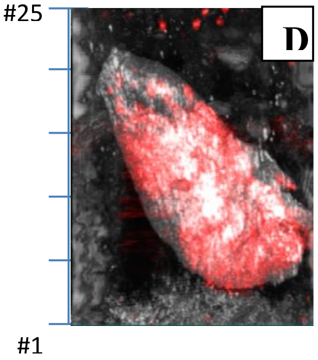

Figure 43. Perfusion culture following HUVEC re-endothelialization. Three injections of $3.3\text{x}10^5$ HUVECs with gold nanoparticles in 3.3 ml media over two hours were delivered to an OA scaffold. Cells were allowed to adhere overnight before gradually increasing perfusion flow was administered (3.2 dyn/cm^2 for 24 hours, 8.7 dyn/ cm^2 for 121 hours, 19.6 dyn/ cm^2 for 24 hours). Photoacoustic signal from cells at 750nm indicates the retention of cells distributed within the entirety of an OA scaffold at the conclusion of the culture. Cross sections from rows A , B, and C, depict slice #180, #130, and #70 respectively (D). Note the void represented by the bronchus is still present following culturing, demonstrating cellular infiltration did not occur (B, arrow). Media was rinsed out then tissue was fixed prior to US/PA imaging at 750nm.

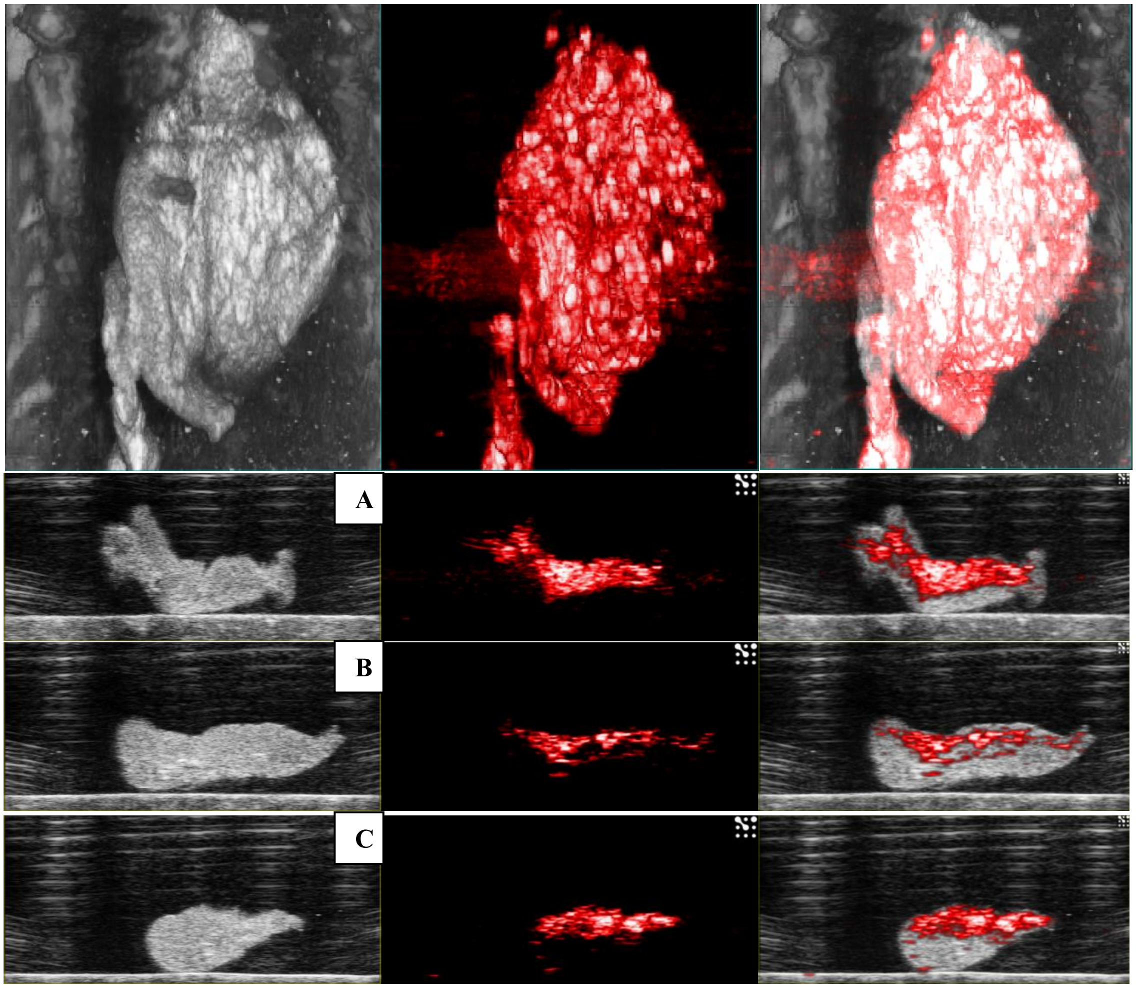

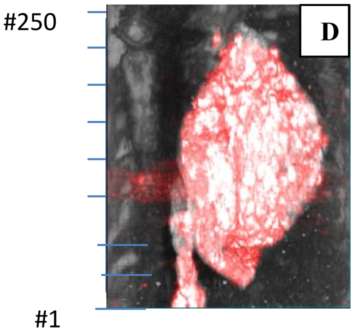

Figure 44. Perfusion culture following HDMEC re-endothelialization. Three injections of 3.3×10^5 HDMECs with gold nanoparticles in 3.3 ml media over two hours were delivered to an OA scaffold. Cells were allowed to adhere overnight before gradually increasing perfusion flow was administered (3.2 dyn/cm^2 for 24 hours, 8.7 dyn/ cm^2 for 121 hours, 19.6 dyn/ cm^2 for 24 hours). Media was rinsed out then tissue was fixed prior to US/PA imaging at 750nm. Photoacoustic signal from cells at 750nm indicates the retention of cells distributed within the entirety of an OA scaffold at the conclusion of the culture. Cross sections from rows A , B, and C, depict slice #180, #130, and #70 respectively (D). Cross sections appear to have cells distributed only on the surface; however, this is an artifact of the Beer-Lambert law, where the concentration of absorbers was too high. When rotated, photoacoustic signal is present in re-endothelialized scaffolds (E, F).

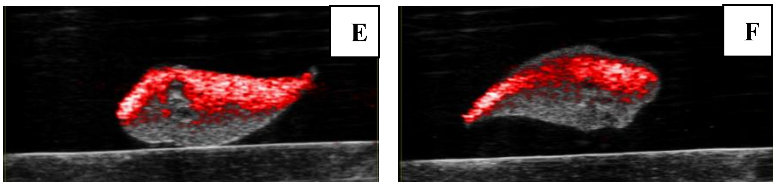

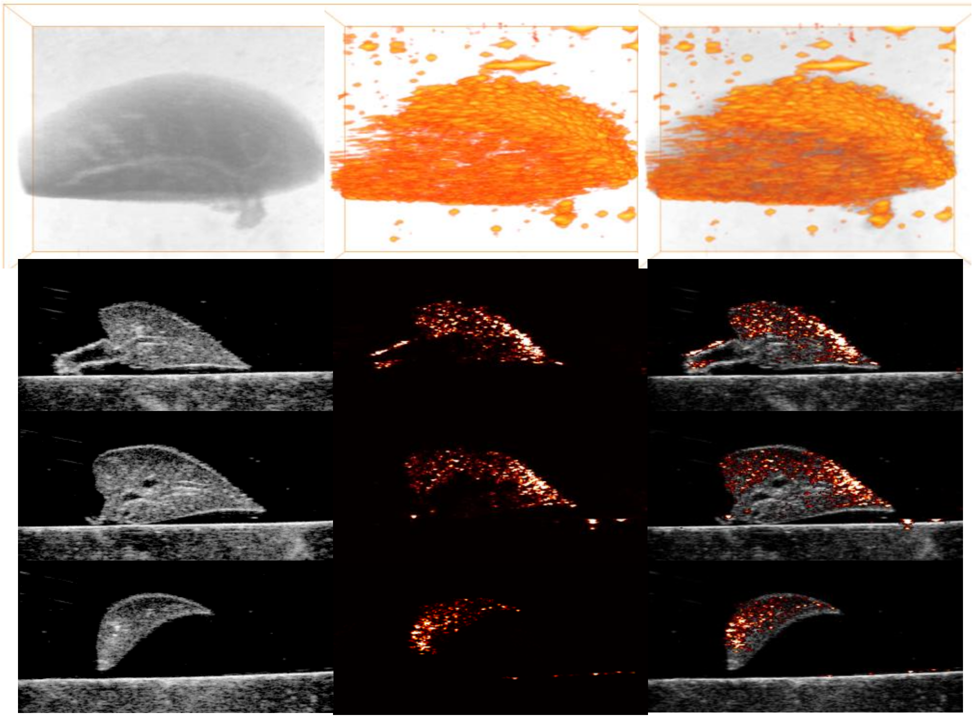

Figure 45. Perfusion culture following HDMEC re-endothelialization with improved US/PA processing. Three injections of 3.3×10^5 HDMECs, half with gold nanoparticles in 3.3 ml media over two hours were delivered to an OA scaffold. Cells were allowed to adhere overnight before gradually increasing perfusion flow was administered (3.2 dyn/cm^2 for 24 hours, 8.7 dyn/ cm^2 for 12 hours, 19.6 dyn/ cm^2 for 24 hours). Photoacoustic signal from cells at 750nm indicates the retention of cells distributed within the entirety of an OA scaffold at the conclusion of the culture.

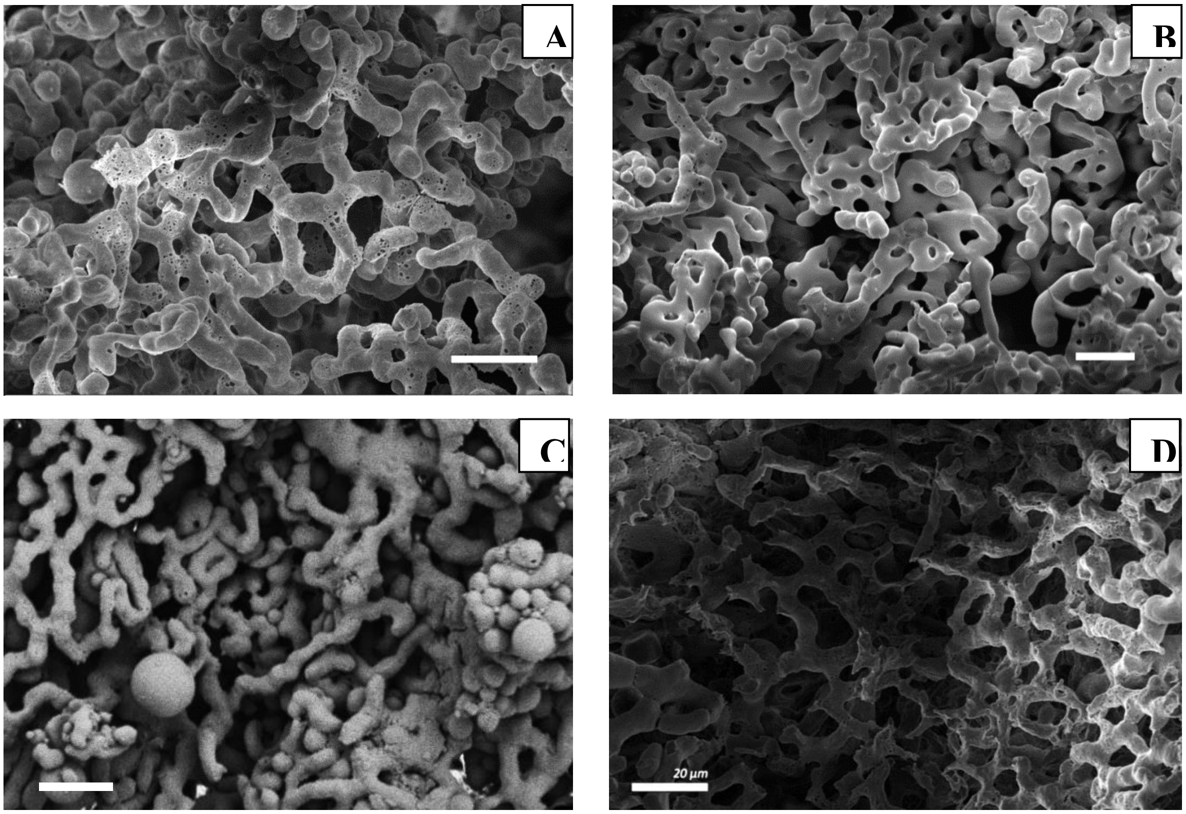

Figure 46. Vascular corrosion casts of re-endothelialized OA scaffolds with HUVECs (A) and HDMECs (B) following perfusion culture for 60 hours. Media was rinsed from scaffolds then fixed before vascular corrosion casting performed. Vascular networks from re-endothelialized scaffolds with HDMECs closely resembled those of fresh tissue (D), compared to decellularized scaffolds alone (C). Scale bar = 20 µm

presence was observed in both re-endothelialized groups along large vessels that normally appear smooth following decellularization (**Figure 47**). From a qualitative assessment, OA scaffolds re-endothelialized with HDMECs demonstrated capillary formations more closely resembling native vascular structures than cell-barren OA scaffolds (**Figure 46**). HUVECs failed to improve the vascular patency of OA scaffolds to the same extent as HDMECs. In addition, HUVECs aggregated in OA scaffolds more than did HDMECs (**Figure 48**). Quantitatively, HDMECs had significantly less extravasations in each diameter range compared to decellularized scaffolds and were statistically indistinguishable from fresh tissue casts in all but extravasations of less than 10 microns in diameter (**Table 2**). In addition, the total extravasational volume of re-endothelialized scaffolds was much lower than all other decell methods (**Figure 49**). Re-endothelialized scaffolds resulted in $2.05\text{x}10^5$ $\mu m^3/mm^2$, which was one-and-a-half times fresh tissue volume of $1.3\text{x}10^5$; whereas barren OA (the next lowest) resulted in $5.97\text{x}10^5$ $\mu m^3/mm^2$, a nearly a three-fold increase over re-endothelialized tissue.

4.3.4 HDMEC Re-endothelialized OA Scaffolds Clear Perfused Blood Compared to Barren OA Scaffolds

Upon harvesting fresh lung, some aggregation of blood could be seen macroscopically, however, the tissue was largely blanched allowing for effective analysis subsequently (**Figure 50**). Following whole-blood perfusion, significant red blood cell (RBC) aggregation could be visualized macroscopically in each group, although the filling patterns varied drastically (**Figure 50**). Initial perfusion into barren OA scaffolds was very structured, flowing into a defined vascular space—with various branching; however, blood began to rapidly fill the entirety of the scaffold, causing uniform coloration. Conversely, freshly harvested lung demonstrated a more controlled filling of

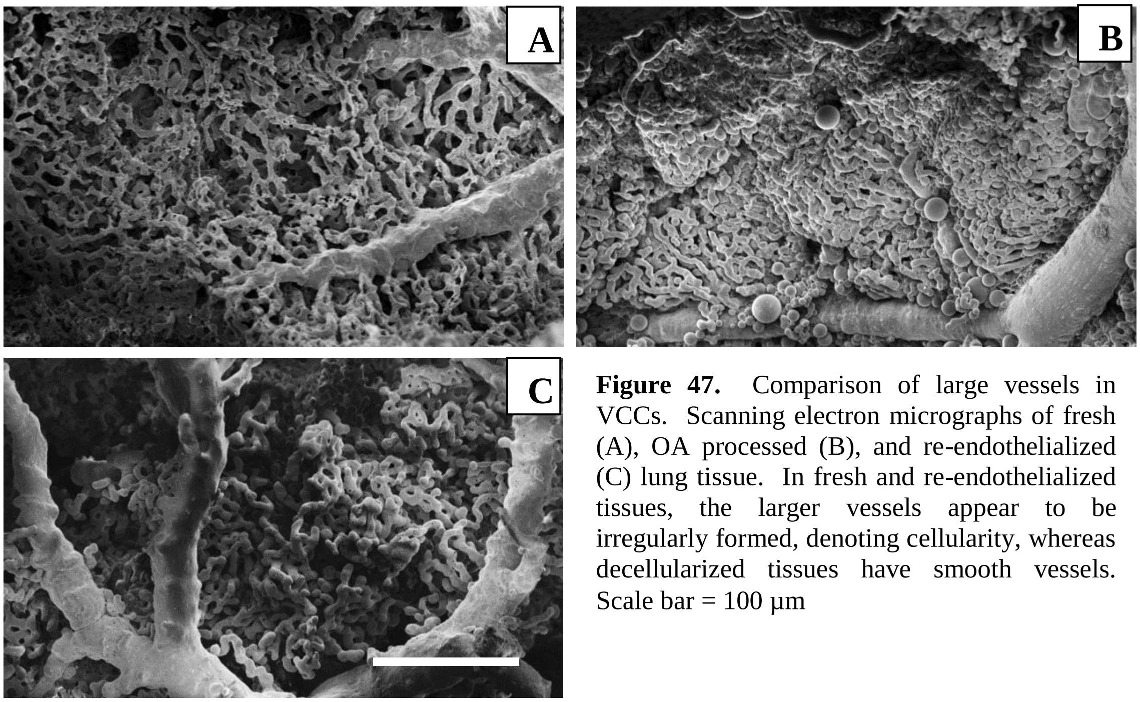

Figure 47. Comparison of large vessels in VCCs. Scanning electron micrographs of fresh (A), OA processed (B), and re-endothelialized (C) lung tissue. In fresh and re-endothelialized tissues, the larger vessels appear to be irregularly formed, denoting cellularity, whereas decellularized tissues have smooth vessels. Scale bar = 100 µm

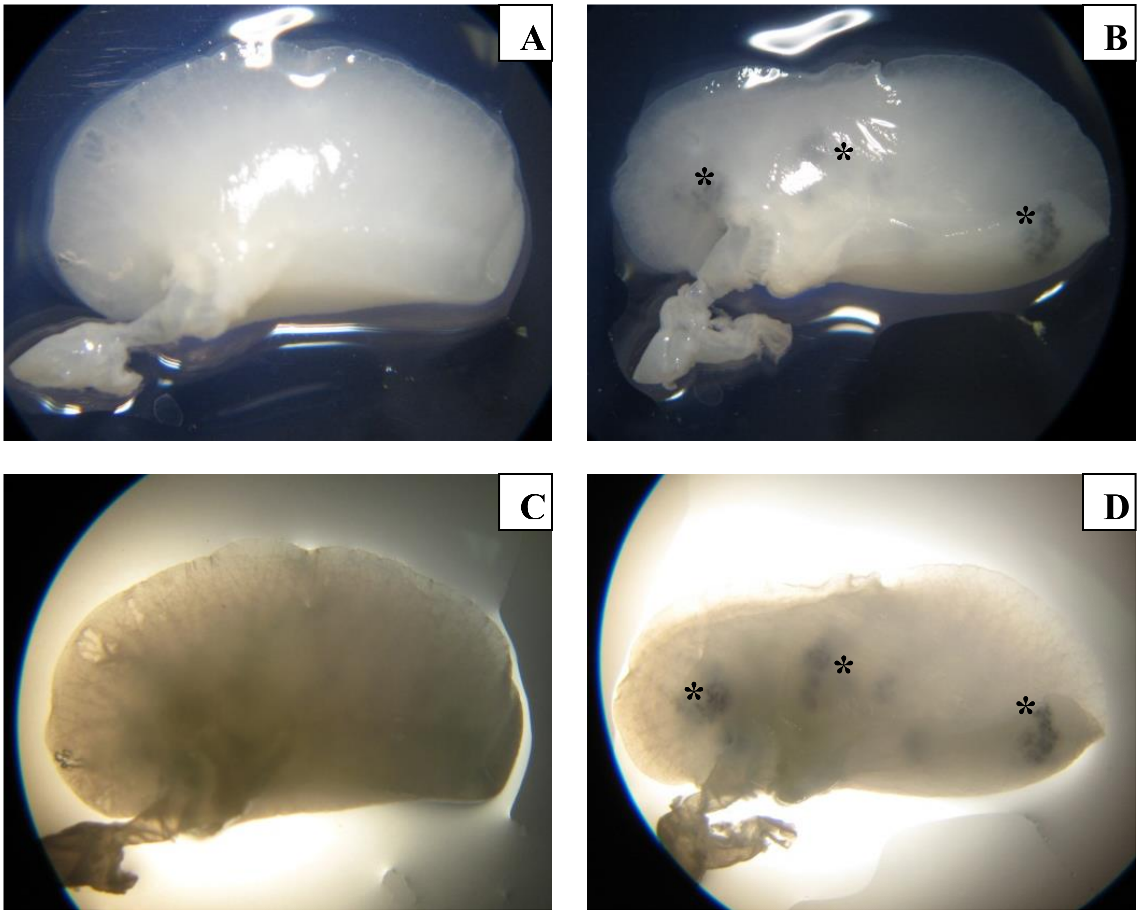

Figure 48. Photographs of re-endothelialized OA scaffolds. HDMEC (A, C) and HUVEC (B, D) cells were injected into decellularized lung then underwent perfusion culture for 60hr using a gradually increasing shear stress protocol. Some cell aggregates were present in the lungs injected with HUVECs (asterisks).

Table 2. Extravasation Counts per mm^2 for Different Decellularization Methods and Re-endothelialization

	Decellularization Method				
Extravasation Diameter	Fresh	OA	PSDS	POA	Re-Endo
Less than 10	95.26 ± 113.88	4125.19 ± 4978.53*	418.76 ± 541.80†	4494.30 ± 2691.37*‡	751 ± 872.26*†Ø
10 to 20	24.01 ± 40.96	119.44 ± 11.70*	374.99 ± 474.49*	464.08 ± 425.11*†	25.88 ± 53.16†‡Ø
20 to 30	3.37 ± 9.80	9.80 ± 19.53	71.78 ± 87.78*†	55.55 ± 65.25*†	11.14 ± 32.06‡Ø
Greater than 30	3.80 ± 5.88	2.56 ± 10.21	246.28 ± 148.39*†	18.15 ± 23.84*†‡	1.36 ± 4.29‡Ø

Asterisk, dagger, double dagger, and ø denote significance ($p<0.05$) versus fresh, OA, and PSDS, and POA groups respectively

Table 2. Extravasation counts following vascular corrosion casting of fresh, decellularized, and HDMEC re-endothelialized lung tissue. Re-endothelialization of OA scaffolds significantly improves the number of extravasations present following VCC. Re-endothelialized lung had significantly fewer extravasations than OA lung of less than 10 microns, and 10-20 microns in diameter.

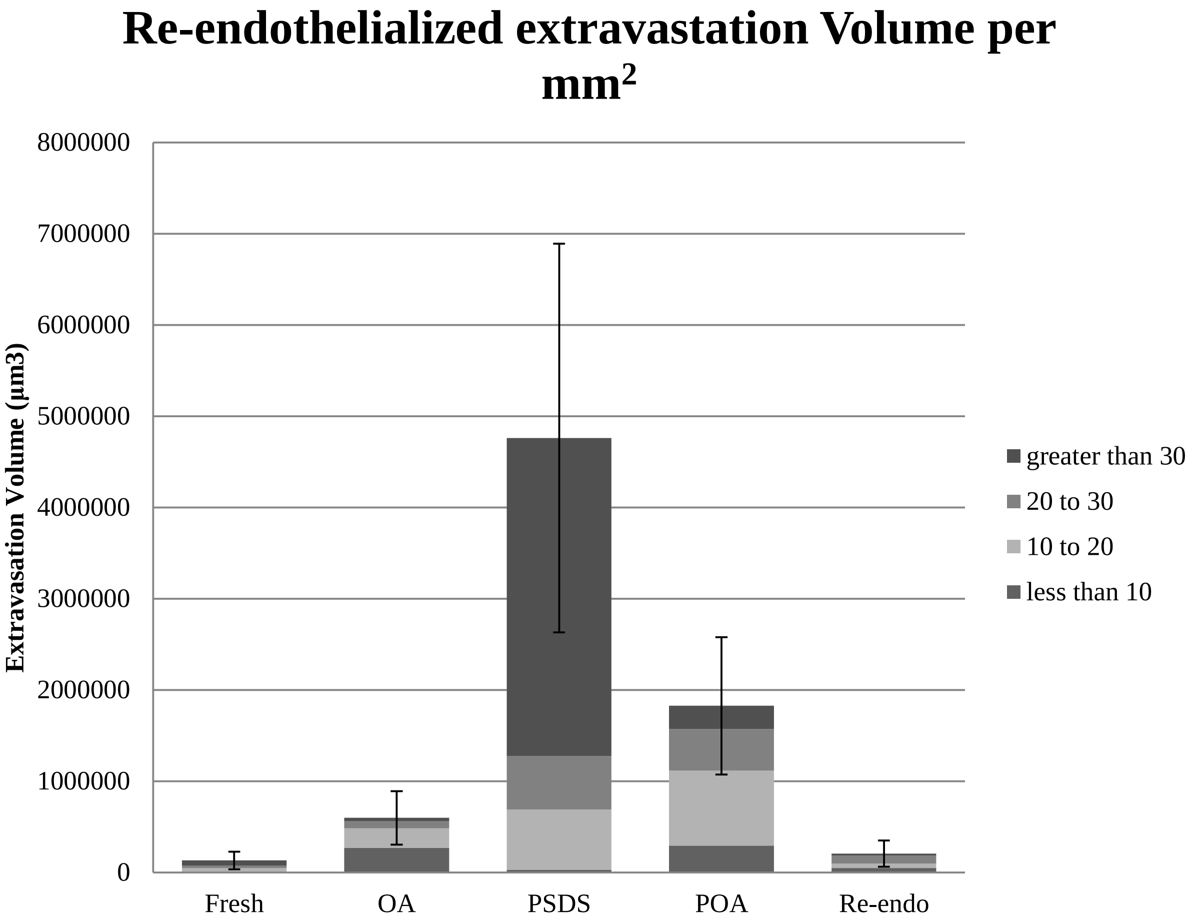

Figure 49. Total extravasation volume was calculated per mm^2 by cubic micron for each decellularization method investigated, as well as re-endothelialized lung. Re-endothelialization with HDMECs clearly rescues some of the vascular patency of the OA tissue.

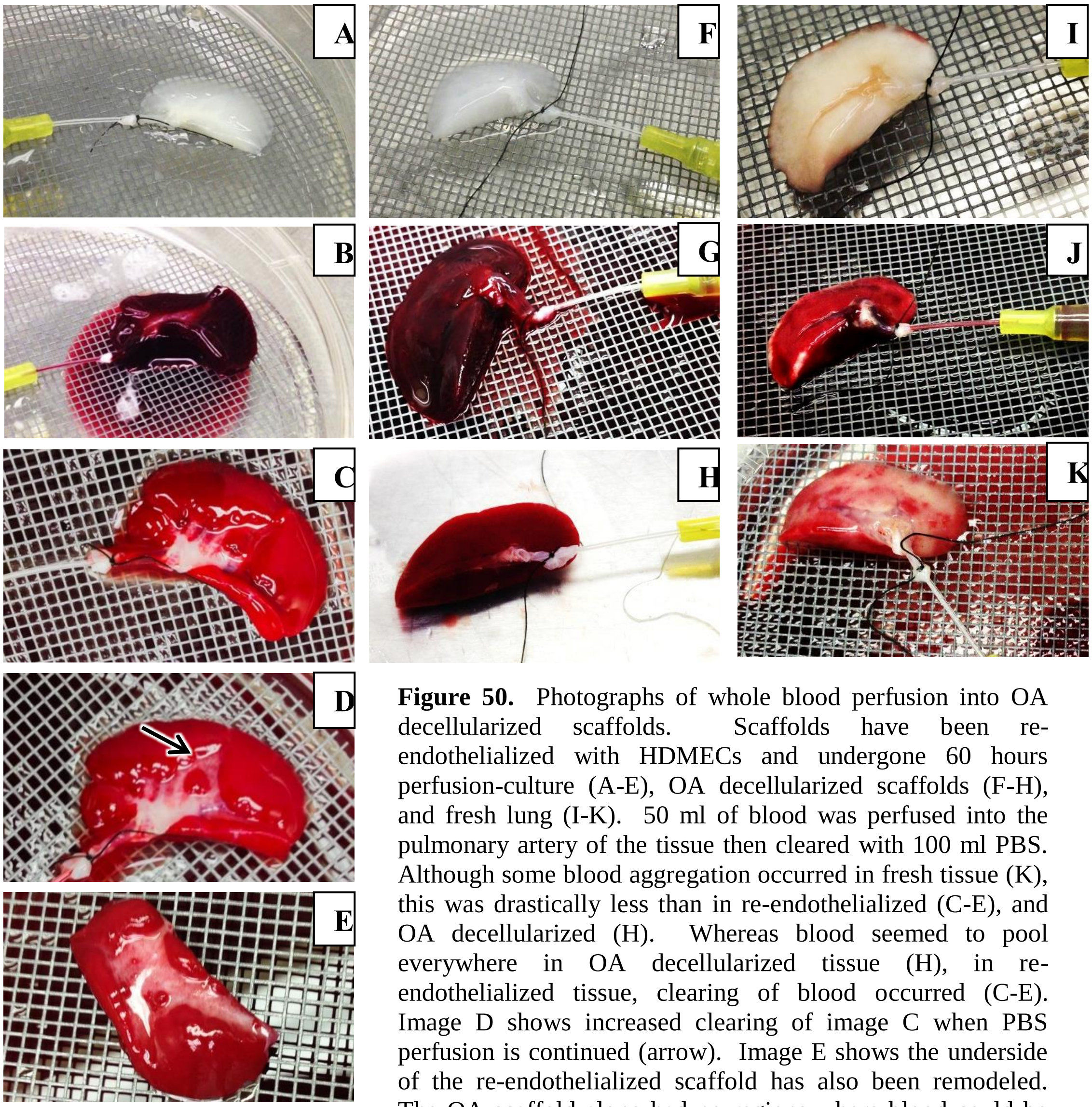

Figure 50. Photographs of whole blood perfusion into OA decellularized scaffolds. Scaffolds have been re-endothelialized with HDMECs and undergone 60 hours perfusion-culture (A-E), OA decellularized scaffolds (F-H), and fresh lung (I-K). 50 ml of blood was perfused into the pulmonary artery of the tissue then cleared with 100 ml PBS. Although some blood aggregation occurred in fresh tissue (K), this was drastically less than in re-endothelialized (C-E), and OA decellularized (H). Whereas blood seemed to pool everywhere in OA decellularized tissue (H), in re-endothelialized tissue, clearing of blood occurred (C-E). Image D shows increased clearing of image C when PBS perfusion is continued (arrow). Image E shows the underside of the re-endothelialized scaffold has also been remodeled. The OA scaffold alone had no regions where blood could be readily perfused out and cleared.

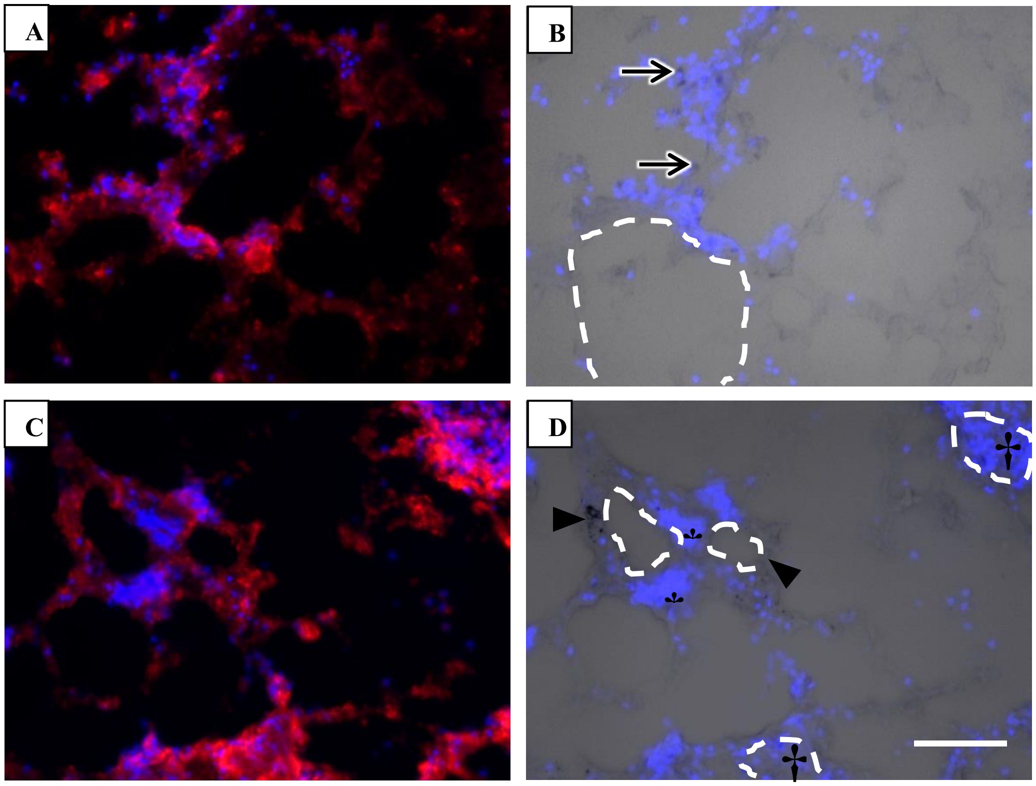

Figure 51. OA scaffolds re-endothelialized with HDMECs help decrease leakage of whole blood. Following re-endothelialization and whole-blood perfusion, scaffolds were perfused with PBS to clear blood. Sections were stained for CD-31 (A, C), staining positively for endothelial cells and platelets, and DAPI. The majority of positive staining for nuclei was likely from white blood cells from blood. Extensive leakage of blood unable to be cleared was seen (A, B). Blood leakage can be visualized in A and B around the top of the vessel (demarked with a dashed line). Although occlusion failed to occur, the resultant leakage can be traced. An overlay with brightfield imaging (B) shows the presence of red blood cells (arrow). C and D demonstrate a working vascular pair. Some damage in the form of cell aggregation can be seen (asterisk) which failed to occur in the regions containing nanoparticles (arrowhead). In contrast, occlusions were present in other vessels present (dagger). Scale bar = 200 µm

the tissue, and took slightly longer to achieve full perfusion. Re-endothelialized scaffolds followed a mixture of the two methods, with the majority of the tissue filling similarly to barren OA scaffolds, and a few regions which took slightly longer to become fully perfused.

When perfused with PBS, the distinctions between the experimental groups became more evident. Barren OA scaffolds failed to eliminate the blood that was present throughout the entirety of the scaffold. Fresh tissue became largely blanched, although regions of RBC aggregation could be visualized. Re-endothelialized scaffolds remained largely perfused with RBCs; however regions of the tissue cleared over time, suggesting cellularity does play a role in the functionality of the vascular patency. All experimental groups achieved clearing of blood in the pulmonary artery and vein.

Upon sectioning re-endothelialized tissue, staining for CD-31 could be visualized extensively (**Figure 51**). Although this antibody labels endothelial cells, it also labels platelets—which likely encompassed the majority of the positive signal present. By evaluating fluorescence and brightfield images, leakages of the vascular network could be seen. In some of the vascular pairs present, nanoparticles could be seen, and were associated with improved vascular performance.

4.4 CONCLUSIONS

Implementing a novel imaging technique, we were able to optimize a re-endothelialization protocol for our scaffold that allowed for cells to penetrate the entirety of the construct. The OA scaffold then served as a vascular substrate for endothelial growth to which pulsatile flow could be delivered continuously over 60 hours, which—in the case of HDMECs—improved vascular patency demonstrated through vascular corrosion casting methods. Ultimately this re-endothelialization technique was able to translate to improved vascular function by improving the blood clearing of the tissues.

Chapter 5: Discussion

5.1 INTRODUCTION

Creating functional *de novo* vascular networks has become the paramount objective of tissue engineering research. The number of people on the donor list far outnumbers the amount of available organs each year. To help rectify this discrepancy, scientists have looked to tissue engineering therapies to help decrease the burden of available organs. However, the most successful tissue engineering products to date have been limited to thin (less than 200 µm thick) organs such as tissue or bladder, or avascular tissues such as cartilage. Thicker constructs have failed due to their inability to sustain the viability of cells within them. Without proper nutrient delivery and gas exchange, a necrotic core forms instead. Thick tissue engineering constructs that contain a functioning vascular network prior to implantation would be able to sustain cellular viability. Furthermore, creating a scaffold that could be rapidly anastomosed to the host vasculature upon implantation would enable rapid nutrient and gas exchange to occur. We have explored the use of decellularization to leave behind a vascular architecture while removing the cellular material that would present an immunogenic response upon implanting the scaffold. The acellular scaffolds were examined for their ultrastructural composition, as well as their vascular functionality, then recellularized to assess the subsequent vascular recovery possible.

5.2 SELECTING VASCULAR TISSUES

Different organs have been investigated on their potential to improve vascularization *in vivo*. Specifically, omentum has proven a popular organ because of the ease with which it may be harvested, and its high vascularity. Omentum has been decellularized and used as a scaffold to improve vascularization—which has been commercialized into several products; however, this tissue is only several hundred microns thick and best suited for smaller vascular patch applications. Liver and lung represented a comparatively thick tissue that was also highly vascularized. Lung proved to be a better selection for our tissue source because of the relative ease to isolate only one lobe with a singular vascular axis, facilitating the ability to create an arteriovenous loop upon implantation—one of the main objectives of the research. Furthermore, the passive delivery of detergents for decellularization utilized in the OA process was able to effectively decellularize lung tissue far more than liver.

5.3 OPTIMIZED ACELLULAR DECELLULARIZATION OF LUNG

The OA method developed previously in our lab has proven to be a successful means to eliminate cellular material [73]. This method was further investigated on its potential to be applied to decellularizing vascular tissue because of its ability to preserve the basal lamina of sciatic nerve tissue—whose 5-10 μm lumina diameter are on a similar scale to capillaries (2-15 μm). The segments of lung ranging in thickness (1, 2, 5 mm) demonstrated the ability for the OA process to remove cellular material following observation of ultrastructural H&E staining. Even in the smaller segments, the OA process was able to preserve an ECM structure that was similar to native tissue. This suggested the ability of this process to be used without damaging the ECM structure on the exterior of the tissue—which was more readily perfused with detergents. The OA process needed modification based on early immunohistochemistry suggesting that cellular material was still present at the conclusion of the decell process. Although nucleic material was not seen, the labeling of cellular surface material (the endothelial glycoprotein, CD-31) could potentially elicit an immune response upon scaffold implantation. Subsequently, the decell detergent incubation times were doubled to ensure the removal of cellular material.

5.4 DIFFERENCES IN DECELLULARIZATION TECHNIQUES DIFFICULT TO ELUCIDATE USING STANDARD HISTOLOGICAL ANALYSES

Three decellularization methods were chosen for comparison, OA, PSDS, and POA. These methods were each generally effective in removing cellular material, while leaving behind an organized ECM, as demonstrated through histology and immunohistochemistry; however, these methods are qualitative and fail to appropriately characterize the extent to which the vascular functionality of the tissue is preserved. Additional qualitative methods including HPLC analysis are used to measure the amount of protein that remains; however, HPLC analysis of decellularized tissue cannot give quantitative values because of the cellular control, and offers no insight as to the functionality of the remaining ECM.

The paramount objective of our decellularization methods was to remove the immunogenic component of the tissues while keeping the patency of the vascular network intact down to the capillary scale. Such a construct could potentially be used as a cell culture system that supports physiological flow *in vitro*, and could be directly anastomosed to the host vascular system upon implantation *in vivo*—allowing for immediate perfusion to the entirety of the graft, and preventing necrotic core formation. If damage occurred to the vascular network, the ability to properly perfuse the whole graft would be compromised, essentially rendering it a construct with a leaky hemorrhagic *de novo* network. By utilizing qVCC we would be able to more accurately assess the chief function of our scaffold and appropriately award merit to our decellularization methods.

The decell methods selected were chosen based on successful decellularization of other tissues in rat. Hudson *et al.* successfully used the amphoteric sulfobetaine detergents SB-10 and SB-16, along with the anionic detergent Triton X-200 to preserve basal lamina in nerve—the dimensions of which are on similar scale to capillary networks [73]. Ott *et al.* successfully used the anionic detergent SDS along with the nonionic detergent Triton X-100 to decellularize heart tissue, subsequently demonstrating functionality of the tissue using mechanical testing [76]. In our aim of preserving the capillary networks of lung tissue, we focused on optimizing the decellularization protocol from the work by Hudson *et al.* on the thicker, yet less dense lung tissue, while leaving the protocol from the Ott study intact. Although better suited for another tissue source, we valued the PSDS method as comparison—as well as an example of results that occur when decellularization methods are not properly tailored for their particular application. Finally, the POA method was used as another comparison method, investigating the gentler detergents of the OA protocol, with the rapid delivery of the PSDS method.

H&E staining demonstrated that the general architecture was maintained following decellularization in each of the decell methods tested. Some erratic hematoxylin was seen in some of the PSDS tissue samples; however the staining was not specific to nuclei, and was likely binding to the residual anionic detergent that failed to rinse away. This method utilized SDS, a powerful anionic detergent that commonly binds to basal proteins and is difficult to rinse away [117-119]. Although evident when looking macroscopically at the decellularized tissues—the decellularized lung from perfusion methods were more translucent than from the OA method, suggesting lack of cellular material. Further evidence that residual detergents were responsible for cationic staining was confirmed in the quantitative DNA analysis of the tissues following decellularization. Each decellularized scaffold analyzed for DNA content demonstrated significant removal of DNA compared to fresh lung, and in fact, the perfusion methods resulted in a larger decrease in DNA content than with the OA method. Thus the cationic agents used to detect anionic residues could only be from the bound anionic detergents.

The immunohistochemistry analysis performed demonstrated a conservation of bioactivity in the ECM proteins stained against in the decell groups comparable to the fresh control tissue. Staining for cellular markers showed an attenuation of signal following decellularization compared to the fresh control. The POA method seemed to perform the poorest in this respect, although the technique effectively eliminated nucleic material. Using immunohistochemistry techniques alone, decellularization efficacy was not immediately evident. More interesting is how the functionality of the scaffold could be further exploited. To assess this functionality, additional analytical methods were needed.

5.5 QUANTITATIVE VASCULAR CORROSION CASTING EFFECTIVELY DISTINGUISHES DIFFERENCES IN VASCULAR PATENCY BETWEEN DIFFERENT ACELLULAR SCAFFOLDS

Vascular Casts (VC) have been used to image and explore the morphology of vascular networks and structures since the 1980s [102, 103]. These permanent representations of the vascular luminal space are obtained after the process of perfusing the vascular system to remove blood, injecting the vasculature with resin, allowing the resin to polymerize, and finally removing the surrounding tissue (Vascular Corrosion Casts or VCC), or optically clearing the surrounding tissue. These polymer casts can then be used to accurately visualize vascular structures down to the capillary scale. Scanning Electron Microscopy (SEM) and Confocal Microscopy techniques are the most commonly used to investigate the vascular structure preserved by the cast due to the high resolution images they are able to produce [109, 110]. Ohtake *et al.* demonstrated the use of VCs to elucidate differences in damaged tissues [120]. After evaluating vessel defects, truncations, and extravasation patterns, they found larger extravasations correlated with their increased microvascular injury [120]. Our technique aimed to quantitatively describe the similarities and differences between the microvascular networks present in fresh tissue and following decellularization.

The cannulation of the OA vascular axis was not a straightforward process and is deserving of elaboration. Initial attempts to cannulate the pulmonary artery required a detailed examination of the tissue structure remaining. The harvested tissue consisted of of the pulmonary artery—with its intact bifurcation, a bronchus, and the pulmonary vein—consisting of two merged vessels from the lung. Initial attempts to cannulate the tissue included the use of a metal syringe that was inserted in the pulmonary artery past its bifurcation. The transected ends of the pulmonary branches—leading to the heart and the right lung—were clamped off. The resistive force encompassing perfusing the tissue proved to be too great for the insertion site of the syringe, and resulted in backflow escaping the vessel. Another problem with the syringe method was the propensity for the syringe to puncture the vessel. The next evolution utilized a rigid 24 gauge cannula to prevent punctures from occurring. Attempts to create a secure connection included the use of photocrosslinkable dental resin—which ultimately failed to prevent backflow. Finally, a cuffed cannula was created in house using PDMS resin. This was secured in place with a ligation of silk suture placed proximally to prevent slippage of the tissue, while also ligating the pulmonary bifurcation—leading to successful cannulation. The 2 ml/min injection speed was taken from typical injection speeds from literature [121].

In characterizing the qVCC data we correlated larger extravasations with greater luminal damage. Given small leaks in the lumina of our vessels, we would expect to see smaller extravasations; whereas a larger leak would result in more rapid diffusion out of the luminal space and henceforth larger extravasations. These sentiments are in agreement with previous studies characterizing extravasations in relation to increased, manually-induced vascular damage in the brain [120]. From our results the OA method resulted in the most small (less than 10 micron) extravasations; however, when counting medium (10-30 micron) and large (over 30 microns) extravasations, the perfusion-based methods had the most. When analyzing the total volume of extravasations, we gain a clearer insight to the amount of damage present in the vascular network. Of the decell methods tested, the perfusion-based methods had much more total extravasational volume when compared to the diffusion-based OA method, and fresh tissue. When performing the qVCC analysis, very little variation in extravasation number and type was seen throughout the scaffold of a particular decell method as opposed to comparing techniques to each other.

Differences between VCs of different decell scaffolds could also be seen upon macroscopic evaluation. The colors of the VCs were different—with fresh lung control the most white color, and perfusion decell methods containing pinkish hue to them, directly correlated the amount of vascular damage in the scaffolds. The white color seen in the fresh VCs was a result of the fine lattice of capillaries that was cast. The optical density of the capillaries would be less due to their small diameters, especially compared to the large extravasations seen in the perfusion-based decell methods. Furthermore, the composition of the fresh VC was much more robust, compared to the perfusion-based methods—which were primarily a loose composition of extravasations compared to the continuous capillary-rich fresh tissue.

Although unclear at the moment as to the correlation between increased vascular ECM damage and subsequent scaffold performance both *in vivo*, the correlation between improved vascular networks and subsequent vascular clearance of blood is a strong starting point for improving decellularized vascular tissue. The importance of a continuous vascular ECM could relate to the role of the ECM in vascularization. Following an injury, the vascular basal membrane is first degraded, ECs then proliferate and migrate within tissues containing interstitial collagen [63, 64]. Interactions with collagen cause a spindle-like morphology that will eventually reorganize into lumina over time [65, 66]. The transduction of mechanical forces through the ECM allows ECs to establish tension-based guidance pathways, leading to interconnected cords. Another important function of the ECM is to sequester cells. Research has demonstrated that the conformation and orientation of fibronectin are key components in EC cell adhesion [68]. This important finding, intimates at the importance of being biomimetic not only in biochemical composition, but also in spatial architecture. Overall, the ability of endothelial ECM to direct EC fate makes scaffold composition a significant characteristic to define in a vascular scaffold.

5.6 OA PROCESSED SCAFFOLDS ARE IMMUNE TOLERATED

Fischer 344 rats were used as donors to provide isografts and allografts to Fischer and Lewis rats respectively. Left lung lobes from donors were harvested and decellularized using the OA process. These decellularized scaffolds were implanted subcutaneously in rats for one or four weeks in either an allograft or isograft model. The one and four week implantation durations were chosen to see different stages in the immune response of rats. In similar implantation studies utilizing ECM scaffolds, the onset of the immune response occurs after eight hours [122]. Cellular infiltration is common and primarily consists of macrophages and other polymorphonuclear (PMN) cells. After eight days, the PMN cells are gradually replaced with fibroblasts. In our study, the presence of macrophages within the scaffolds after one week was consistent between allograft and isograft models, with no appreciable difference. For every 100 cells present, about six were macrophages. Following implantation for four weeks, the scaffolds were extensively remodeled, although fibrous encapsulation occurred. Unsurprisingly, the fibrous tissue surrounding the scaffolds contained a higher density of macrophages than within the scaffolds—these data were not quantified. Interestingly, histological staining around the bronchus of the OA scaffold after four weeks revealed a dramatic increase in cellular infiltration when compared to migration through the exterior of the scaffold; however, immunohistochemistry of these regions with increased cellularity failed to detect the presence of macrophages. Macrophage counts between within the scaffolds were decreased from the one-week explants, and in fact allografts had lower cell counts per nuclei counted than isografts; however, this difference would equate to one less macrophage in allografts for every 100 nuclei counted. The total cell counts in the one-week explant demonstrated more cellular infiltration occurred in the isograft scaffold; however total cell counts were equivalent after four weeks.

A positive control depicting an immune response was not used because the analysis of immunogenicity in our experiment was performed by counting cells that migrated into the scaffold. If a scaffold that was not decellularized was taken from a Lewis rat and implanted into a Fischer rat, then cellular infiltration might not be the same as comparing two decellularized scaffolds—which should be more permissive to cellular infiltration.

An analysis of the histocompatibility between the two rat strains suggests a positive immune response should occur in Lewis rats, provided the decellularization process failed to remove the relevant histocompatibility complexes. Stark and Kren found $RT1^{l}$, $RT2^{a}$, $RT3^{a}$, $RT7^{a}$, and $RT8^{b}$ to be the major histocompatibility complexes in the Lewis rats used [123]. Fischer rats were found to contain $RT1^{lv1}$, $RT2^{a}$, $RT3^{b}$, $RT8^{b}$ [124]. Two of the histocompatibility complexes are identical, however there are six differences, indicating an immune response would be expected given a lack of histocompatibility. Thus, the OA method was effective in removing immunogenic components as verified by the similarities in the explants between the two groups.

In a tangential finding, subcutaneously implanted scaffolds were able to support the viability of cells in the entirety of the explant. This explant was remodeled into a uniform round disc after four weeks *in vivo* but still retained significant amount of volume (approximately 1-2 cm in diameter). Immunohistochemistry targeting the endothelial glycoprotein CD-31 was present throughout the explant, and was more prevalent than macrophage cells (Appendix). This finding was surprising, considering a fibrous capsule formed around all the scaffolds. This finding points at the capacity for cellular ingrowth utilizing this scaffold.

5.7 ULTRASOUND GUIDED PHOTOACOUSTIC IMAGING IS AN EFFECTIVE TOOL TO DISPLAY CELLULAR DISTRIBUTION

The technique of US/PA imaging has been pioneered by researchers at The University of Texas at Austin. Drs. Stanislav Emelianov and Laura Suggs have implemented this technique with the end goal of tracking cells delivered *in vivo*. Although many complications regarding cellular interactions, nanoparticle retention and expulsion, and subsequent nanoparticle uptake by other cells remain obstacles to translating this technique *in vivo*, the applications of US/PA imaging *in vitro* are attractive.

Previous research utilizing this technique has demonstrated the capacity for hMSCs cultured with the same gold nanotracers to maintain viability and engage in the same phenotypic changes observed without nanotracers—when being cultured in different 3-dimensional matrices. These cells were differentiated using PEGylated fibrin gels as previously described [125]. Briefly, hMSCs (Cambrex, East Rutherford, NJ) were cultured for one week in serum-containing MSCBM medium (Cambrex) supplemented with MSCGM SingleQuots (Cambrex) prior to gel seeding at 5x10^4 cells/ml, fibrinogen at 10 mg/ml, thrombin at 12.5 U/ml, and difunctional SC-PEG (succinimidyl carbonate, 3400 Da, Sunbio, Anyang City, South Korea) at a 10:1 molar ratio to fibrinogen. After seven days of culture *in vitro* the photoacoustic signal was still present, although somewhat attenuated due to cell division and exocytosis. These cell-seeded gels were also maintained for 10 days in a rat hind limb implantation model, with signal present at the conclusion of the study [126]. With these studies already published, the concept of using US/PA imaging to track the distribution and retention of cells within the OA scaffold was promising. This technique allows for specific detection of localized nanotracers due to plasmon resonance resulting in a red-shifted peak broadening of light absorption by aggregated nanotracers.

5.7.1 Cellular Uptake of Nanotracers Does Not Alter Cell Fate

Cellular uptake and subsequent behavior was of paramount importance in order for US/PA to be a plausible method for observing cellular distribution subsequently. We initially chose a seeding density that was comparable to previous studies in our department that utilized mesenchymal and adipose-derived stem cells. Following 24 hours of incubation, nanoparticles were readily taken up by both endothelial cell lines used as verified through brightfield and darkfield imaging. After expanding these cells out to confluency, general morphological characteristics were consistent with endothelial cells. Both HDMEC and HUVEC cells took on a cobblestone-like morphology in phase contrast images.

The results of the MTS assay revealed the inert qualities of the nanotracers when taken up by cells. Although there was a significant difference between HUVECs monitored 24 hours following the addition of nanoparticles ($p<0.01$), the difference in observed MTS fluorescence intensity at 490 nm for cells cultured with nanoparticles was only 15% less than intensity observed in cells cultured without nanoparticles. Furthermore, when cells were expanded out for an additional two days, the MTS activity was equivalent between cells with and without nanotracers having been added. MTS activity in HDMECs was also equivalent in 24 and 72 hour culture conditions, suggesting the inert influence of nanotracers on the cells.

5.7.2 US/PA Imaging Effective at Detecting Cellular Distribution in OA Scaffolds

Whereas researchers in the past used histological sectioning to investigate the distribution of cells implanted into decellularized tissues [18-20, 76, 117, 119], we utilized a technique that could accurately map the distribution of cells throughout the entirety of the scaffold, without reconstructing a series of physical tissue sections. In selecting this method we were able to at-once visualize cells, enabling greater ease in optimizing re-endothelialization parameters, as well as communicating the data through transparent publishing—opposed to selecting one "representative image."

US/PA imaging demonstrated differences in cellular distribution depending on injection density, as well as periodicity. Upon injecting cells containing nanotracers in the OA scaffold, it was important to verify that the PA signal detected was only from the nanotracers in the cells, and not loose systemic nanoparticles that might have been exocytosed. An initial injection of nanoparticles alone was used to verify that PA signal was not present from nanoparticles alone; however, PA signal was detected close to the site of injection, although not in the larger vessels comprising the scaffold's vascular axis. This distinction was likely a result of nanotracer aggregation in the capillary beds within the scaffold. The ability to plug the capillaries using small microparticles has been performed by researchers attempting to obtain VCCs depicting the larger vessel structure of the tissue, without obstruction from the dense capillary beds [127]. Plugging the capillaries would allow for subsequent nanotracer aggregation and the red-shifted plasmon resonance frequency to be detected. This study highlighted the importance of optimizing the injection parameters to allow for broad cellular distribution without plugging the capillary beds.

An injection schedule was then implemented that allowed for broad distribution of cells throughout the scaffold. Cells injected from $5.5\text{x}10^4$ to $1.1\text{x}10^5$ cells/ml did not aggregate in capillaries; however, when increasing the number of cells, the subsequent injections needed to be split into a series of smaller injections in order to prevent aggregation of cells within capillaries.

Once injected within the scaffolds, the ECs with nanotracers were able to be imaged upon injection and at the conclusion of the study with US/PA imaging, demonstrating cellular distribution. Cells were able to penetrate throughout the entirety of the scaffold, and were maintained despite the addition of physiological shear flow. Cross-sections of the US/PA imaging demonstrated that the cells were not present in the bronchus, further indicating the patency of the vascular network that remained, as well as the efficacy for the technique to visualize cells on a relevant spatial resolution. Histological evaluation further demonstrated that nanoparticles were contained within the cells. Although some free nanoparticles existed and cells can freely exocytose them, these nanotracers will not be detected by the 750 nm laser because they are not aggregated and hence will not present plasmon resonance.

A complication that occurred when using US/PA imaging following the injection of cells was utilizing too many nanoparticles. The increase in photoacoustic absorbers prevented the penetration of light in the scaffold as depth was increased. This resulted in no signal in the re-endothelialized scaffolds when moving away from the photoacoustic laser. According to the Beer-Lambert law (**eq. 2**) there were two ways to increase the penetration depth. In order to fully penetrate the scaffold, the sensitivity had to be decreased according to the Beer-Lambert law (**eq. 2**). Where δ is the penetration (cm), σ is the absorption cross section (cm^2), and N is the concentration of absorbers ($[cm^{-3}]$).

$$\delta = \frac{1}{\sigma N} \qquad \textbf{(eq. 2)}$$

To allow for greater penetration, we chose to leave the absorption cross section the same, while decreasing the number of absorbers—by using nanoparticle-loaded cells in only one of the three injections when re-endothelializing the tissue. This effectively solved the penetration problem.

Although uniform distribution could be visualized through US/PA imaging, and cells could be found throughout the scaffold sections, at the cellular level the entirety of the scaffold was not cellularized. Brightfield imaging revealed the presence of cells in the locations of nuclei visualized fluorescently; however although a minority, there were also nanoparticles present which were not associated with nuclei but were positive for CD-31 markers. Whereas the US/PA imaging was able to accurately reflect the distribution of cells within the scaffold, histological analyses are still needed to refine the total number of cells that can be permitted into the tissue.

5.8 RE-ENDOTHELIALIZATION AND PERFUSION-CULTURE WITH HDMECS IMPROVES VASCULAR PATENCY

The perfusion of cells into the scaffolds was performed as described above. The subsequent perfusion-culture was based off beneficial effects of shear flow on endothelial cells once anastomosed to the host vasculature (the end goal of this scaffold). Inoguchi *et al.*, found that a shear stress regimen of 24 hours 3.2 dyn/cm^2, followed by 8.7 dyn/cm^2

for 12 hours, and finally 19.6 dyn/cm^2 for 24 hours significantly conditioned the phenotype of endothelial cells in a large vessel setup [35].

5.8.1 Perfusion Set-up and Shear Calculations

To determine the shear stress on our cells, we used the Hagen-Poiseuille equation (**eq. 1**). Our perfusion system was more complex and consequently we needed to first determine what diameter to select as the diameter to base our calculations on. Since Inoguchi *et al.* implemented their shear stress regimen on large vessel—we looked at the largest vessel that was being cannulated as our starting diameter. The pulmonary artery of the Fischer rats at the age we harvested was measured to be around 0.5 mm at the point of cannulation, and was thus used as the diameter moving forward. The dynamic viscosity was based off the Inoguchi *et al.* study in which the media was found to have viscosity of 0.0075 dyn·s/cm^2. The flow rate was then determined that would result in the desired shear stress, which was then converted into pump-head rotations per minute—the control display for the iPump peristaltic pump we used.

The full perfusion of the lung was necessary to culture cells that span the entirety of the tissue. We also used flow rates that were within physiological conditions (160-180 ml·kg^{-1}·min^{-1} = 28-36 ml/min) [128]. This gave us a large target window that would allow for perfusion to occur. After a thorough literature search on right ventricle pressure, it was determined that the typical pressure for rat lung perfusion are generally between 5-18 mmHg for diastolic and 12-30 mmHg for systolic pressures for rats varying in weight and sex, but higher pressures can be tolerated [129-132]. Even at low flow rates, our pump was able to deliver more than enough pressure to fully perfuse the lung. As our system was open, the amount of pressure delivered to the scaffold could not be controlled, and was dependent on the resistive load of the tissue; however, full perfusion in all injection studies was seen, without damage to the major vessels of the scaffold.

Sterilization of the decellularized scaffold was a major challenge when attempting to perform the *in vitro* cell experiments. This has been an issue with using ECM-derived constructs in medicine. Standard sterilization methods such as ethylene oxide, peracetic acid, and gamma or e-beam radiation have all been used to sterilize ECM derivatives with differing levels of success in terms of efficacy and ECM preservation [133-136]. Although some damage has been seen following e-beam sterilization [133-135], typically involving partial denaturation of collagen, literature exists that demonstrates irradiation causes insignificant effects on ECM biochemistry and cellular affinity [136]. We used e-beam irradiation to successfully sterilize the scaffolds. This process had no visable effect on subsequent VCC and perfusion-culture studies; however, alternative methods such as supercritical carbon dioxide might be an alternative method for sterilizing ECM [137].

5.8.2 Vascular Patency Determination

Vascular patency of OA scaffolds following re-endothelialization with HDMECs (Rd-OA) outperformed barren OA scaffolds, as well as scaffolds re-endothelialized with HUVECs (Rv-OA). The differences were noticeable from the US/PA images acquired. PA signal was more clustered in Rv-OA than with Rd-OA scaffolds. This clustering was likely a result of aggregation in the capillary beds which in turn effected the perfusion of Mercox resin in the scaffold. A reason for this could be the relative size of the cells—with HDMECs being approximately half the size of HUVECs.

From a qualitative assessment of the VCCs, the Rd-OA scaffolds contained capillary architectures that resembled native tissue. These are slightly irregular capillary meshes, having non uniform diameters within the mesh. This is in contrast with Rv-OA scaffolds and the barren OA scaffolds, which had uniform tubular vessels.

Quantitative analysis of the VCCs substantiated the qualitative observations. Rd-OA scaffolds contained far less extravasations than barren OA scaffolds in all diameter subgroups that were inferior from fresh tissue, and were indistinguishable from fresh tissue in all but extravasations of less than 10 microns in diameter. As discussed earlier, the number of extravasations correlates to an increase in damage to the patency of the vascular network. The total extravasational volume from Rd-OA scaffolds was much less than the barren scaffolds and pointed to the superiority of the vascular structure after re-endothelialization.

CD-31 positive staining using immunohistochemistry demonstrated the presence and activity of the cells that remained in the scaffold following perfusion culture. VE-cadherin staining was not as strong. The fact that cells persisted in the tissue along vessels even when physiological shear stress was applied points to the viability of the cells within the tissue. Dead cells would not be attached to the ECM, especially under stress. Although cells were present in most of the sections imaged using bright field fluorescence microscopy, the numbers were far less than what would be seen in fresh tissue. Further investigation would be needed to find how many injections could be possible to increase cell numbers.

5.9 IMPROVED VASCULAR PATENCY IMPROVES CLEARANCE OF BLOOD IN DECELLULARIZED SCAFFOLDS

The same perfusion-culture system was again used to perfuse blood throughout the lung. In this setup, the kinematic viscosity was changed to that of blood (estimated to be between 0.03-0.04 Poise at 37°C [138]. An additional consideration was the shear rate being applied to the blood through our system. To be considered Newtonian, blood shear rate must be over 100^{-s} [139]. We also wanted to prevent hemolysis that might result from too high a shear coming from the cannula. Podgoreanu *et al.*, utilized a peristaltic pump to implement a successful bypass in a rat model [140]. They used an average flow rate of 160-180 $ml \cdot kg^{-1} \cdot min^{-1}$ (similar to the normal cardiac output of rats), along with a

20-gauge cannula injected into the tail vein to perfuse animals for 60 min. We calculated the shear rate for their setup again using the Hagen-Poiseuille equation (**eq. 3**), assuming a 350g weight which was the average range of the animals they used.

$$\dot{\gamma} = \frac{\tau}{\mu} = \frac{4Q}{\pi R^3} \qquad \textbf{(eq. 3)}$$

The shear rate was found to be 46069.54^{-s}. This value was then applied to our setup as a maximum value. We were able to use equations 1 and 3 to determine the associated shear stress, and then calculate the necessary flow rate given our radius of 0.0155 cm for the 24-gauge needle we use for our perfusions. It was then determined what flow rate we needed so as not to surpass this shear rate, depending on what the tubing length was (8.1 ml/min). We used a flow rate of 5.8 ml/min which had a shear rate of 32685.8^{-s} at the cannula and 983.19^{-s} at the vessel entrance. The shear stress was slightly higher than what we perfused into the construct using media at 23.75 dyn/cm^2 compared to 19.6 dyn/cm^2.

Following whole-blood perfusion, we were able to visualize repeatable differences between fresh tissue, barren OA scaffolds, and re-endothelialized OA scaffolds. The purpose of this study was to correlate the improved vascular patency determined through qVCC analysis with a physiological response. A flaw in this system is that the cause for blood aggregation is not understood absolutely. Aggregation of blood could be a result of clotting in vessels or simply pooling in the interstitial space outside the vascular network. In addition, the fresh rat tissue harvested was perfused with the same human whole-blood as the other scaffolds. This xenogeneic transfusion could result in an immune response, which could also explain the aggregation that occurred in fresh tissue. Despite these uncertainties, we believe clearing the tissues with PBS helped to visualize deficiencies in the vascular network regardless of the case. Vascular performance was particularly evident when comparing re-endothelialized scaffolds with barren OA scaffolds. Although vascular and capillary-like structures existed in the VCC of barren OA scaffolds, extravasations did exist, and were likely the cause of blood pooling in the interstitial space. This pooling was also seen in re-endothelialized scaffolds; however clearing of some of blood from regions of the scaffold was also demonstrated. This clearing most commonly occurred along the major vessels of the scaffold, and extended to the lower portion of the scaffold—following the pulmonary vein. In all experimental groups, the vascular axis became cleared of blood—demonstrating that some vascular integrity remained. Histological techniques showed the presence of vascular leakage which occurred in vascular pairs. Positive CD-31 staining depicting platelet presence was more evident in regions where clotting and leakage occurred. Brightfield imaging was helpful in finding regions of re-endothelialized cells, as wells as the presence of red blood cells. In areas where nanoparticles were visualized in brightfield imaging, there was a decrease in platelets and leakage, hinting at the importance of endothelial cells in this capacity.

The inability to clear blood from the decellularized tissue provides insight as to why the perfusion-based decellularization methods failed to remove some biological components (in the case of CD-31 in POA processed tissue) as well as residual detergent. In these methods, after creating damage to the vascular network, detergent solution would likely pool in regions, much the way blood did in OA and even re-endothelialized tissue, and would remain there despite rinsing with buffer. Alternatively the OA process allows for flux and clearing throughout the entire tissue, enabling rinsing despite damage that occurred to the vascular network.

Further experiments investigating the dynamics between cells, vascular patency, and physiological performance will need to be performed to optimize the various parameters to the end goal. We have laid the foundation establishing a connection between vascular patency *in vitro* and a potential improved vascular function.

Chapter 6: Conclusions and Future Directions

The purpose of this dissertation was to describe the motivation and development of a decellularized vascular scaffold. We outlined a method for effectively decellularizing lung tissue with a series of chemical detergents, while retaining most of the native architecture and patency of the vascular network down to the capillary scale. Such a scaffold was able to support cellular growth via injection loading and perfusion culture for three days—which in turn allowed cells to form capillary meshes and recover the vascular patency of the tissue.

The optimized acellular method was compared against two other decell methods. The first was taken from a method to decellularize heart tissue. The second was a method that utilized the detergents from the optimized acellular method, but delivered them in a perfusion system. Following decellularization, each tissue was examined on its ability to remove cellular components while retaining the architecture of native lung—particularly as it pertains to its vascular network. Standard characterization methods including histology, DNA concentration, and immunohistochemistry failed to elucidate significant differences in the efficacy of the decell methods. Functionality-based characterization using vascular corrosion casting was necessary to demonstrate the superiority of the optimized acellular method over the others tested. Qualitative electron micrographs depicted capillary-like structures that were not present in the corrosion casts of the other methods. Quantitative analysis of the electron micrographs was used to determine how much resin leaked out of the vascular networks in the form of spherical extravasations. Counting the total extravasational volume demonstrated the superiority of the optimized acellular method over the other two decellularization methods chosen, and highlighted the importance of functional characterization when evaluating decellularization protocols.

Re-endothelialization of the vascular network remaining in OA scaffolds was investigated by first determining the proper injection concentrations needed to attain uniform cellular distribution, then evaluating the vascular patency using qVCC analysis. An injection protocol was established that allowed for consistent loading and uniform distribution of cells into the vasculature of the OA scaffolds. After 60 hours of applied shear stress, the vascular patency proved to be improved when compared to barren OA scaffolds. The capillary-like structures that were present in the decellularized scaffolds were restored to resemble actual capillary structures once human dermal endothelial microvascular cells were added. The re-endothelialization also decreased the amount of extravasations and total extravasational volume. Following perfusion with whole blood, this improved vascular patency enhanced the ability to clear blood following perfusion with PBS, compared to barren scaffolds alone. Although some pooling of blood in the re-endothelialized construct was still observed, a correlation between improved vascular patency upon re-endothelialization and ability to perfuse and clear blood can be established. What needs to be determined is what significance the improved vascular patency will have on subsequent scaffold performance when implanted *in vivo*. The ultimate goal was to create a tissue engineering construct that could be potentially anastomosed to the host vasculature to allow for rapid perfusion to the entirety of the construct, in this regard the performance will be directly related the ability for the construct to facilitate blood flow without hemorrhaging. A hemorrhagic area would inevitably lead to poor nutrient transport and likely cell death in that area. A detailed study that looks at *in vivo* vascular performance would be necessary to draw the appropriate connections between vascular patency *in vitro* and subsequent performance—enabling the tailoring of future constructs to be properly optimized *in vitro*.

Further work needs to be performed to improve the vasculature of re-endothelialized scaffolds. Although we demonstrated regions of tissue that could be cleared following perfusion with blood, there were still regions of the scaffold that failed to clear. A more detailed investigation on the re-endothelialization process specific to the number of cells needed to effectively reconstitute the scaffold should be performed. Following optimized re-endothelialization, the next step to creating a relevant tissue engineering construct will be to observe the ability for the construct to support tissue-specific cells. Creating a patent vascular network will allow for the efficient flux of nutrients throughout the tissue, what needs to be understood is what happens to the cells in the remainder of the ECM not comprising vascular networks. Future studies could include implanting different cell populations into the bronchial space, allowing for additional repopulation of the scaffold prior to implantation *in vivo*.

Creating a co-culture system to support tissue-specific cells could be established using our re-endothelialized scaffold. Various researchers have used culture systems to support adult stem cells in a tissue-specific manner by tuning the modulus of the substrate in 2D [141] and 3D [142, 143]. Along these lines, the capacity to surround the vascular space created following re-endothelialization with a hydrogel of a specific modulus could be performed.

Using a hydrogel with a modulus that supports MSC differentiation toward adipose tissue could be a potential therapy for partial mastectomy healing. Scaffolds implanted in regions of adipose tissue experience greater vascularization than subcutaneous regions [144]. Included in the appendix section of this dissertation are images of sectioned explanted OA scaffolds following four weeks subcutaneous implantation. These images contain high positive staining for CD-31, demonstrating abundant vascular ingrowth. Such results may point to the ability of this scaffold to support vascularization without the need for anastomosis—again suggesting adipose implantation could lead to vascular ingrowth and support of MSCs comprising the majority of the tissue. Preliminary work on this project could consist of implanting re-endothelialized scaffolds subcutaneously into the right flank of rats, to observe the relative vascularization found in decellularized scaffolds alone. Creating an OA scaffold-hydrogel combination could also be performed preliminarily to observe the ability to support the viability of MSCs alone, or MSCs in a re-endothelialized scaffold. Researchers have demonstrated the ability to re-endothelialize decellularized lung tissue using the bronchial space instead of vascular space [145, 146]. Following re-endothelialization using our system, a second cell type or gel could easily be delivered by injecting the bronchus. This would allow for a controlled filling of the remaining space within the OA scaffold.

The majority of literature describing tuning PEG matrix stiffness to direct stem cell differentiation has been performed to isolate the effect stiffness has on cells without the influence of biological factors. In a concurrent project devised with the aid of funding from the venture capital group Remeditex, we have demonstrated the ability to create injectable gels from reconstituted decellularized matrix. Following the decellularization process, we are able to regel the ECM after mechanical and enzymatic degradation. The stiffness of this injectable ECM hydrogel is tunable depending on the solution used to regel (Appendix). A tissue engineering scaffold could potentially be created using the re-endothelialized matrix along with regelled ECM—specific to a particular tissue, and having an elastic modulus that could better support cells in that region.

Although the primary focus of this research has been to create a tissue engineering construct, other potential applications have presented themselves through the work performed here, as well as through interactions with other researchers and other literature. The composition of the scaffold used here is biomimetic, both spatially and chemically. With such considerations in place, the scaffold presents itself as a potential bioreactor system to investigate cellular phenomena, and drug-cell interactions. The effect that architecture might have on stem cell differentiation is one possible investigation. More research is being published focusing on the composition of the extracellular matrix on stem cell differentiation and "renewal," [147, 148] and the use of this scaffold would add to this field of investigation.

Problems finding an *in vitro* system to monitor effects of drugs on cells are in part due to the simplicity of systems *in vitro* opposed to the complexity of systems *in vivo*. With increasing research demonstrating the difference between cellular fate in 2D and 3D, it would make sense that the 3D environment plays an important role in the determination of cell fate—which would in turn affect drug response. Although this system would be extremely low-throughput, it nevertheless could be a helpful late stage *in vitro* tool that allows for greater control than *in vivo* models. Although this system has been used solely on the left lung lobe, the entire cardiovascular system could be easily decellularized, with little fear of excessive damage to the extracellular matrix based on the decellularization of 1 mm thick sections of lung being equivalent to 5 mm thick sections.

In conclusion, we created a decellularized scaffold that included a patent vascular network confirmed by augmenting standard characterization methods with the functional characterization. This decellularized scaffold was immune-tolerated and supported cellular growth of endothelial cells while implanted. The scaffold allowed for perfusion-based culture of endothelial cells—which imparted an improved vascular patency to the scaffold. We also applied a novel imaging modality that allowed us to monitor the loading of cells in a complex manner—enabling optimization that likely could not have occurred otherwise. Although not functionally relevant at this time, we propose this scaffold as a promising system for tissue regeneration, cell culture, and pharmacology.

Appendix A: Left Lung Isolation Protocol

Procedure:

1. Remove the esophagus from the dorsal side
2. Transect lymph tissue and descending aorta in between the esophagus and the left lung
3. Flip lung over to expose the ventral side
4. Completely remove the thymus
5. Clear lymph tissue above and around the aortic arch, until it becomes an impediment
6. Transect the aorta as close to the heart as possible—lift the tissue and cut the vessel free from connective tissue
7. Clear away lymph tissue to expose the right pulmonary artery distal to the bifurcation
8. Transect the right pulmonary artery as close to the right lung as possible—again, lift the tissue and cut the vessel free from connective tissue
9. Transect the trachea distal to the bifurcation
10. Transect the pulmonary artery as close to the heart as possible—lift up and cut to free the vessel, then fold the vessel over the left lung
11. Separate the left lung from the heart to expose the pulmonary veins (brownish in color), then transect them
12. Remove any connective tissue to free the left lung from the heart
13. Finish by removing excess fat and lymph tissue

The artery should be underneath the trachea, which is underneath the vein

Appendix B: Hematoxylin and Eosin Staining

Solutions:
<u>Eosin-Y</u>
100 ml 1% eosin solution
300 ml EtOH
2 ml acetic acid added just prior to use

<u>Hematoxylin</u>

<u>Scott solution</u>
10 g Magnesium sulfate
2 g Sodium bicarbonate
1000 ml Tap water

<u>Xylenes</u>

<u>Procedure</u>: (Frozen Slides)

1. Thaw slides
2. Rinse with water
    a. Hematoxylin for 2 min
    b. Tap water 2 changes 5 dips
    c. Scott solution dip until blue
    d. Tap water 2 changes 10 dips
    e. Eosin 15 dips
    f. 95% EtOH 10-15 dips
    g. 100% EtOH 10-15 dips
    h. 100% xylene 3 changes 10-15 dips
3. Permount and mount coverslip
4. Dry and image

Appendix C: Vascular Corrosion Casting Protocol

Materials:
Mercox II CL-2R
40% Benzoyl peroxide
Syringe pump with appropriate tubing
Modified 21Ga cannula (silicon rubber bead added)
Suture

Procedure: Casting

1. Using stereoscope, insert modified cannula (needle removed) into the pulmonary artery of the left lung—note: inject the cannula with PBS prior to insertion
2. Use chromic suture to tie a knot around the pulmonary artery—note: fold the right pulmonary artery such that the knot ties off the branching vessel as well
3. Attach the cannula to a luer plug attachment on tubing—note: tubing should be filled with PBS
4. Without creating bubbles, carefully mix Mercox II resin with 40% benzoyl peroxide (0.2 g catalyst/10 mL resin) and draw into a syringe while in the chemical hood
5. Attach tubing to syringe and perfuse tissue with the resin at a rate of 2 mL/min
6. Allow polymerization to occur in the hood for 10 min then cut cannula off the tissue and place the lung into a 15 mL conical tube filled with water
7. Place the conical tube in a water bath at 55-65°C for 1-2 days

Procedure: Tissue maceration

1. Place tissue in 25% KOH and place on a plate-shaker for 3-10 days
2. Every two days use water bath to help clear tissue, and change KOH solution
3. Place tissue in desiccator for SEM prep

Use glass in all resin polymerization steps. Once polymerized, the plastic can be easily removed. Once polymerized, the cast is no longer a health concern.

Appendix D: HPLC Analysis

HPLC Analysis of OA Decellularized Tissue

Another method used to characterize the biochemical composition of a particular material is high-performance liquid chromatography (HPLC). OA Processed lungs were degraded by flash-freezing, then grinding with a mortar and pestle. Enzymatic degradation of proteins was achieved by using pepsin at a pH of 2, and then neutralized after degradation was complete. Samples were electrophoresed on a 4-20% precast polyacrylamide gel. A trypsin-in-gel sample digestion (20 µL/sample) protocol was used before extraction with 5% formic acid in HPLC water. Samples were then processed using mass spectrometry HPLC in the Core Facility in ICMB.

HPLC Analysis Confirms Qualitative Composition of ECM Following OA Decellularization

Protein and tissue composition following decellularization was compared to fresh tissue. Although quantitative compared to the baseline sample, the actual protein concentrations obtained could not be absolutely quantified, only relatively quantified. All decell methods had similar relative distributions of proteins, which were consistent with fresh lung tissue (**Table, Figure**).

In lung decellularized using the OA procedure, fibrillin-1 comprised the majority of protein left in the ECM with 88 spectrum counts. This is not surprising based on the high amount of elasticity exhibited by both fresh lung as well as the decellularized scaffolds. With 41 spectrum counts, the next most prominent protein was laminin subunit β2, a common component of vascular smooth muscle ECM. The next most abundant protein, with 28 spectrum counts, was laminin subunit α5, a major component of basement membranes which has a high affinity with integrin α3β1. This was followed by the interstitial matrix protein collagen type VI at 24 spectrum counts. The most prominent proteins were by far fibrillin followed by various laminin subunits. Only two collagens featured prominently, collagen type VI and collagen type IV(α2), at 24 and 14 spectrum counts respectively. Other proteins present included collagen type I, elastin, fibronectin and nidogen. In summary, 41% of the proteins found belonged to laminin, 34% to fibrillin, 21% to collagen, 2% to elastin, and 1% to fibronectin.

HPLC analysis of our decellularized tissue allowed for the presence of a vast array of proteins to be observed. Although this method is not purely quantitative, it did allow for relative distributions of proteins within the different experimental groups to be compared. Following decellularization using the OA procedure, the majority of proteins identified were fibrillin-1, followed by various laminins. Fibrillin-1 is a glycoprotein that is responsible for forming microfibrils that surround elastin in the ECM. Given the high degree of elasticity in lung a high presence of fibrillin-1 is unsurprising. Laminin subunit β2 is a component of laminin-9, an endothelial cell basement membrane [61]. This laminin plays a role in endothelial cells stabilization [61]. Laminin subunit α5 is commonly found in laminin-5, laminin-10 (adult and vascular basement membranes), and laminin-11 (endothelial cell basement membrane) [61]. This subunit has a high affinity for the α3β1 integrin—upregulation of this binding has been shown to drive stabilization of the endothelium, ceasing proliferation and migration of endothelial cells [61]. The most prevalent collagen fragment found was collagen VI(α3). Collagen VI has significant interactions regarding endothelial cells. This interstitial protein helps organize ECM components through its binding of collagen types I, IV, and VIII [61]. Not all proteins were involved solely in stabilization of endothelium. Some collagen type IV was present (sixth highest protein count). Although this accessory protein of basement membrane assembly helps stabilize the basement matrix under stress, it is also involved in endothelial cell tube formation [61]. The presence of these major components tends to point at the preservation of basal membranes upon decellularization, with less interstitial proteins and less fibronectin and collagens. An interesting component present was nidogen-1, an accessory component to basement matrix assembly that also enhances endothelial tube formation [61]. HPLC analysis allowed for a wide selection of ECM proteins to be observed, however the presence of these proteins could only offer the idea that this scaffold could support endothelial cell fate.

HPLC Protein Analysis of Lung Tissue Following OA Decellularization

Proteins	Spectrum Counts (%) OA
Collagen Type I (α1)	3.1
Collagen Type II (α1)	1.2
Collagen Type IV(α2)	5.4
Collagen Type VI (α1)	1.5
Collagen type VI (α2)	0.8
Collagen Type VI (α3)	9.2
Total collagen	***21.2***
Elastin (iso 2)	1.9
Fibrillin-1	34.0
Fibronectin (iso 2)	1.2
Laminin (α5)	10.8
Laminin (β2)	15.8
Laminin (β3)	3.9
Laminin (γ1)	8.1
Laminin (γ2)	2.3
Total Laminin	***40.9***
Nidogen-1	0.8

HPLC analysis reveals conservation of proteins following decellularization. OA tissue contained a high level of basal membrane proteins and important interstitial proteins for endothelial cell fate.

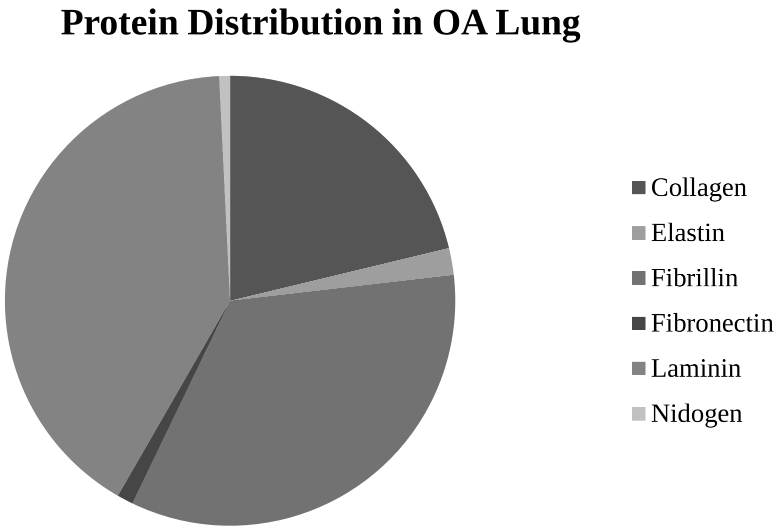

Number of spectrum counts for various proteins in lung following OA processing. HPLC analysis reveals a majority of fibrillin along with laminin and some collagens.

HPLC Protocol

Adapted from ICMB Core Facilities

This protocol was developed for 2D gel spots, ~100ng, using Dilution A of trypsin for silver, sypro ruby or faint Coomassie stained bands. If Coomassie stained spots at ug levels (medium to dark) are being digested, use Dilution B for trypsin aliquots.

Be ultraclean in all steps prior Day 3 step 1. If any keratin from dust or skin gets into the sample from the gel, cutting surface, pipette tips, tubes or digestion buffer, it will show up in the mass spectra and swamp weaker signals from the protein. Use tubes and tips that have not been exposed to ungloved hands. If possible work in the hood or a clean bench and filter the solutions, keep all the materials in an area dedicated to in-gel digestion. Wear lab coat and keep hair covered and held back.

<u>Solutions</u>:

1. Destain (400uL/sample)
    - 50% Methanol, 5% Acetic Acid in HPLC water
2. Trypsin (20uL/sample)
    - Add 160uL of Trypsin buffer to Trypsin stock solution tube (40uL of 0.5ug/uL). Then make aliquots of 20uL (2ug of Trypsin) and store in the freezer.
    - Prepare a fresh solution from aliquot before use.
    - Dilution A: 180uL of 50mM Ammonium Bicarbonate to each vial of 2ug (Promega) sequencing grade Trypsin. (Final concentration: 10ug/mL = 10ng/uL). 200 uL per vial
3. Acetonitrile (600uL/sample)
4. 10mM DTT (100uL/sample)

  - Prepare a fresh solution before use.
  - 1.54mg of DTT in 1mL of 100mM Ammonium Bicarbonate
5. 50mM Iodoacetamide (100uL/sample)
  - Prepare a fresh solution before use.
  - 10mg of Iodoacetamide in 1mL 100mM Ammonium Bicarbonate
6. 100mM Ammonium Bicarbonate (200uL/sample)
  - 0.79g of Ammonium Bicarbonate in 100mL of HPLC Water (Filtered with 0.2um syringe filter)

   Note: Also add amount needed to make 50mM Ammonium Bicarbonate, 10 mM DTT and 50mM Iodoacetamide solutions.
7. 50mM Ammonium Bicarbonate (20uL/sample)
  - Dilution 1:1 of HPLC Water:100mM Ammonium Bicarbonate

   Note: Also add amount needed to make Trypsin solution.
8. Extraction buffer 1 (20uL/sample)
  - 5% Formic Acid in HPLC Water
9. Extraction buffer 2 (20uL/sample)
  - -1:2 (v:v) 5% Formic Acid in HPLC Water : Acetonitrile

Procedure: Sample Preparation

1. Grind decellularized lungs into a coarse powder using a mortar and pestle and liquid nitrogen
2. Lyophilize and keep frozen at -20°C until further use
3. Digest milled samples with pepsin in 0.1M HCl at a concentration of 10 mg ECM per 1 mL HCl. Pepsin (Sigma, St. Louis, MO) was used at a concentration of 1 mg per mL. The ECM powder was digested for 65 hours and neutralized to a pH of 7.4 using 1 M NaOH (1 ml = 10 of original digest volume) and 10X PBS (1 ml =10 ml of final neutralized volume)
4. Electrophorese solubilized ECM lung samples on a 4–20% precast linear gradient polyacrylamide under reducing conditions (5% 2-mercaptoethanol) for 20 minutes

Procedure: Sample Digestion

1. Cut the spot and chop it with a clean razor blade into 1mm^3 pieces. If Coomassie gel is used, cut spot as close as possible to minimize gel volume.
2. Pick the gel pieces with the razor or with a wide bore P1000 tip or P1000 tip with end cut off and put them in a 1.5mL microfuge tube
3. Add 400uL of Destain solution. Spots can be left in Destain solution indefinitely at 4^{o}C.

Day 2

1. Remove and discard Destain solution.
2. Add 200uL of Acetonitrile to dehydrate. Gel pieces should turn white. If they do not, repeat Acetonitrile treatment.
3. Remove and discard Acetonitrile solution.
4. Air dry at room temperature until gel pieces no longer stick to the tube or each other.
5. Add 100uL of 10mM DTT solution to reduce the gel.
6. Incubate for 30min at room temperature.
7. Remove and discard DTT solution.
8. Add 100uL 50mM of Iodoacetamide solution to alkylate the gel
9. Incubate for 30min at room temperature.
10. Remove and discard Iodoacetamide solution.
11. Wash with 200uL of 100mM Ammonium Bicarbonate solution.
12. Incubate for 10min at room temperature.
13. Remove and discard Ammonium Bicarbonate solution.
14. Wash two times with 200uL of Acetonitrile solution to dehydrate the gel. Incubate each time for 5min at room temperature. Gel should turn white.
15. Air dry at room temperature until gel pieces no longer stick to the tube or each other.
16. Prepare Trypsin solution (See solution preparation for recipe). Choose either Dilution A or B based on amount of protein in gel band.
17. Add 20uL of Trypsin solution to each spot (sample), keep cold until gel is rehydrated. If gel is not fully hydrated, add 20uL of Trypsin solution again.
18. Incubate in ice for a few minutes.
19. Add 20uL of 50mM Ammonium Bicarbonate solution to each spot (sample).

Incubate overnight at 37°C.

Day 3

(microfuge briefly before each solution transfer step)

1. Add 20uL of Extraction Buffer 1 to each spot (sample) then vortex and centrifuge it.
2. Transfer liquid to a new 0.5mL microfuge tube.
3. Add 20uL of Extraction Buffer 2 to each spot (sample) then vortex and centrifuge it.

4. Transfer liquid to same new tubes as step 2.
5. Store samples at 4^{o}C if submitting directly to Analytical Core or at -20^{o}C if leaving for more than 3-4 days.

Appendix E: CD-31 Stained Explants

Following subcutaneous implantation for four weeks, OA explants were sectioned and stained for presence of macrophages. Unrelated to the immunogenicity experiment, these sections were also stained with CD-31 (green) and laminin (red) to visualize any presence of vascularization in allografts (top) and isografts (bottom). These images demonstrate that vascularization occurred within the entirety of the scaffold—which was extensively remodeled. Scale bar = 200 microns.

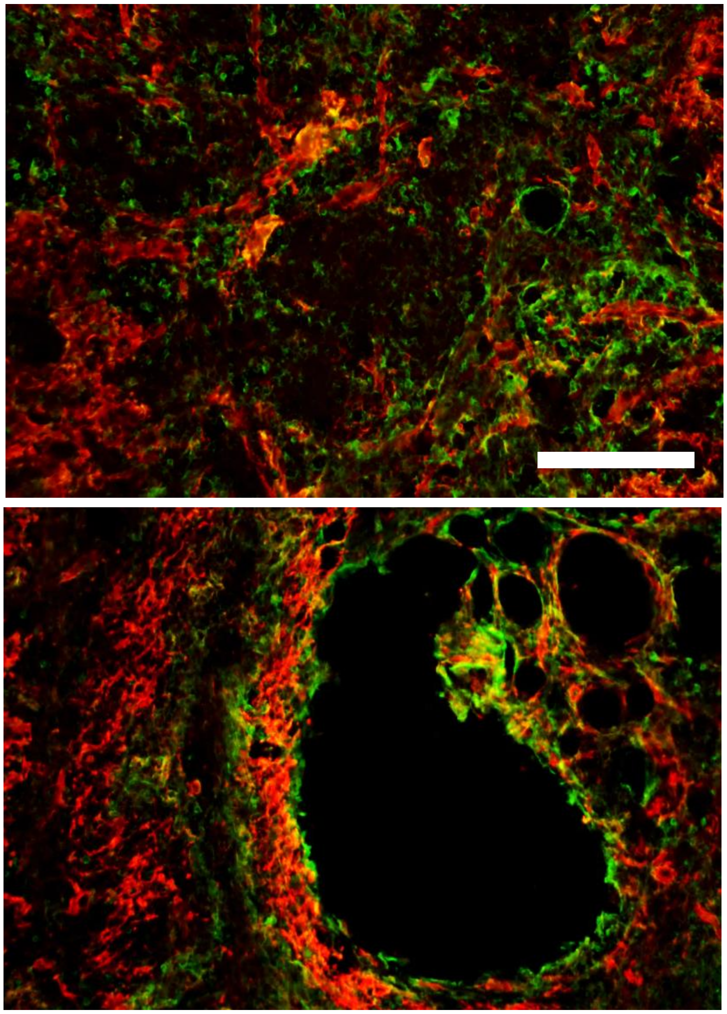

Appendix F: Regelled Decellularized ECM

Lung ECM decellularized using the OA procedure was subsequently regelled. The end product is an injectable gel that crosslinks at physiological temperature. This technique could potentially be used in combination with our decellularized vascular tissue to fill the remaining space. This tunable gel could potentially support adult or immature stem cells and direct differentiation using biochemical and mechanical cues.

Procedure: Sample Preparation

1. Grind decellularized lungs into a coarse powder using a mortar and pestle and liquid nitrogen
2. Lyophilize and keep frozen at -20°C until further use
3. Digest milled samples with pepsin in 0.1M HCl at a concentration of 10 mg ECM per 1 mL HCl. Pepsin (Sigma, St. Louis, MO) was used at a concentration of 1 mg per mL. The ECM powder was digested for 65 hours and neutralized to a pH of 7.4 using 1 M NaOH (1 ml = 10 of original digest volume) and 10X PBS (1 ml =10 ml of final neutralized volume)
4. Place in 2 mm gel mold for crosslinking at 37C

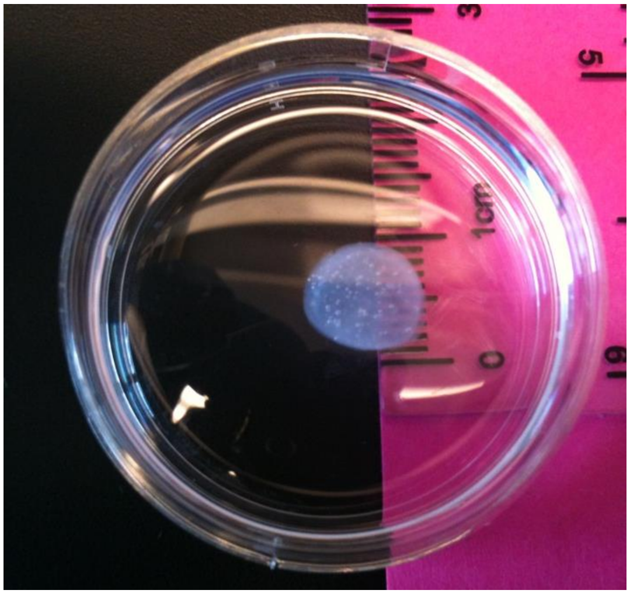

References

1. *Organ Procurement and Transplantation Network (OPTN) Data*. 2010.
2. Atala, A., et al., *Tissue-engineered autologous bladders for patients needing cystoplasty.* Lancet, 2006. **367**(9518): p. 1241-1246.
3. Brittberg, M., et al., *Treatment of Deep Cartilage Defects in the Knee with Autologous Chondrocyte Transplantation.* New England Journal of Medicine, 1994. **331**(14): p. 889-895.
4. Kirsner, R.S., V. Falanga, and W.H. Eaglstein, *The development of bioengineered skin.* Trends in Biotechnology, 1998. **16**(6): p. 246-249.
5. Johnson, P.C., et al., *Strategic directions in tissue engineering.* Tissue Engineering, 2007. **13**(12): p. 2827-+.
6. Carmeliet, P. and R.K. Jain, *Angiogenesis in cancer and other diseases.* Nature, 2000. **407**: p. 249-257.
7. Eliot R. Clark, E.L.C., *Microscopic observations on the extra-endothelial cells of living mammalian blood vessels.* American Journal of Anatomy, 1940. **66**(1): p. 1-49.
8. Folkman, J., et al., *Tumor Angiogenesis - Therapeutic Implications.* New England Journal of Medicine, 1971. **285**(21): p. 1182-&.
9. Kruyt, M.C., et al., *Optimization of bone tissue engineering in goats: A peroperative seeding method using cryopreserved cells and localized bone formation in calcium phosphate scaffolds.* Transplantation, 2004. **77**(3): p. 359-365.
10. Ishaug-Riley, S.L., et al., *Three-dimensional culture of rat calvarial osteoblasts in porous biodegradable polymers.* Biomaterials, 1998. **19**(15): p. 1405-1412.
11. Suzuki, K., et al., *Number and volume of islets transplanted in immunobarrier devices.* Cell Transplantation, 1998. **7**(1): p. 47-52.
12. Griffith, C.K., et al., *Diffusion limits of an in vitro thick prevascularized tissue.* Tissue Engineering, 2005. **11**(1-2): p. 257-266.
13. Griffith, L.G. and G. Naughton, *Tissue engineering - Current challenges and expanding opportunities.* Science, 2002. **295**(5557): p. 1009-+.
14. Rivron, N.C., et al., *Engineering vascularised tissues in vitro.* European Cells & Materials, 2008. **15**: p. 27-40.
15. Malda, J., et al., *Oxygen gradients in tissue-engineered PEGT/PBT cartilaginous constructs: Measurement and modeling.* Biotechnology and Bioengineering, 2004. **86**(1): p. 9-18.
16. Zisch, A.H., M.P. Lutolf, and J.A. Hubbell, *Biopolymeric delivery matrices for angiogenic growth factors.* Cardiovascular Pathology, 2003. **12**(6): p. 295-310.
17. Rouwkema, J., N.C. Rivron, and C.A. van Blitterswijk, *Vascularization in tissue engineering.* Trends in Biotechnology, 2008. **26**(8): p. 434-441.

18. Mertsching, H., et al., *Generation and Transplantation of an Autologous Vascularized Bioartificial Human Tissue.* Transplantation, 2009. **88**(2): p. 203-210.
19. Mertsching, H., et al., *Engineering of a vascularized scaffold for artificial tissue and organ generation.* Biomaterials, 2005. **26**(33): p. 6610-6617.
20. Schultheiss, D., et al., *Biological vascularized matrix for bladder tissue engineering: Matrix preparation, reseeding technique and short-term implantation in a porcine model.* Journal of Urology, 2005. **173**(1): p. 276-280.
21. Hirschi, K.K., et al., *Vascular assembly in natural and engineered tissues*, in *Reparative Medicine: Growing Tissues and Organs*, J.D. Sipe, C.A. Kelley, and L.A. McNicol, Editors. 2002, New York Acad Sciences: New York. p. 223-242.
22. Jain, R.K., et al., *Engineering vascularized tissue.* Nature Biotechnology, 2005. **23**(7): p. 821-823.
23. Carmeliet, P., *Mechanisms of angiogenesis and arteriogenesis.* Nature Medicine, 2000. **6**: p. 389-395.
24. Chen, R.R., et al., *Spatio-temporal VEGF and PDGF delivery patterns blood vessel formation and maturation.* Pharmaceutical Research, 2007. **24**(2): p. 258-264.
25. Pola, R., et al., *The morphogen Sonic hedgehog is an indirect angiogenic agent upregulating two families of angiogenic growth factors.* Nature Medicine, 2001. **7**(6): p. 706-711.
26. Richardson, T.P., et al., *Polymeric system for dual growth factor delivery.* Nature Biotechnology, 2001. **19**(11): p. 1029-1034.
27. Langer, R. and J.P. Vacanti, *TISSUE ENGINEERING.* Science, 1993. **260**(5110): p. 920-926.
28. Druecke, D., et al., *Neovascularization of poly(ether ester) block-copolymer scaffolds in vivo: Long-term investigations using intravital fluorescent microscopy.* Journal of Biomedical Materials Research Part A, 2004. **68A**(1): p. 10-18.
29. Karageorgiou, V. and D. Kaplan, *Porosity of 3D biornaterial scaffolds and osteogenesis.* Biomaterials, 2005. **26**(27): p. 5474-5491.
30. Yang, S.F., et al., *The design of scaffolds for use in tissue engineering. Part 1. Traditional factors.* Tissue Engineering, 2001. **7**(6): p. 679-689.
31. Cartmell, S.H., et al., *Effects of medium perfusion rate on cell-seeded three-dimensional bone constructs in vitro.* Tissue Engineering, 2003. **9**(6): p. 1197-1203.
32. Lovett, M., et al., *Vascularization Strategies for Tissue Engineering.* Tissue Engineering Part B-Reviews, 2009. **15**(3): p. 353-370.
33. Ott, M.J. and B.J. Ballermann, *SHEAR STRESS-CONDITIONED, ENDOTHELIAL CELL-SEEDED VASCULAR GRAFTS - IMPROVED CELL ADHERENCE IN RESPONSE TO IN-VITRO SHEAR-STRESS.* Surgery, 1995. **117**(3): p. 334-339.

34. Sato, M., et al., *Local mechanical properties measured by atomic force microscopy for cultured bovine endothelial cells exposed to shear stress.* Journal of Biomechanics, 2000. **33**(1): p. 127-135.
35. Inoguchi, H., et al., *The effect of gradually graded shear stress on the morphological integrity of a huvec-seeded compliant small-diameter vascular graft.* Biomaterials, 2007. **28**(3): p. 486-495.
36. Frangos, J.A., et al., *FLOW EFFECTS ON PROSTACYCLIN PRODUCTION BY CULTURED HUMAN-ENDOTHELIAL CELLS.* Science, 1985. **227**(4693): p. 1477-1479.
37. Duffy, D.C., et al., *Rapid prototyping of microfluidic systems in poly(dimethylsiloxane).* Analytical Chemistry, 1998. **70**(23): p. 4974-4984.
38. Kane, R.S., et al., *Patterning proteins and cells using soft lithography.* Biomaterials, 1999. **20**(23-24): p. 2363-2376.
39. Borenstein, J.T., et al., *Microfabrication technology for vascularized tissue engineering.* Biomedical Microdevices, 2002. **4**(3): p. 167-175.
40. Kaihara, S., et al., *Silicon micromachining to tissue engineer branched vascular channels for liver fabrication.* Tissue Engineering, 2000. **6**(2): p. 105-117.
41. Borenstein, J.T., et al., *Functional endothelialized microvascular networks with circular cross-sections in a tissue culture substrate.* Biomedical Microdevices, 2010. **12**(1): p. 71-79.
42. King, K.R., et al., *Biodegradable microfluidics.* Advanced Materials, 2004. **16**(22): p. 2007-+.
43. Fidkowski, C., et al., *Endothelialized microvasculature based on a biodegradable elastomer.* Tissue Engineering, 2005. **11**(1-2): p. 302-309.
44. Khademhosseini, A., et al., *Microscale technologies for tissue engineering and biology.* Proceedings of the National Academy of Sciences of the United States of America, 2006. **103**(8): p. 2480-2487.
45. Green, J.V., et al., *Effect of channel geometry on cell adhesion in microfluidic devices.* Lab on a Chip, 2009. **9**(5): p. 677-685.
46. Lu, H., et al., *Microfluidic shear devices for quantitative analysis of cell adhesion.* Analytical Chemistry, 2004. **76**(18): p. 5257-5264.
47. Kim, S.S., et al., *Survival and function of hepatocytes on a novel three-dimensional synthetic biodegradable polymer scaffold with an intrinsic network of channels.* Annals of Surgery, 1998. **228**(1): p. 8-13.
48. Zeltinger, J., et al., *Effect of pore size and void fraction on cellular adhesion, proliferation, and matrix deposition.* Tissue Engineering, 2001. **7**(5): p. 557-572.
49. Leong, K.F., C.M. Cheah, and C.K. Chua, *Solid freeform fabrication of three-dimensional scaffolds for engineering replacement tissues and organs.* Biomaterials, 2003. **24**(13): p. 2363-2378.
50. Erol, O.O. and M. Spira, *NEW CAPILLARY BED FORMATION WITH A SURGICALLY CONSTRUCTED ARTERIOVENOUS-FISTULA.* Plastic and Reconstructive Surgery, 1980. **66**(1): p. 109-115.

51. Tanaka, Y., et al., *Generation of an autologous tissue (matrix) flap by combining an arteriovenous shunt loop with artificial skin in rats: preliminary report.* British Journal of Plastic Surgery, 2000. **53**(1): p. 51-57.
52. Kneser, U., et al., *Engineering of vascularized transplantable bone tissues: Induction of axial vascularization in an osteoconductive matrix using an arteriovenous loop.* Tissue Engineering, 2006. **12**(7): p. 1721-1731.
53. Bach, A.D., et al., *A new approach to tissue engineering of vascularized skeletal muscle.* Journal of Cellular and Molecular Medicine, 2006. **10**(3): p. 716-726.
54. Hofer, S.O.P., et al., *Increasing the volume of vascularized tissue formation in engineered constructs: An experimental study in rats.* Plastic and Reconstructive Surgery, 2003. **111**(3): p. 1186-1192.
55. Beier, J.P., et al., *DE NOVO GENERATION OF AXIALLY VASCULARIZED TISSUE IN A LARGE ANIMAL MODEL.* Microsurgery, 2009. **29**(1): p. 42-51.
56. Tremblay, P.L., et al., *Inosculation of tissue-engineered capillaries with the host's vasculature in a reconstructed skin transplanted on mice.* American Journal of Transplantation, 2005. **5**(5): p. 1002-1010.
57. Black, A.F., et al., *In vitro reconstruction of a human capillary-like network in a tissue-engineered skin equivalent.* Faseb Journal, 1998. **12**(13): p. 1331-1340.
58. Levenberg, S., et al., *Engineering vascularized skeletal muscle tissue.* Nature Biotechnology, 2005. **23**(7): p. 879-884.
59. Caspi, O., et al., *Tissue engineering of vascularized cardiac muscle from human embryonic stem cells.* Circulation Research, 2007. **100**(2): p. 263-272.
60. Unger, R.E., et al., *Tissue-like self-assembly in cocultures of endothelial cells and osteoblasts and the formation of microcapillary-like structures on three-dimensional porous biomaterials.* Biomaterials, 2007. **28**(27): p. 3965-3976.
61. Davis, G.E. and D.R. Senger, *Endothelial extracellular matrix - Biosynthesis, remodeling, and functions during vascular morphogenesis and neovessel stabilization.* Circulation Research, 2005. **97**(11): p. 1093-1107.
62. Senger, D.R., et al., *The alpha(1)beta(1) and alpha(2)beta(1) Integrins provide critical support for vascular endothelial growth factor signaling, endothelial cell migration, and tumor angiogenesis.* American Journal of Pathology, 2002. **160**(1): p. 195-204.
63. Bompais, H., et al., *Human endothelial cells derived from circulating progenitors display specific functional properties compared with mature vessel wall endothelial cells.* Blood, 2004. **103**(7): p. 2577-2584.
64. Drake, C.J. and C.D. Little, *VEGF and vascular fusion: Implications for normal and pathological vessels.* Journal of Histochemistry & Cytochemistry, 1999. **47**(11): p. 1351-1355.
65. Montesano, R., L. Orci, and P. Vassalli, *INVITRO RAPID ORGANIZATION OF ENDOTHELIAL-CELLS INTO CAPILLARY-LIKE NETWORKS IS PROMOTED BY COLLAGEN MATRICES.* Journal of Cell Biology, 1983. **97**(5): p. 1648-1652.
66. Davis, G.E. and C.W. Camarillo, *An alpha 2 beta 1 integrin-dependent pinocytic mechanism involving intracellular vacuole formation and coalescence regulates*

capillary lumen and tube formation in three-dimensional collagen matrix. Experimental Cell Research, 1996. **224**(1): p. 39-51.

67. Ingber, D.E. and J. Folkman, *HOW DOES EXTRACELLULAR-MATRIX CONTROL CAPILLARY MORPHOGENESIS.* Cell, 1989. **58**(5): p. 803-805.
68. Iuliano, D.J., S.S. Saavedra, and G.A. Truskey, *EFFECT OF THE CONFORMATION AND ORIENTATION OF ADSORBED FIBRONECTIN ON ENDOTHELIAL-CELL SPREADING AND THE STRENGTH OF ADHESION.* Journal of Biomedical Materials Research, 1993. **27**(8): p. 1103-1113.
69. Schmidt, C.E. and J.M. Baier, *Acellular vascular tissues: natural biomaterials for tissue repair and tissue engineering.* Biomaterials, 2000. **21**(22): p. 2215-2231.
70. Borschel, G.H., R.G. Dennis, and W.M. Kuzon, *Contractile skeletal muscle tissue-engineered on an acellular scaffold.* Plastic and Reconstructive Surgery, 2004. **113**(2): p. 595-602.
71. Merritt, E.K., et al., *Functional assessment of skeletal muscle regeneration utilizing homologous extracellular matrix as scaffolding.* Tissue Eng Part A, 2010. **16**(4): p. 1395-405.
72. Fawcett, J.W. and R.J. Keynes, *MUSCLE BASAL LAMINA - A NEW GRAFT MATERIAL FOR PERIPHERAL-NERVE REPAIR.* Journal of Neurosurgery, 1986. **65**(3): p. 354-363.
73. Hudson, T.W., S.Y. Liu, and C.E. Schmidt, *Engineering an improved acellular nerve graft via optimized chemical processing.* Tissue Engineering, 2004. **10**(9-10): p. 1346-1358.
74. Hudson, T.W., et al., *Optimized acellular nerve graft is immunologically tolerated and supports regeneration.* Tissue Engineering, 2004. **10**(11-12): p. 1641-1651.
75. Sondell, M., G. Lundborg, and M. Kanje, *Regeneration of the rat sciatic nerve into allografts made acellular through chemical extraction.* Brain Research, 1998. **795**(1-2): p. 44-54.
76. Ott, H.C., et al., *Perfusion-decellularized matrix: using nature's platform to engineer a bioartificial heart.* Nature Medicine, 2008. **14**(2): p. 213-221.
77. Lalka, S.G., et al., *Acellular vascular matrix: a natural endothelial cell substrate.* Ann Vasc Surg, 1989. **3**(2): p. 108-17.
78. Malone, J.M., et al., *DETERGENT-EXTRACTED SMALL-DIAMETER VASCULAR PROSTHESES.* Journal of Vascular Surgery, 1984. **1**(1): p. 181-191.
79. Kaushal, S., et al., *Functional small-diameter neovessels created using endothelial progenitor cells expanded ex vivo.* Nature Medicine, 2001. **7**(9): p. 1035-1040.
80. Lozito, T.P., et al., *Human Mesenchymal Stem Cells Express Vascular Cell Phenotypes Upon Interaction With Endothelial Cell Matrix.* Journal of Cellular Biochemistry, 2009. **107**(4): p. 714-722.
81. Lozito, T.P., et al., *Mesenchymal Stem Cell Modification of Endothelial Matrix Regulates Their Vascular Differentiation.* Journal of Cellular Biochemistry, 2009. **107**(4): p. 706-713.

82. Prevel, C.D., et al., *EXPERIMENTAL EVALUATION OF SMALL-INTESTINAL SUBMUCOSA AS A MICROVASCULAR GRAFT MATERIAL.* Microsurgery, 1994. **15**(8): p. 586-591.
83. Kawamoto, A. and D.W. Losordo, *Endothelial progenitor cells for cardiovascular regeneration.* Trends in Cardiovascular Medicine, 2008. **18**(1): p. 33-37.
84. Roncalli, J.G., et al., *Endothelial progenitor cells in regenerative medicine and cancer: a decade of research.* Trends in Biotechnology, 2008. **26**(5): p. 276-283.
85. Thomson, J.A., et al., *Embryonic stem cell lines derived from human blastocysts.* Science, 1998. **282**(5391): p. 1145-1147.
86. Pittenger, M.F., et al., *Multilineage potential of adult human mesenchymal stem cells.* Science, 1999. **284**(5411): p. 143-147.
87. Oswald, J., et al., *Mesenchymal stem cells can be differentiated into endothelial cells in vitro.* Stem Cells, 2004. **22**(3): p. 377-384.
88. Chen, L.W., et al., *Paracrine Factors of Mesenchymal Stem Cells Recruit Macrophages and Endothelial Lineage Cells and Enhance Wound Healing.* Plos One, 2008. **3**(4).
89. Jackson, K.A., et al., *Regeneration of ischemic cardiac muscle and vascular endothelium by adult stem cells.* Journal of Clinical Investigation, 2001. **107**(11): p. 1395-1402.
90. Kinnaird, T., et al., *Marrow-derived stromal cells express genes encoding a broad spectrum of arteriogenic cytokines and promote in vitro and in vivo arteriogenesis through paracrine mechanisms.* Circulation Research, 2004. **94**(5): p. 678-685.
91. Kinnaird, T., et al., *Local delivery of marrow-derived stromal cells augments collateral perfusion through paracrine mechanisms.* Circulation, 2004. **109**(12): p. 1543-1549.
92. Kocher, A.A., et al., *Neovascularization of ischemic myocardium by human bone-marrow-derived angioblasts prevents cardiomyocyte apoptosis, reduces remodeling and improves cardiac function.* Nature Medicine, 2001. **7**(4): p. 430-436.
93. Gnecchi, M., et al., *Paracrine Mechanisms in Adult Stem Cell Signaling and Therapy.* Circulation Research, 2008. **103**(11): p. 1204-1219.
94. Hung, S.C., et al., *Short-Term Exposure of Multipotent Stromal Cells to Low Oxygen Increases Their Expression of CX3CR1 and CXCR4 and Their Engraftment In Vivo.* Plos One, 2007. **2**(5).
95. Asahara, T., et al., *Isolation of putative progenitor endothelial cells for angiogenesis.* Science, 1997. **275**(5302): p. 964-967.
96. Urbich, C. and S. Dimmeler, *Endothelial progenitor cells - Characterization and role in vascular biology.* Circulation Research, 2004. **95**(4): p. 343-353.
97. Discher, D.E., D.J. Mooney, and P.W. Zandstra, *Growth Factors, Matrices, and Forces Combine and Control Stem Cells.* Science, 2009. **324**(5935): p. 1673-1677.

98. Discher, D.E., et al., *Matrix elasticity directs stem cell lineage specification.* Biophysical Journal, 2007: p. 32A-32A.

99. Pajerowski, J.D., et al., *Physical plasticity of the nucleus in stem cell differentiation.* Proceedings of the National Academy of Sciences of the United States of America, 2007. **104**: p. 15619-15624.

100. Wang, H., et al., *Shear stress induces endothelial differentiation from a murine embryonic mesenchymal progenitor cell line.* Arteriosclerosis Thrombosis and Vascular Biology, 2005. **25**(9): p. 1817-1823.

101. Yamamoto, K., et al., *Fluid shear stress induces differentiation of Flk-1-positive embryonic stem cells into vascular endothelial cells in vitro.* American Journal of Physiology-Heart and Circulatory Physiology, 2005. **288**(4): p. H1915-H1924.

102. Gannon, B., et al., *MUCOSAL MICROVASCULAR ARCHITECTURE OF THE FUNDUS AND BODY OF HUMAN STOMACH.* Gastroenterology, 1984. **86**(5): p. 866-875.

103. Raschke, M., W. Lierse, and H. Vanackeren, *MICROVASCULAR ARCHITECTURE OF THE MUCOSA OF THE GASTRIC CORPUS IN MAN.* Acta Anatomica, 1987. **130**(2): p. 185-190.

104. Gorczyca, J., et al., *Architecture of blood vessels in human fetal gastric corpus: a corrosion casting study.* Annals of Anatomy - Anatomischer Anzeiger, 1999. **181**(4): p. 353-358.

105. Zawilinski, J., et al., *Vascular system of the human spinal cord in the prenatal period: a dye injection and corrosion casting study.* Annals of Anatomy - Anatomischer Anzeiger, 2001. **183**(4): p. 331-340.

106. Westerweel, P.E., et al., *A study of neovascularization in the rat ischemic hindlimb using Araldite casting and Spalteholtz tissue clearing.* Cardiovascular Pathology, 2005. **14**(6): p. 294-297.

107. Mondy, W.L., et al., *Micro-CT of Corrosion Casts for Use in the Computer-Aided Design of Microvasculature.* Tissue Engineering Part C-Methods, 2009. **15**(4): p. 729-738.

108. Maina, J.N. and P. van Gils, *Morphometric characterization of the airway and vascular systems of the lung of the domestic pig, Sus scrofa: comparison of the airway, arterial and venous systems.* Comparative Biochemistry and Physiology a-Molecular and Integrative Physiology, 2001. **130**(4): p. 781-798.

109. Dickie, R., et al., *Three-dimensional visualization of microvessel architecture of whole-mount tissue by confocal microscopy.* Microvascular Research. **72**(1-2): p. 20-26.

110. Konerding, M.A., et al., *Evidence for characteristic vascular patterns in solid tumours: quantitative studies using corrosion casts.* British Journal of Cancer, 1999. **80**(5-6): p. 724-732.

111. Konerding, M.A., E. Fait, and A. Gaumann, *3D microvascular architecture of pre-cancerous lesions and invasive carcinomas of the colon.* British Journal of Cancer, 2001. **84**(10): p. 1354-1362.

112. Laurent, M., et al., *CONFOCAL SCANNING OPTICAL MICROSCOPY AND 3-DIMENSIONAL IMAGING.* Biology of the Cell, 1992. **76**(2): p. 113-124.
113. Koyanagi, I., C.H. Tator, and P.J. Lea, *Three-Dimensional Analysis of the Vascular System in the Rat Spinal Cord with Scanning Electron Microscopy of Vascular Corrosion Casts. Part 2: Acute Spinal Cord Injury.* Neurosurgery, 1993. **33**(2): p. 285-292.
114. *Guide for the Care and Use of Laboratory Animals*. 2011, Institue for Laboratory Animal Research, National Research Council of the National Academies: Washington D.C.
115. Ricles, L.M., et al., *Function of mesenchymal stem cells following loading of gold nanotracers.* International Journal of Nanomedicine, 2011. **6**: p. 407-416.
116. Mallidi, S., et al., *Molecular specific optoacoustic imaging with plasmonic nanoparticles.* Optics Express, 2007. **15**(11): p. 6583-6588.
117. Cebotari, S., et al., *Detergent decellularization of heart valves for tissue engineering: toxicological effects of residual detergents on human endothelial cells.* Artif Organs, 2010. **34**(3): p. 206-10.
118. Reynolds, J.A. and C. Tanford, *Binding of Dodecyl Sulfate to Proteins at High Binding Ratios. Possible Implications for the State of Proteins in Biological Membranes.* Proceedings of the National Academy of Sciences, 1970. **66**(3): p. 1002-1007.
119. Rieder, E., et al., *Decellularization protocols of porcine heart valves differ importantly in efficiency of cell removal and susceptibility of the matrix to recellularization with human vascular cells.* J Thorac Cardiovasc Surg, 2004. **127**(2): p. 399-405.
120. Ohtake, M., et al., *Three-dimensional structural changes in cerebral microvessels after transient focal cerebral ischemia in rats: Scanning electron microscopic study of corrosion casts.* Neuropathology, 2004. **24**(3): p. 219-227.
121. Bozzola, J.J.a.R., Lonnie Dee, *Electron Microscopy: Principles and Techniques for Biologists*. 2nd ed. 1999: Jones & Bartlett Publishers
122. Anselme, K., et al., *Tissue reaction to subcutaneous implantation of a collagen sponge. A histological, ultrastructural, and immunological study.* Journal of Biomedical Materials Research, 1990. **24**(6): p. 689-703.
123. Stark, O. and V. Kren, *5 CONGENIC RESISTANT LINES OF RATS DIFFERING AT RT H-1 LOCUS.* Transplantation, 1969. **8**(2): p. 200-&.
124. *Fischer 344 Data Sheet*, H. Laboratories, Editor. 2008.
125. Zhang, G., et al., *Vascular differentiation of bone marrow stem cells is directed by a tunable 3D matrix.* Acta Biomaterialia, 2010. ***in press***.
126. Nam, S.Y., et al., *In vivo Ultrasound and Photoacoustic Monitoring of Mesenchymal Stem Cells Labeled with Gold Nanotracers.* Plos One, 2012. **7**(5).
127. McMullan, D.M., F.L. Hanley, and R.K. Riemer, *A method for selectively limiting lumen diameter in corrosion casting.* Microvasc Res, 2004. **67**(3): p. 215-7.

128. Li, S.G., D.C. Randall, and D.R. Brown, *Roles of cardiac output and peripheral resistance in mediating blood pressure response to stress in rats.* Am J Physiol, 1998. **274**(4 Pt 2): p. R1065-9.

129. Smith, F.J. and G.A. Bennett, *The Pulmonary Arterial Pressure in Normal Albino Rats and the Effect Thereon of Epinephrine.* J Exp Med, 1934. **59**(2): p. 173-80.

130. Hess, P., M. Clozel, and J.P. Clozel, *Telemetry monitoring of pulmonary arterial pressure in freely moving rats.* Journal of Applied Physiology, 1996. **81**(2): p. 1027-1032.

131. Deten, A., H. Millar, and H.-G. Zimmer, *Catheterization of pulmonary artery in rats with an ultraminiature catheter pressure transducer.* American Journal of Physiology - Heart and Circulatory Physiology, 2003. **285**(5): p. H2212-H2217.

132. Kolettis, T., et al., *Characterisation of a rat model of pulmonary arterial hypertension.* Hellenic journal of cardiology : HJC = Hellenike kardiologike epitheorese, 2007. **48**(4): p. 206-10.

133. Sun, W.Q. and P. Leung, *Calorimetric study of extracellular tissue matrix degradation and instability after gamma irradiation.* Acta Biomater, 2008. **4**(4): p. 817-26.

134. Crapo, P.M., T.W. Gilbert, and S.F. Badylak, *An overview of tissue and whole organ decellularization processes.* Biomaterials, 2011. **32**(12): p. 3233-43.

135. Parenteau-Bareil, R., R. Gauvin, and F. Berthod, *Collagen-Based Biomaterials for Tissue Engineering Applications.* Materials, 2010. **3**(3): p. 1863-1887.

136. Brown, B., et al., *The basement membrane component of biologic scaffolds derived from extracellular matrix.* Tissue Eng, 2006. **12**(3): p. 519-26.

137. Qiu, Q.Q., et al., *Inactivation of bacterial spores and viruses in biological material using supercritical carbon dioxide with sterilant.* J Biomed Mater Res B Appl Biomater, 2009. **91**(2): p. 572-8.

138. Cho, Y.I. and K.R. Kensey, *Effects of the non-Newtonian viscosity of blood on flows in a diseased arterial vessel. Part 1: Steady flows.* Biorheology, 1991. **28**(3-4): p. 241-262.

139. Truskey, G.A., Yuan, F., Katz, D.F., *Transport phenomena in biological systems*. 1st ed. 2004, Upper Saddle River: Pearson/Prentice Hall.

140. Podgoreanu, M.V., et al., *Differential cardiac gene expression during cardiopulmonary bypass: Ischemia-independent upregulation of proinflammatory genes.* J Thorac Cardiovasc Surg, 2005. **130**(2): p. 330-339.

141. Engler, A.J., et al., *Extracellular matrix elasticity directs stem cell differentiation.* Journal of Musculoskeletal & Neuronal Interactions, 2007. **7**(4): p. 335-335.

142. Gilbert, P.M., et al., *Substrate Elasticity Regulates Skeletal Muscle Stem Cell Self-Renewal in Culture.* Science, 2010. **329**(5995): p. 1078-1081.

143. Pek, Y.S., A.C.A. Wan, and J.Y. Ying, *The effect of matrix stiffness on mesenchymal stem cell differentiation in a 3D thixotropic gel.* Biomaterials, 2010. **31**(3): p. 385-391.

144. Williams, S.K., S.S. Berman, and L.B. Kleinert, *Differential healing and neovascularization of ePTFE implants in subcutaneous versus adipose tissue.* Journal of Biomedical Materials Research, 1997. **35**(4): p. 473-481.
145. Petersen, T.H., et al., *Tissue-Engineered Lungs for in Vivo Implantation.* Science, 2010. **329**(5991): p. 538-541.
146. Ott, H.C., et al., *Regeneration and orthotopic transplantation of a bioartificial lung.* Nature Medicine, 2010. **16**(8): p. 927-U131.
147. Sun, Y., et al., *Rescuing replication and osteogenesis of aged mesenchymal stem cells by exposure to a young extracellular matrix.* Faseb Journal, 2011. **25**(5): p. 1474-1485.
148. Conboy, I.M., et al., *Rejuvenation of aged progenitor cells by exposure to a young systemic environment.* Nature, 2005. **433**(7027): p. 760-764.

Vita

Ryan Nagao was born to Daniel and Virginia Nagao in 1986. He graduated from the University of California, Davis with Honors in Biomedical Engineering in 2008. His undergraduate studies culminated with a University of California record of invention for a novel intubation assist device for veterinary use. Ryan then attended the University of Texas at Austin starting in the fall of 2008. While at UT, Ryan received the Engineering Doctoral Fellowship from the Cockrell School of Engineering, and a community service recognition from Dr. Christine Schmidt. Over a three year period he was the primary author for over $1MM in government and private funding, including a research proposal to the venture capital group, Remeditex. Ryan became active in entrepreneurship as an associate at Texas Venture Labs—a startup incubator, and Bluecap Partners—a venture capital LLC. He also acted as vice president for two years for the University Boxing club, treasurer of the Standup Comedy club. He was a two-time flag football intramural champion, and the 2013 basketball intramural champion while attending UT.

Permanent address: 1900 W42nd St., Austin, TX 78731
This dissertation was typed by Ryan Nagao.